Master's Degree in Energy and Nuclear Engineering

Politecnico di Torino

Master's Degree Thesis

Computational Thermal-Fluid Dynamics Analyses of Borated Water Distribution in the Vacuum Vessel of the Divertor Tokamak Test Facility

Supervisors

Prof. Roberto BONIFETTO

Dr. Antonio FROIO

Dr. Andrea ZAPPATORE

Candidate

Federico VAIR

AA 2022/23

Abstract

The Divertor Tokamak Test (DTT) facility is a superconducting tokamak being built at the ENEA Frascati Research Centre to foster the development of advanced divertor solutions for the EU DEMO.
The DTT Vacuum Vessel (VV) will be procured in three multi-sectors, in turn divided into one or more sectors; due to manufacturing and integration constraints, the different sectors cannot share the same design: some of them will be identically repeated ("*Regular*" sectors), whereas the remaining will all be one of a kind ("*Special*").
In DTT the VV plays also the role of neutron shield for the superconducting magnets, and therefore it will be actively maintained at the operating temperature of 60°C by borated water in forced flow to counteract the thermal loads (pulsed heating from the plasma and static radiative cooling from the thermal shield).
The water will flow in the free space between the two shells composing the VV; given the complexity of the geometry, a careful hydraulic design is mandatory, to avoid local stagnation points which may cause either overheating or freezing.
An additional requirement is the possibility to fully drain the entire VV from the bottom to perform baking with nitrogen at ≈ 200°C.
The water will enter the sectors in parallel by 9 inlets at the bottom and leave them by 9 outlets (staggered by 20°) at the top. This identifies 18 separate hydraulic paths, covering 20° toroidal portions and therefore reflecting the differences between the "*Regular*" and "*Special*" sectors; this asks for a proper balance of the mass flow repartition among them.
This work presents the full set of Computational Thermal-Fluid Dynamics (CtFD) analyses of the DTT VV to address the issues above. All the different hydraulic paths are separately analysed with the *Star-CCM+* software, with a $SST\ k-\omega$ turbulence closure, proving the effectiveness of their design. In addition, the coolant mass flow rate distribution among the different paths is assessed.
To conclude, results from CtFD analyses are exploited to approximate the hydraulic characteristic of each sector and to develop a system-level model of the full VV in Modelica language.
The overall VV pressure drop of $\Delta p = 2810$ [Pa], the outlet mixing temperature of $T_{out,mix} = 333.06$ [K] and a mass flow rate distribution close to the homogeneous condition (≈ 2.22 [$\mathrm{kg\,s^{-1}}$] in each sector) confirms that no relevant issues are found in the current VV design from the thermal-hydraulic point of view.

Acknowledgements

Eccoci finalmente alla parte più attesa di ogni tesi.
La parte che si scrive rigorosamente alla fine, ma che viene posta tendenzialmente all'inizio per creare quell'antitesi tra l'autore ancora pieno di speranze ed energie che spulcia con foga e fibrillazione tutta la letteratura scientifica perché *"Hey, questa è la mia tesi e l'introduzione voglio farla come Dio comanda"*, e l'autore che, alla fine di un lunghissimo (credetemi, ***lunghissimo***) calvario di sei mesi si ritrova in un essere strisciante notturno, che odia i rumori (e cancella 75% dell'intro).
A parte gli scherzi, questa parte serve soprattutto a dare un giusto peso alle cose.
Per primissima cosa, vorrei ringraziare i *Boss*, ossia i professori Roberto Bonifetto, Antonio Froio e Andrea Zappatore, supervisori attivi di questo lavoro.
Dall'inizio di questa tesi mi hanno costantemente fornito supporto e letteralmente una *valanga* di consigli, con appuntamenti fissi ogni settimana e un efficientissimo *customer service* online, della quale spero di non aver mai usufruito in modo inopportuno. Chissà se anche voi siete PIENI del DTT e del suo Vacuum Vessel.
Sempre loro mi hanno garantito l'accesso a risorse di calcolo che rappresentano il top italiano dell'high performance computing (risorse di calcolo fornite da hpc@polito[1], e da HPC Cineca[2]) permettendomi di concludere questa tesi entro i 150 anni.
Ringrazio poi i miei genitori e la mia famiglia, per i multipli e costanti sacrifici fatti per permettermi di essere qui a scrivere queste righe oggi.
Ringrazio *cù*, augurando a tutti di avere il privilegio di potersi totalmente abbandonare a qualcuno con leggerezza e serenità.
Ringrazio Diego, fedelissimo compagno di battaglie e di progetti, sempre falliti.
Concludo ringraziando i *Four sveiggj men*: Luca, *testardo* che cerca di trascinarci nei Balcani; Barbieri, inesauribile *jukebox di cazzate* e Zic, uomo davvero *strano*.
Un ringraziamento collettivo poi a quelli del *Big let's twist again*: meritereste anche voi una dedica, ma se non finisco in questa pagina mi si sminchia tutta la tesi e potrei letteralmente ESPLODERE.

[1] http://www.hpc.polito.it

[2] https://www.hpc.cineca.it

Table of Contents

List of Tables

List of Figures

Acronyms

CtFD
: Computational Thermal-Fluid Dynamics

CV
: Control Volume

DTT
: Divertor Tokamak Test

IB
: Inboard

OB
: Outboard

RANS
: Reynolds Averaged Navier-Stokes

SST
: Shear Stress Transport

TH
: Thermal-Hydraulic

TS
: Thermal Shield

VV
: Vacuum Vessel

Chapter 1

Introduction

"Ma è triste, è forse inutile l'amore della Sapienza se è saggio, se non è autentica pazzia amorosa, se non serve a rompere l'illusione della vita per mezzo dei poteri nascosti della vita, se non ricrea il miracolo, se non fa salire i gradini del tempio, se non si penetra nella luce".

Cantico dei Cantici

1.1 Thesis Structure and Objectives

The present Master Thesis is organized in five chapters and two appendices.
The main objective is to investigate the compliance of the latest design of the vacuum vessel (VV) of the Divertor Tokamak Test facility with all the project requirements, by means of computational thermal-fluid dynamic analyses. In particular, the distribution of the borated water in the VV is analyzed from the thermal-hydraulic point of view to identify possible unbalance in its repartition among the different flow paths. Special attention is devoted to the temperature variation due to the thermal loads, and to the presence of stagnation regions.
The main topics that will be discussed in each chapter, together with all the ancillary and integrating ones, are organized as follows:

- Chapter 1: the first chapter has a specific introductory nature.
  It's goal is to present in sections 1.2.1 and 1.2.2 a crash introduction to nuclear fusion energy physics and engineering principles, aiming at providing the reader with the instruments to better understand the contents presented in the following chapters. Of course, it's almost useless to specify that the presentation of these topics will be rather superficial and incomplete, for obvious reason of space and specific knowledge of each single topic.
  This chapter is then concluded by presenting the *"coherent, ambitious and pragmatic"* plan foreseen by the EUROfusion roadmap to provide nuclear

fusion electricity by 2050 in section 1.2.3, and by introducing in section 1.3 the Divertor Tokamak Test (DTT) facility, main character of the present work, which is currently under construction in ENEA Frascati Research Centre, Italy.

- Chapter 2: the second chapter focuses on a specific component of the DTT facility, namely the Vacuum Vessel (VV), which is the real subject of the present Thesis.
  In section 2.1 the geometry of the vacuum vessel is presented together with the previous thermal-hydraulic (TH) analysis of one regular sector done in 2021 by the NEMO group of Politecnico di Torino Energy Department.
  Lastly, in section 2.2 all the relevant design updates experienced from 2021 to the end of 2022 are discussed and visualized to justify the need for new TH analyses of regular and special sectors.

- Chapter 3: the third chapter represents the core of the Master Thesis and it is by far the most technical one.
  It focuses on the setup of the thermal-fluid dynamics model based on the pieces of physics involved in the flow of borated water inside VV channels.
  Topics such as turbulence modelling (section 3.3), $SST\ k-\omega$ turbulence closure (section 3.4), buoyancy forces modelling (section 3.5) and wall treatment (section 3.9) are discussed and presented by looking directly at the equations implemented in the commercial software *Star-CCM+*, used to develop all the computational thermal-fluid dynamics (CtFD) analyses.
  Chapter 3 is then concluded with the assessment, starting from the available literature, of the thermo-physical properties of borated water for the material characterization.

- Chapter 4: the last but one chapter is dedicated to the presentation and discussion of the numerical results.
  Much attention is devoted to the assessment of results' sensitivity with respect to specific simulation choices such as mesh parameters, adopted wall treatment, prescribed inlet turbulence specification (section 4.1.2), followed by a mesh independence study for the model *verification* in section 4.1.4.
  The chapter continues with the presentation of TH results for all the regular and special control volumes (CVs) and it is concluded with a pure-hydraulic system-level model developed on the open-source *OpenModelica* software for the complete vacuum vessel characterization.

- Chapter 5: the last chapter gives space for further discussion of the obtained results, opening to the possibility (or necessity) for upgrades of the existing model or for new and more powerful models. It's silly to think that, even after

such efforts, the present work can be considered concluded and this chapter tries to categorize future works based on the their priority.

- Appendix A: the first appendix deals with the inclusion of temperature effects in the turbulent boundary layer.
  It starts from the derivation of the turbulent Prandtl number for a simpler 2D case known as *Coutte Flow*, to then analyze how CFD codes deal with temperature wall functions. These topics are useful, but not mandatory, for the comprehension of the computational model presented in chapter 3.

- Appendix B: the second and last appendix is used to show support material, useful but not strictly necessary, for the integration of the TH results.
  Here, temperature scalar scenes, velocity scenes for backflow visualization and detailed mass flow repartition tables are presented for all the CVs but CV1, whose scenes and tables are integrated in the main matter of the Master Thesis.

1.2 Nuclear Fusion: the path towards the European DEMO Reactor

1.2.1 Introduction to Energy by Fusion

In this section, a brief introduction on nuclear fusion is presented.
Nuclear fusion is the process in which two or more atomic nuclei are combined to form heavier atoms and subatomic particles as neutrons or protons.
If the process results in nuclei lighter than iron ^{56}Fe or nickel ^{62}Ni then the fusion product will be characterized by a mass defect (increasing binding energy according to the Einstein relationship $E = mc^2$) which is translated into an energy release (exothermic reaction), typically in the form of kinetic energy of the products.
Among all the existing and documented fusion reactions, the D-T (deuterium-tritium) fusion reaction is by far the easiest one to be initiated (even if the adjective "easy" make sense only in relative terms) but several drawbacks are present.
As can be seen in the reaction written below, the fusion process that exploits the two hydrogen isotopes produces large number of highly energetic neutrons (≈ 14 MeV against the ≈ 2 MeV of fission) and relies on tritium which is extremely rare in one hand, but also radioactive (half-life of 12.26 years) and volatile on the other hand:

$$\mathrm{D} + \mathrm{T} \longrightarrow \alpha + \mathrm{n} + 17.6\ [\mathrm{MeV}]$$

The specific energy of 50-50 D-T mixture is 338000 $[\mathrm{GJ\,kg^{-1}}]$.
One possible explanation of why energy from fusion is always "*thirty-years away*" is that, in order to overcome electrostatic repulsion between reactants, large kinetic

energy of the latter should be reached (i.e temperatures). This could be achieved by creating, sustaining and confining a burning $10 \div 20$ keV D-T plasma, which is actually the key challenge of researchers and scientists involved in nuclear fusion development for energy purposes, since no materials are able to withstand directly such temperatures without melting or even vaporizing immediately, introducing then impurities into the plasma with an immediate interruption of the reaction because of massive loss of energy by radiation.
The energy released by nuclear fusion however, already demonstrated to be feasible under a theoretical point of view, will guarantee in the future an energy supply which is:

- **Clean**: no GHGs are produced in the process. No radioactive fission products nor trans-uranium elements are foreseen. Despite that, the structural materials' activation remains an issue, even if it is estimated that after one century natural radioactivity levels are restored.

- **Safe**: fusion reaction is in principle an *energy self-sustained* reaction and not a *particles self-sustained chain* reaction. It means that no criticality accidents are possible a priori, with possible power divergences.

- **Predictable**: unlikely stochastic direct or undirect solar energy resources, the nuclear fusion reactors will be able to operate with high capacity factors, ensuring in a reliable way the right amount of energy when needed.

- **Inexhaustible**: hydrogen in the most abundant element in the universe and deuterium is its second more abundant isotope. As far as tritium is concerned instead, the question is trickier being the latter, radioactive with a very short half-life. The possibility of running out of tritium without having the possibility to start the first reactor by 2050 is not a remote ones.

1.2.2 Nuclear Fusion Reactor Engineering

A detailed review or treaty on nuclear fusion reactor's engineering is far beyond the scope of the present work.
However, having in mind the most relevant engineering challenges involved in the design and realization of a nuclear fusion reactor, together with a brief history of fusion coupled with near and long-term future perspective, will simplify the process of finding an answer for the question: "why?" of this Master Thesis.
Nowadays, two main plasma confinement strategies are investigated: magnetic confinement and inertial confinement.
Focusing the attention on the first one solely, it exploits the definition of plasma, where nuclei and electrons are no longer tied together: therefore they exist as separate charged entities whose trajectories can be influenced by a magnetic field due to the Lorentz force.
Nuclear fusion reactors based on magnetic confinement are identified as Tokamak ("toroidal chamber with magnetic coils"). In a modern Tokamak, the plasma is confined by three magnetic components:

1. Toroidal Field B_φ: it replicates the field of an ideal toroidal solenoid exploiting a discrete number of DC superconducting toroidal field coils (TF).

2. Poloidal Field B_θ: it acts along the small circumference of the torus and it is generated by the plasma current itself, which is induced in turn by the AC operation of a superconducting central solenoid module (CSM).

3. Vertical Field B_v: generated by superconducting poloidal field coils (PF) positioned parallel to the equatorial plane of the reactor at different heights.

The desired magnetic field to succeed in confining the plasma can reach > 10 [T], and by applying the Ampere's law it becomes immediately clear that superconductors (temperature below 4.5 [K]) are mandatory to technically sustain currents of the order of [MA]. However, even if the 10 [keV] plasma is properly confined, the efficient and effective management of power and particle exhaust, while keeping under control the level of impurities is the second of the three main challenges in a fusion reactor.
In the 0-D, steady-state power balance the power in the alpha-channel is dissipated by radiation, advection and conduction respectively.
The power in the radiation channel is isotropic, resulting therefore in an heat flux for plasma facing components ≤ 10 [$\mathrm{MW\,m^{-2}}$]).
On the other hand, the power in the advection and conduction channels are intrinsically anisotropic, and are thus distributed on a much more limited wetted area. In the so-called Scrape-Off Layer (SOL), magnetic surfaces are no longer closed and particles are directed towards the divertor (reactor's component in charge

of dealing with the power exhaust issue); here they imping divertor plates with very high energy. In the European demonstrative nuclear fusion reactor DEMO, which will be characterized by a plasma power of 3000 [MWth], the resulting heat fluxes on divertor's targets are estimated to be of the order of 40 [$\mathrm{MW\,m^{-2}}$]. Revolutions in the power exhaust handling strategies are therefore mandatory for the realization of the first kWh of electricity from fusion, since no materials are able to withstand such thermal loads.
The last main challenge in a fusion reactor concerns the faiths of high energetic neutrons.
This is taken over by the breeding blanket which has three main objectives:

1. to extract the kinetic energy of neutrons and exploit it to heat up an energy vector (like water) which in turns it's expanded in a turbine to produce electricity.

2. to shield all the components outside it, as the vacuum vessel, the TF coils and the cryostat from excessive neutral load (which causes degradation/activation and dangerous volumetric heat deposition)

3. to breed (self-produce) an amount of tritium larger than the one consumed for the reactions, ensuring a tritium breeding ratio TBR>1.

1.2.3 The EUROfusion Roadmap by 2050

The current European efforts involved in the development of nuclear fusion are administrated and managed by EURATOM, the international organization established in 1957 to coordinate nuclear research and development of the European member states.
Within EURATOM, Fusion For Energy is the organization that has the responsibility to properly manage European contributions (almost half of the construction cost) to the International Thermonuclear Experimental Reactor ITER, while cooperating with six global partners in fusion R&D.
In parallel, EUROfusion is the European Consortium for the development of fusion energy. EURATOM gives the responsibility to EUROfusion to implement the development of fusion as stated in the roadmap, a document summarizing most relevant milestones and deadlines for the realization of the first kWh of electricity by fusion.
The latest EUROfusion roadmap [1] available is based on three main pillars:

1. To demonstrate the scientific and technology feasibility of fusion on a large scale (ITER).

2. To create a fusion neutron source facility for materials' test and qualification (IFMIF-DONES).

3. To demonstrate electricity production and closed fuel cycle (tritium self-sufficiency) operation in a competitive way, proving also the economic feasibility (DEMO).

All of them have to be pursued together with an eye on alternative designs (Wendelstein 7-X stellarator for instance), not to miss possible plant's architecture opportunities that may help in the search for a global optimum, also in terms of safety and waste minimization.
The roadmap also faces the heat exhaust and helium removal issue introduced in the previous section, highlighting the necessity of an "*aggressive programme on alternative solutions*" to overcome the impossibility to extrapolate ITER divertor solution for DEMO.
In 2015, Italy presented the project proposal "*Blue Book*"[2] of a dedicated Tokamak exhaust facility, the Divertor Tokamak Test DTT, real subject of the present work, to solve for that specific issue which received a positive evaluation from the EUROfusion Consortium. Next section will be therefore exploited to provide a brief introduction on the DTT facility.

1.3 The Italian Divertor Tokamak Test DTT Facility

As already introduced in the previous chapter, the idea of a dedicated divertor test facility was born as a consequence of the increasing difficulties found by researchers and scientists when dealing with the power exhaust problem in magnetic plasma confinement.
The joint effort of about one hundreds of experts coming from the ENEA Italian Institution[1] and third parties, with the support of European (KIT and IPPLM[2]) and international labs[3], was presented with the draft of a dedicated small Tokamak reactor for the characterization and test of several divertor strategies.
In April 2018, the Frascati Reasearch Centre in Rome was selected as DTT site, among the 9 location proposed for the public call.
The latest comprehensive revision of the original project dates back to April 2019;

[1]The "Agenzia nazionale per le nuove tecnologie, l'energia e lo sviluppo economico sostenibile" it's the EUROfusion program manager that coordinates the 21 partners carrying on research activities on fusion in Italy

[2]Karlsruhe Institute of Technology, Germany and Institute of Plasma Physics and Laser Microfusion, Poland

[3]More info about all the DTT contributors are available at [3]

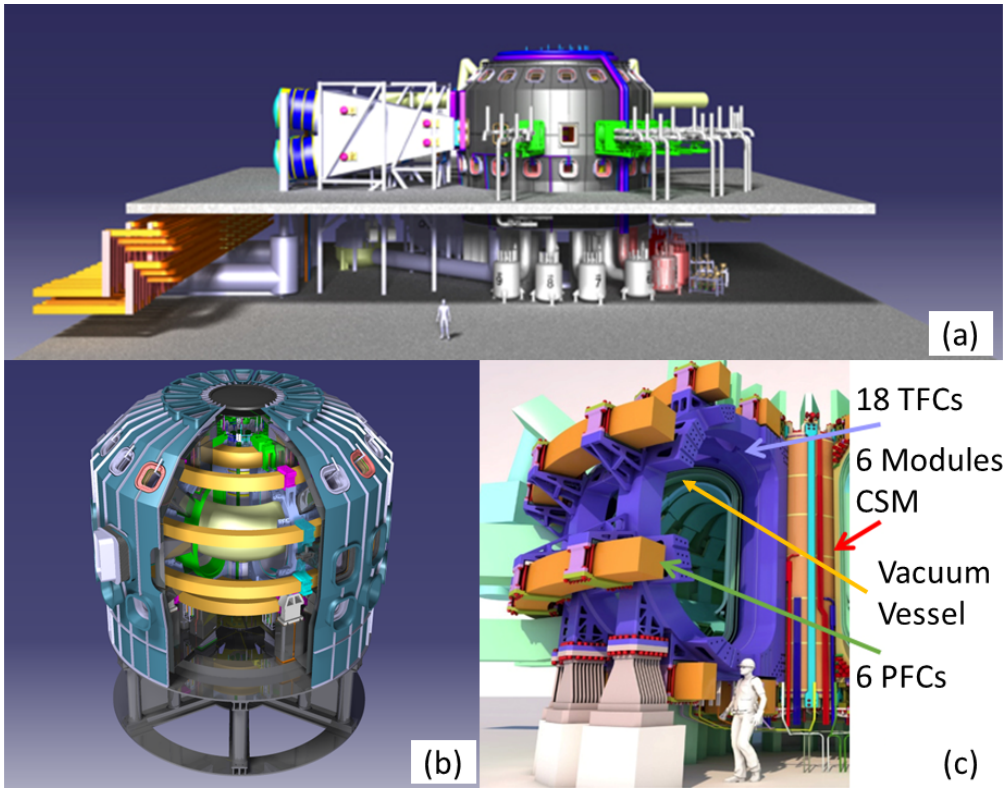

Figure 1.1: (a) The DTT main building with all the auxiliaries. (b) Close-up on the DTT cryostat. (c) Close-up on DTT reactor core, with the identification of the Vacuum Vessel and of the different components making up the magnets' system. Courtesy of DTT (2023).

in the same year the DTT Consortium was founded aiming at implementing the DTT realization.
At this point, it is mandatory to stress again that the current Thesis falls exactly in a period of strong transition and renovation; despite a little insight on more recent design choices for a specific component of the DTT, namely the vacuum vessel which will be presented and discussed in the next dedicated chapter, all the reported information and pictures presented here are therefore only indicative, since an updated DTT interim design report is expected in the near future, together with the updated EUROfusion roadmap.

The DTT facility, appearing in figure 1.1, has to integrate different aspects in order to recreate, at least in terms of dimensionless quantities because of cost constraints, the operating conditions planned for DEMO, while ensuring the complete realization of the project and to bring at least one divertor strategy to sufficient level

of maturity by 2030, a time window coherent with the scheduled fusion roadmap discussed in the previous section.
The DTT facility, as already introduced, will guarantee wide flexibility to test different magnetic divertor topologies (like liquid metal divertors) and plasma facing materials together with alternative plasma shape configurations in order to asses an integrated solution for the power exhaust issue in DEMO.
According to the DTT "*Blue Book*", the first tender was scheduled in 2016, estimating the first DTT experimental operation by 2022, with an overall expected cost for the realization of €500 million, half of them covered by a loan from the European Investment Bank and €60 million already allocated by EUROfusion from the European Horizon 2020.
In the latest official design interim report published in 2019, the DTT "*Green Book*", the first operation was expected to start by the end of 2025, but little they know about the rock 'n roll that was going to happen the next year in 2020.
According to the DTT website, today the first experimental plasma of 3 [T] and 2 [MA] is set for 2026; currently the DTT is in its contruction phase.
The most relevant parameters of the DTT machine are reported in table 1.1, and briefly compared with the one characterizing ITER and DEMO Tokamaks.

Parameter	**DTT**	**ITER**	**DEMO**
Major Radius [m]	2.19	6.2	9.1
Minor Radius [m]	0.7	2	2.93
Aspect Ratio [-]	3.1	3.1	3.1
Plasma Current [MA]	5.5	15	19.6
Toroidal Field [T]	6	5.3	5.7
Pulse Length [s]	95	400	7600

Table 1.1: Comparison among DTT, ITER and DEMO most relevant parameters.

In 2021, Politecnico di Torino became a partner of the DTT Consortium, and the present work has been carried out in view of this important cooperation.
The DTT operation is expected to last for $25 \div 28$ years, laying the scientific foundations for the European DEMO while ensuring an occupational impact of at least 250 people. The economic impact for the hosting territory is estimated to be of the order of 2 billion Euro.

Chapter 2

The Divertor Tokamak Test Vacuum Vessel

"Incapace di capirlo, maestro nello scriverlo"
Proverbio arabo

In this chapter, a brief description of the Vacuum Vessel (VV from now on) of the just introduced Divertor Tokamak Test (DTT) facility is presented, together with a view on previous results found with Thermal-Hydraulic (TH from now on) analysis of a regular sector and with the latest design updates which justify indeed the need for new TH analyses.

2.1 The DTT Vacuum Vessel Geometry and Previous Works

The VV in a Tokamak system is designed to provide an enclosed environment where favorable conditions for a burning plasma can be reached (i.e high quality vacuum).
The VV design however has to take into account several other requirements besides the high quality vacuum: it also provides support for in-vessel components (e.g first wall, breeding blanket) while withstanding nuclear and radiative loads.
In addition to that, the VV has a shielding function towards TF coils and it represents a first confinement barrier, in case of accidents, between plasma and external environment.
On the other hand, the VV should provide several access ports which allow the diagnostic, the control/regulation and the maintenance of in-vessel components.

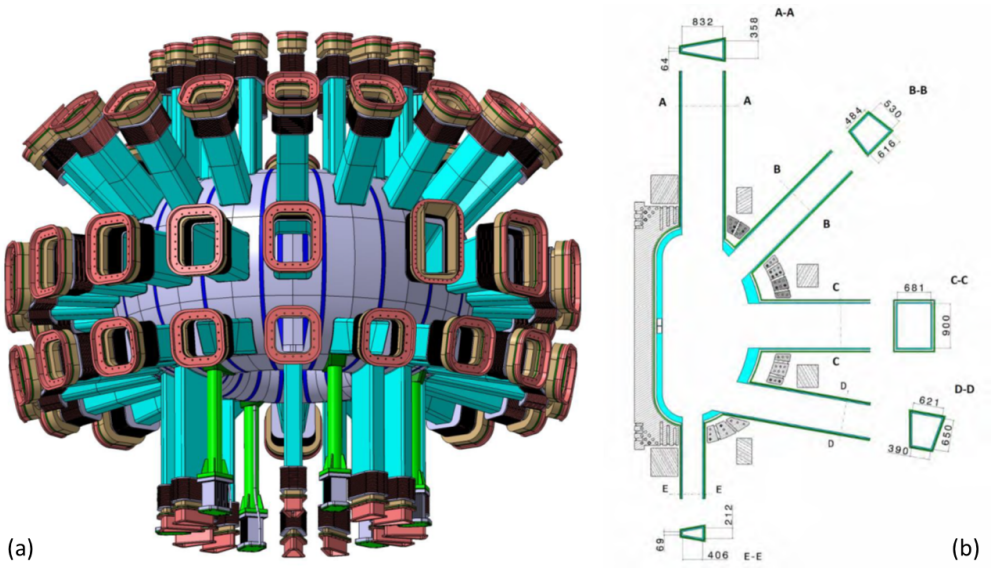

Figure 2.1: (a) The DTT Vacuum Vessel, full view. (b) Poloidal cross-section of the VV with a focus on different poloidal ports. Courtesy of ENEA.

According to the Interim Design Report "*Green Book*" [4], the main vessel is made of 14 standard modules (20° toroidal development) and one 80° NNBI module, where the negative-neutral beam injector is accomodated.
In the conceptual design, the VV toroidal structure is characterized by an outboard diameter of 6800 [mm], an inboard diameter of 2530 [mm] and a total height of 3940 [mm]). Such structure weights around 36 tons and accomodates a plasma side volume of 75 [m^3].
Each sector contains from four to five poloidal ports, numbered clockwise from top to bottom as shown in figure 2.1(b), which provide several openings with multiple functions:

- Port #1: it is provisionally devoted to the remote handling of the inboard first wall (FW).
- Port #2: it points directly to the plasma center in order to correctly direct Electorn Cyclotron Resonance Heating (ECRH) antennas and diagnostics.
- Port #3: the equatorial port is mainly devoted to diagnostic system and ECRH/ICRH antennas, but it is also exploited for the remote handling of outboard FW. Two of them have to accommodate the NBI modules, which are 30°-oriented with respect to the poloidal plane.
- Port #4: it is aligned with the divertor in order to guarantee its remote maintenance as well as (de)commissioning.

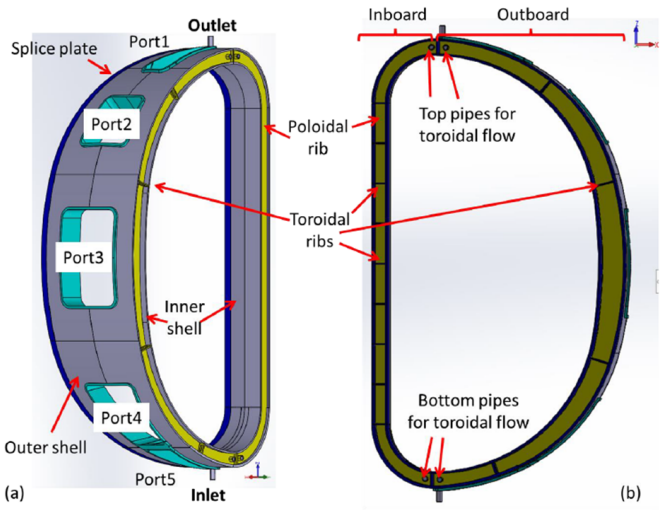

Figure 2.2: View and nomenclature of a 20° regular VV sector in 2021. (a) Isometric view. (b) Poloidal cross-section view. Pictures are taken from [5].

- Port #5: when present, it is mainly devoted to diagnostics, pumping and fuelling.

The volume between inner and outer shells is travelled by borated water, which acts simultaneously as coolant and neutron shield. A set of poloidal and toroidal ribs, exploited to sustain and to give stiffness to the overall structure, creates internal flow paths for the coolant.
Splice plates (represented in blue in 2.1(a)) are employed to connect adjacent sectors between each others, and they are directly welded on site.
The ≈ 13.5 [m^3] of coolant, constrained between inner and outer shells, flow mainly from the bottom to top in view of the limited connections in the toroidal directions. Inboard (IB) and outboard (OB) paths are kept separated and are only connected hydraulically at inlet and outlet regions.
The reference geometry of a regular sector simulated by the NEMO group in 2021 is characterized by 20° toroidal width with five ports and one splice plate, as reported in figure 2.2.
Bottom and upper pipes for toroidal flow will be open during the normal operation of the VV, while all of them are kept closed during the pressurization test of each sector to detect possible leakages.
Being the regular sectors replicated identically in the toroidal direction, the minimum control volume to perform TH analysis consists of two half regular sectors connected with the splice plate in between. The TH solution could then be mirrored with respect to a plane identifying radial and vertical directions.

In the work done by the NEMO group, two cooling strategies namely **PAR** and **SER** have been analysed and studied in deep in a steady-state condition.
Both options allowed to minimize the overall number of inlets and outlets from 18 to 9, drastically reducing the ex-vessel piping complexity.
In option PAR, the flow was expected to move in parallel in the three regions individuated by the poloidal ribs, while in the SER case the three poloidal channels were crossed by the same amount of borated water in series, moving therefore both from bottom to top (two lateral channels) and from top to bottom (central channel).
The main flow distribution is reported below in figure 2.3 (with a focus on the outboard leg only for sake of brevity).

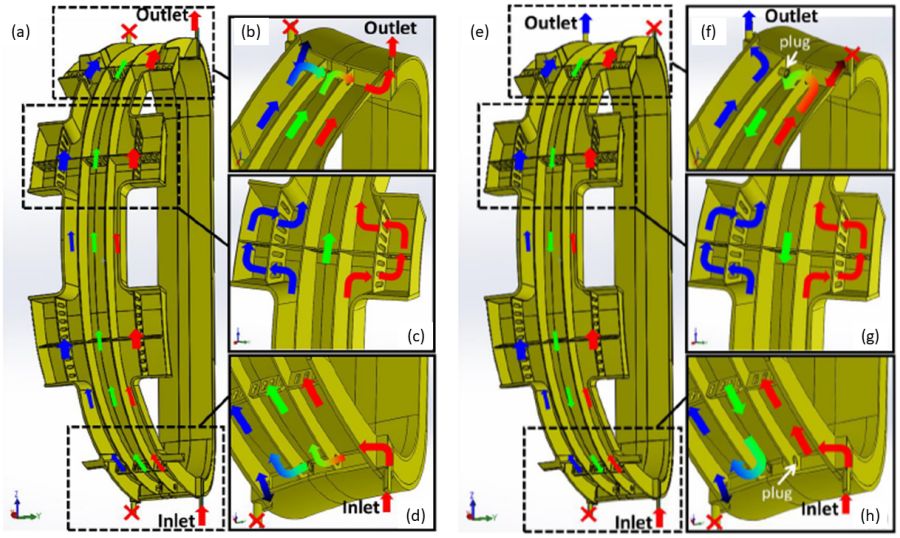

Figure 2.3: On the left, option PAR with three OB parallel flow paths (a). Close-up on the outlet (b), equatorial (c) and inlet (d) regions. On the right, OB flow paths in option SER (e) with details of the outlet (f), equatorial (g) and inlet (h) sections.

The total mass flow rate of borated water considered was 20 [kg s^{-1}], assumed to be equally distributed in all the 18 sectors, prescribing thus 1.11 [kg s^{-1}] of coolant at half of the inlet section for each single control volume, with an inlet temperature and pressure of 60°C and 4 [bar] respectively (remember that two adjacent control volumes share the same inlet and therefore the resulting $20/18 = 2.22$ [kg s^{-1}] are equally split in the two domains). However, as a first approximation, default thermo-physical properties of pure water have been considered for the simulation, as summarized in table 2.1:
Due to the very limited fluid's velocity, the flow was expected to be fully laminar but in inlet and outlet sections, characterized with narrower diameters, where a

Property	Value
Density [$\mathrm{kg\,m^{-3}}$]	997.6
Dynamic viscosity [$\mathrm{Pa\,s}$]	$8.871 \cdot 10^{-4}$
Specific heat [$\mathrm{J\,kg^{-1}\,K^{-1}}$]	4182
Thermal conductivity [$\mathrm{W\,m^{-1}\,K^{-1}}$]	0.62
Thermal expansion coefficient [$\mathrm{K^{-1}}$]	$3.9 \cdot 10^{-4}$
Turbulent Prandtl number	0.9

Table 2.1: Thermo-physical properties of pure water exploited for the material characterization in 2021 TH simulations.

turbulent state of motion was reached. For that reason, RANS turbulent model has been adopted with a $SST\ k-\omega$ turbulence closure, coupled with a Boussinesq approximation to take into account the effect of buoyancy due to gravity acting along the z-direction (-9.81 [$\mathrm{m\,s^{-2}}$]) while considering the flow incompressible.
The thermal driver considered for the simulation was the radiative cooling provided by the VV thermal shield (TS), namely -70 [$\mathrm{W\,m^{-2}}$] (evaluated on a 20° toroidal extension) applied uniformly on the outer surface of the fluid directly, neglecting therefore the conjugate heat transfer intrinsic nature of the problem in one hand, but being conservative in the final solution on the other hand (neglected thermal resistance of the outer shell).
No contribution for the nuclear load has been taken into account, being the latter pulsed and not steady, with a peak of 490 [W] on a 20° sector only during the plasma flat top (maximum of 85 seconds if considering the longest plasma scenario Double Null). The average power of ≈ 12 [W] can be considered therefore negligible.

The results showed that most of the pressure drops were concentrated in the inlet/outlet pipes, where fluid velocity reaches approximately 1 [$\mathrm{m\,s^{-1}}$], while in the overall sector the pressure can be considered almost uniform in view of the very limited fluid velocity (< 10 [$\mathrm{cm\,s^{-1}}$]).
The overall pressure drops due to friction of only $\approx 400 \div 500$ [Pa] (option PAR and SER respectively) were therefore non critical.
As far as the temperature distribution is concerned, in the option PAR the minimum temperature was reached in the central channel of the outboard leg, because the mass flow rate in the splice plate resulted to be smaller, while in the SER cooling configuration a toroidal temperature gradient has been detected in view of the serial connection of the three main poloidal channels.
The overall differences between maximum and minimum temperatures are summarized in table 2.2, while scalar scenes of pressure and temperature distribution in both configurations are presented in figure 2.4.

Option	ΔT_{max} [K]
PAR	4
SER	2

Table 2.2: Maximum temperature difference between PAR and SER cooling configurations.

As a conclusion of the TH analysis, no issues were found in terms of pressure and temperature distributions when reducing the number of inlets and outlets from 18 to 9, with no boron precipitation ($T < T_{min}$) nor accelerated steel corrosion ($T > 80$°C) in both cooling strategies.
The option SER resulted to be better from a pure thermal point of view because of reduced temperature decrease, since it ensures the mass same flow rate in each poloidal section. However it is worth noticing that the temperature difference is not that large with respect to the PAR configuration.
Nevertheless, the latter is the only one that allows the VV to be fully drained during the baking operation with hot nitrogen.
For that reason, the PAR cooling strategy has been therefore indicated as the favourable option, coupled with future optimization of the flow impedance towards the central poloidal channel (diameter of toroidal pipes), to guarantee a more equal flow distribution.

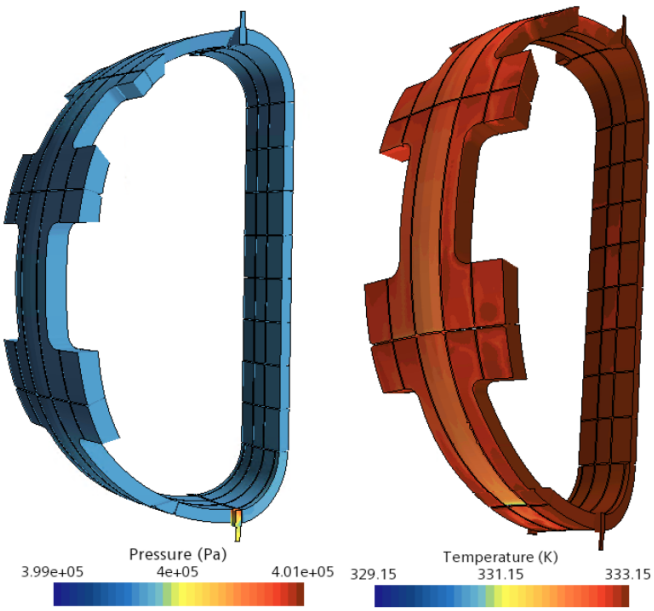

(a) *PAR*

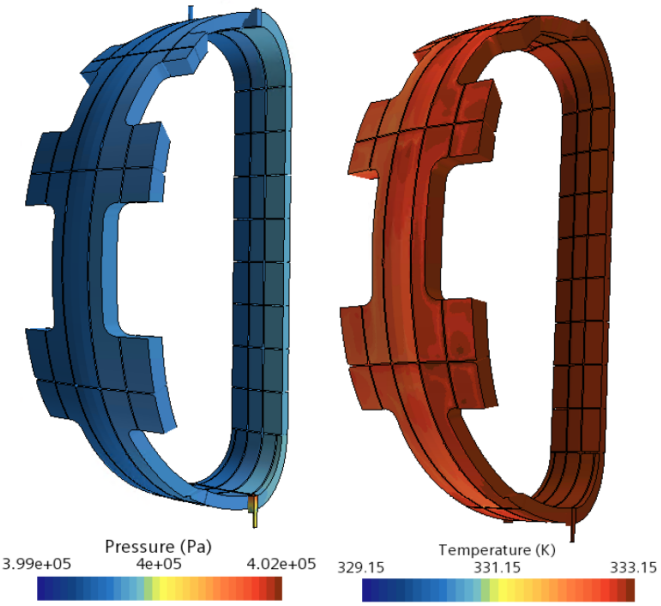

(b) *SER*

Figure 2.4: Pressure and Temperature scalar scenes for PAR and SER cooling configurations.

2.2 VV Design Updates and Justifications for New Thermal-Hydraulic Analyses

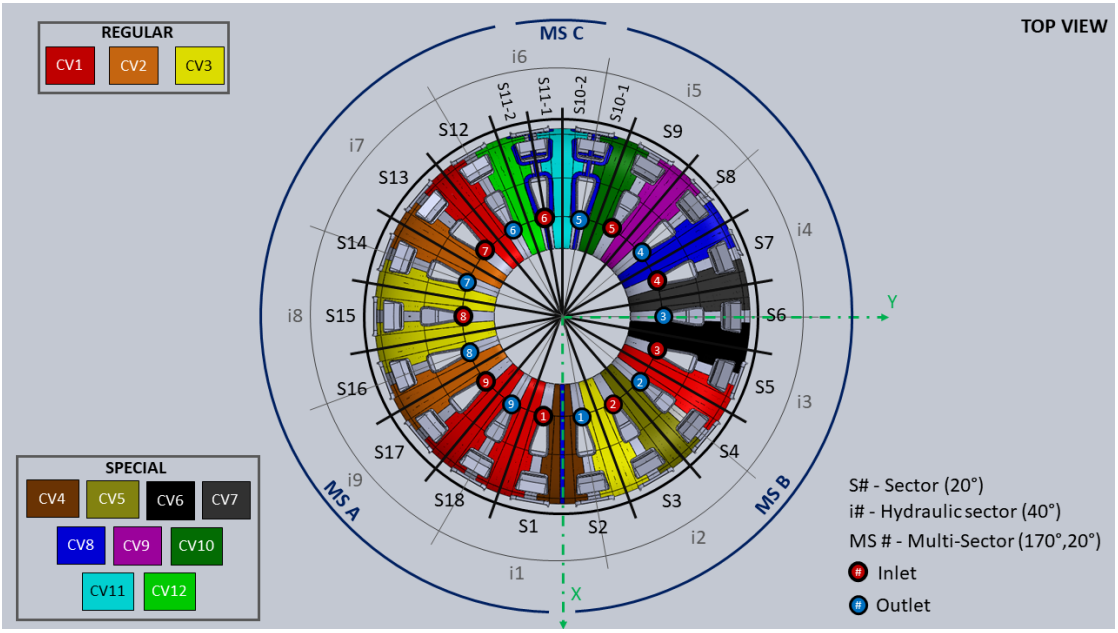

Figure 2.5: Top view of the updated VV geometry with complete nomenclature. Regular and Special CVs are highlighted with different colors.

After the conclusions found by the NEMO group in 2021, the overall vacuum vessel design has been updated extending the staggered arrangement of inlets and outlets and the PAR flow configuration to the whole torus, non regular sectors included.

In October 2022 the VV faced a complete revision with several improvements (version **REV03**), replacing **REV02** of June 2022.
Despite little changes in overall dimensions (outboard diameter of 6960 [mm], inboard diameter of 2530 [mm] and total height of 3910 [mm]) major differences can be found in what regards the manufacturing and assembling point of view.
In fact, it has been decided to manufacture the VV in three main sections only (called respectively multi-sector A,B and C), rather than with 18 separate sectors assembled via splice plates (see figure 2.6 for details).
The two 170° multi-sectors (A and B) will be built, assembled and tested (inter-shell pressurization test with water at $p_{test} = 7$ [bar]) separately and then connected, to fully complete the toroidal geometry, with the last 20° section C (including original sectors S10-2 and S11-1) with the TF coil already mounted.
The holes for the pressurization test have been moved respectively from their

original positions to the two limiting boundaries of each section only, introducing thus changes in the already simulated regular sectors.
A final pressure test will verify then the watertightness of welded sectors A+B+C.
Moreover, splice-frames has been introduced to improve and simplify the installation of the poloidal ports in section C with a consequent change in the orientation of the neighbouring poloidal ribs, to left space for the former (see figure 2.6).
That geometry updates will have an effect on the flow distribution because of the reduced cross section of the central poloidal path (the new toroidal ribs will have only two apertures rather than three) that has to be assessed. On the other hand, the two lateral paths will result to be wider.
In addition to the already discussed updates, the shape of the shorter poloidal ribs between two ports has been uniformed in the regions where the holes for the pressurization test are no longer needed (figure 2.6(c)), while the distribution channels present in some inlet and outlet sections have been substituted with simpler wall compartments (figure 2.6(b)), after having highlighted the welds' complexity in the REV02 design.

The reference geometry for the thermal-hydraulic simulations consists therefore in 18 sectors (regular and special) organized in two 170° multi-sectors and one 20° connecting sector.
A total number of 82 ports provides direct access to the inner plasma-side volume of 75 [m^3], while during operation borated water (20 [$kg\,s^{-1}$], inlet temperature and pressure of 333.15 [K] and 4 [bar] respectively) or nitrogen (inlet temperature of 200°C) will flow in the inter shell volume of 13.5 [m^3] for cooling and baking purposes respectively.
In figure 2.5, 12 control volumes (CVs from now on) for thermal-fluid dynamics simulations can be therefore distinguished: the tag "*Regular*" refers to CVs which are very similar, in terms of geometry, to the one simulated in 2021.
Moreover, CVs of type "*Regular*" are repeated multiple times in the VV geometry, typically with a mirrored symmetry. Therefore, if CV1-type R (inlet on the right-end side) is simulated, then the solution of CV1-type L is automatically defined by mirroring the solution.
On the other hand, "*Special*" sectors are **OOAK** (one of a kind), namely they appear in the VV geometry only once.
Special control volumes include splice plates (CV4), splice frames (CV10-11-12) and skewed (because of NNBI) or missing ports (CV8-9 and CV6-7 respectively).
To conclude, "*Regular*" and/or "*Special*" CVs sharing the same inlet pipe are grouped in the same hydraulic sector *i#*.

2.2.1 New Regular Control Volumes

Differently from the geometry analysed in 2021, in the updated design three distinct regular CVs (CV1-2-3) can be distinguished (they are highlighted in red, orange and yellow respectively in figure 2.5).
The origin of multiple different regular CVs derives from the fact the lowest port (port #5) is not always present in all sectors: this feature, combined to the staggered arrangement of inlet and outlet pipes, introduces asymmetries between adjacent sectors (always remember that the control volume for the thermal-hydraulic simulation is located between two adjacent half-sectors), as highlighted in figure 2.7 with a comparison to the previous geometry.
In the latest geometry in fact, the 9 sliding supports located at the base of port #5 originally designed to vertically sustain the 36 tons of VV structure has been replaced with more cumbersome triangular pedestals, originally located every two sectors. As a consequence, because of support's dimension, the port #5 in these sectors has been removed (2021).
In the latest update, the triangular supports have been placed every three sectors rather than two (indicative), in order to increase the number of available port #5 from 9 to 11, leading to the current control volumes' distinction.
Moreover, in figure 2.8 it can be seen that the number of toroidal ribs have significantly changed in the lower part of each sector (specials included) to provide additional structural support to the bottom region of the VV where the divertor rails will be installed.
Intuitively (and TH results in chapter 4 will corroborate that) such change will introduce significant qualitative modifications in the fluid flow, increasing the pressure drop because of more intricate paths.

2.2.2 New Special Control Volumes

Coherently to what stated for regular control volumes, also special control volumes have been affected by some design modifications.
Even if such modifications do not result in the necessity for new TH analyses (since no TH analyses have ever been done before for special CVs), it is worth reporting them for sake of completeness.
As already mentioned above, the structural reinforcement by means of additional toroidal ribs is extended all along the lower side of the torus, influencing therefore the coolant distribution in special CVs as well.
In addition to that, even if it isn't related to the thermal-hydraulic side, it is important to stress that the 80° NBI module experienced an important modification in terms of functionalities.
In a recent publication by Agostinetti et al. [6], the improved conceptual design of the beamline for the DTT NBI was presented.

Differently to what originally thought, in 2020 the team working on DTT plasma physics underlined the necessity to have a NBI beam usable also for diagnostic purposes: the original "double-source" solution threfore, not adequate for such additional requirement, was substituted by a "single-source" ones, with a beam providing deuterium neutrals for an overall injected power of 10 [MW], as presented in figure 2.9

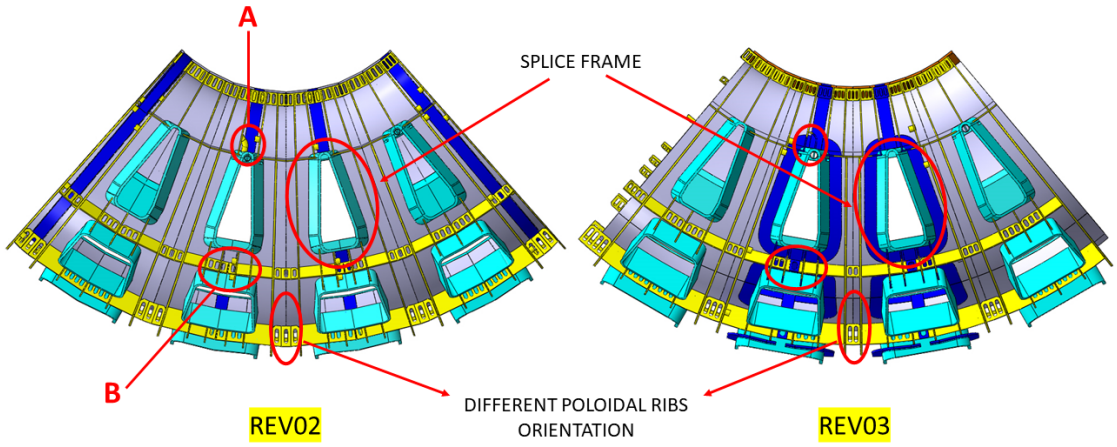

(a)

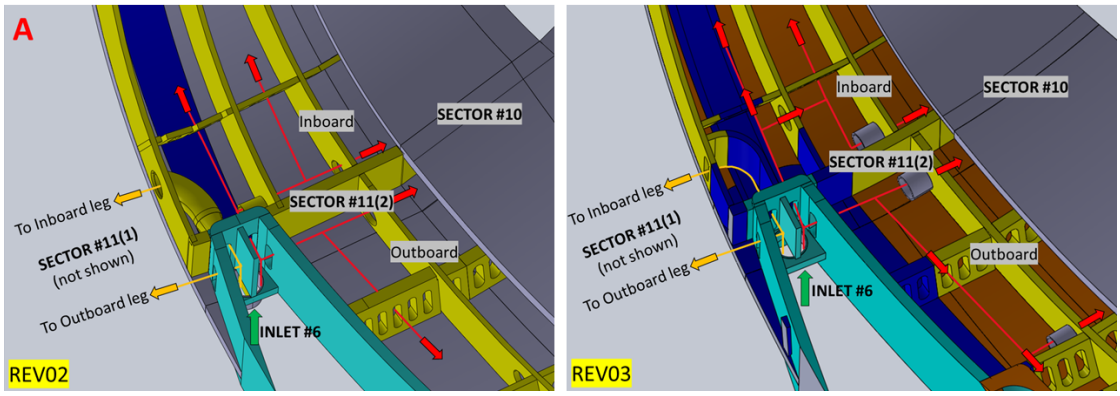

(b)

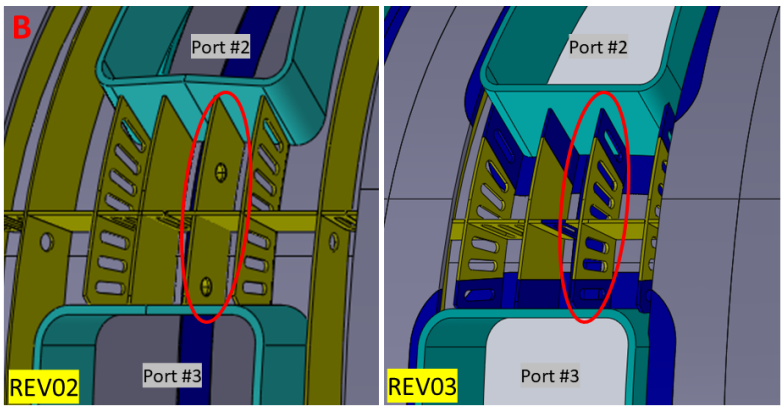

(c)

Figure 2.6: Major relevant differences between REV02 and REV03 designs (a). Both wall compartments (b) and uniformed toroidal ribs (c) are foreseen in sectors S10-11. See figure 2.5 for clarifications on complete vacuum vessel nomenclature.

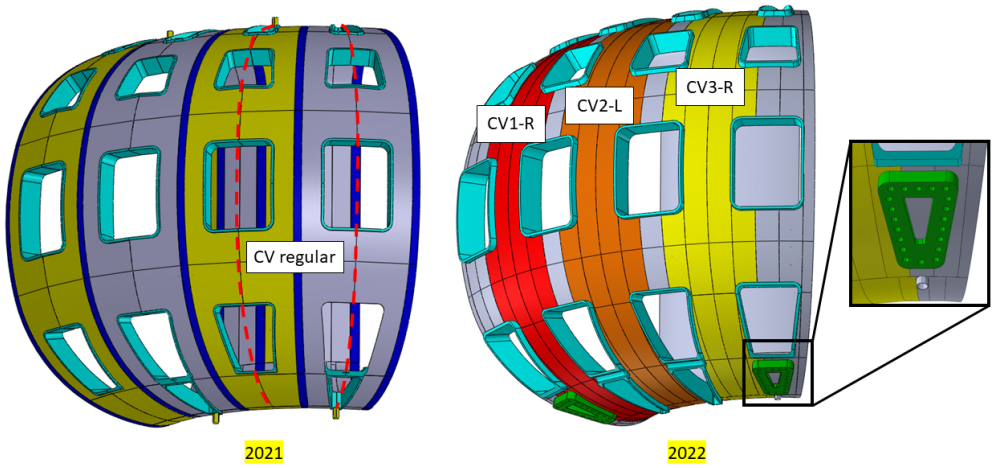

Figure 2.7: Comparison between 2021 regular sectors and 2022 updated designs. The ex-regular CV (highlighted with the red dashed line) differs from the three new regular ones of the updated design (shown in red, orange and yellow for an easier identification). On the right, the new triangular support replacing port #5 each three sectors is showed.

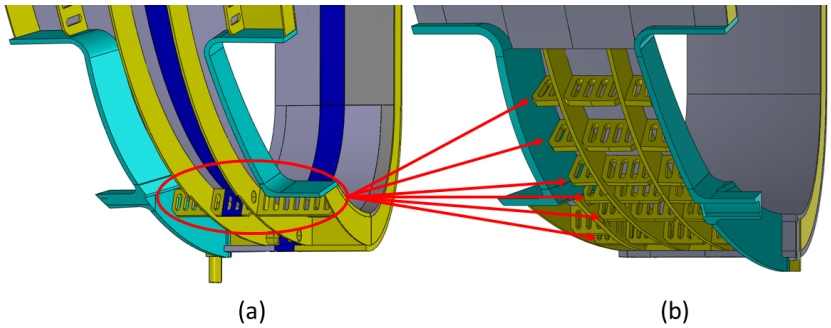

Figure 2.8: Comparison between 2021 (a) regular sectors and 2022 (b) bottom region topologies. The number of toroidal ribs has dramatically increased (six times larger) to provide the necessary structural support to the divertor. On the other hand however, such design penalizes the fluid flow, which results to be much more complex and chaotic, with increased pressure losses. This is indeed a great example of how difficult it is the optimization of Tokamak components.

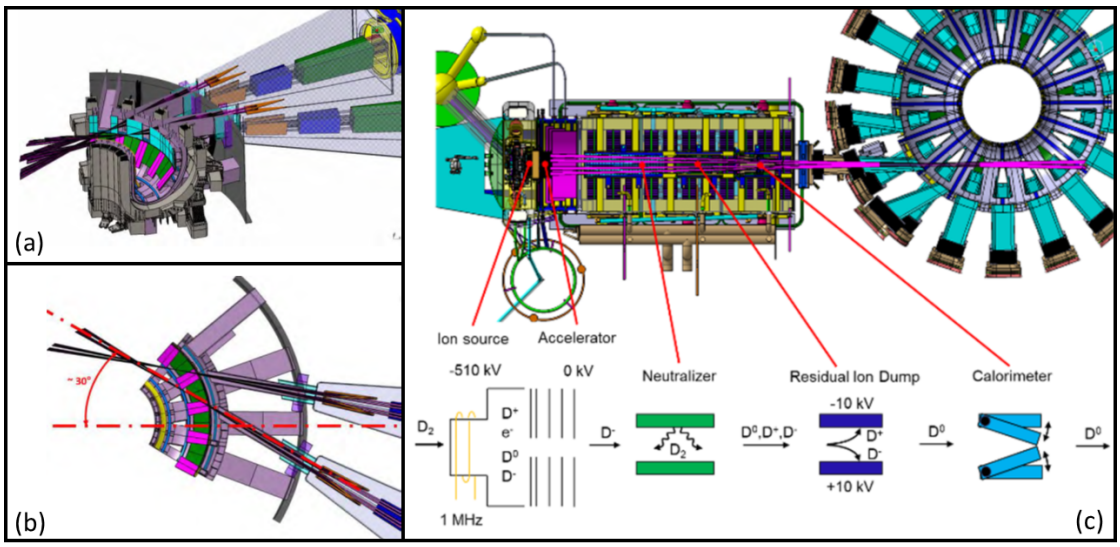

Figure 2.9: Comparison between double-source (a,b) and new single-source (c) DTT NBI configurations. The inclination of the beam has changed (and thus the inclination of the equatorial port hosting the NBI duct) from 30° to 35°. Images reproduced from [4] and [6].

Chapter 3

Setup of the Thermal-Fluid Dynamics Model

"The greatest disaster one can encounter in computation is not instability or lack of convergence, but results that are simultaneously good enough to be believable but bad enough to cause trouble"
Ferzinger, 1993

3.1 Simulation Physics and Objectives

As introduced in the chapters before, the goal of the present work is to characterize the thermal-hydraulic behaviour of each of the 12 control volumes that make up the DTT VV. The need for detailed numerical simulations comes from the necessity to understand if the current design of the VV satisfies a series of qualitative design requirements DSs:

- DS1: The borated water must not go below a minimum temperature of $T_{min} = 313.15$ K causing a possible boron precipitation with consequent deposition and formation of encrustations over the VV components that can damage the structure and partially or even totally occlude passages for the flow.
- DS2: The borated water must not overcome a maximum temperature of $T_{max} = 353.15$ K, accelerating the steel corrosion.
- DS3: The VV must be fully drainable from borated water to allow baking.

Concerning the last point, baking is a process foreseen in the maintenance routine for Tokamak reactors where the VV walls are gas-cooled (by means of nitrogen at

200°C in the specific case of DTT).
The goals of this operation are twice: Richard Pitts, leader of the Plasma-Wall Interactions Group in ITER between 2008-2019, says that baking is essential to loosen all the impurities that have been accumulated during operation in order to guarantee high purity and thus high plasma performances. In addition, the baking process is not solely related to the VV, but it is also used for FW e divertor cleaning where it acts as a detritiation mechanism to keep under control the tritium trapped inventory, subjected to regulatory limits [7]. Hot nitrogen is preferred in DTT VV to avoid high pressures related to baking operation with water, necessary to hinder phase transition of water into steam: for that reason if the VV sectors are not fully drainable water can remain trapped inside, acting as an obstacle to hot nitrogen which can not properly bakes the inner surface of the sector completely.
It must be stressed that a dedicated simulation of the draying process is not foreseen for the present work: DS3 will be evaluated only qualitatively by assessing overall water recirculation regions.
The VV will be subjected to a radiative negative heat load towards the TF coils, which as discussed in the introduction, are kept at around 4.5 [K] to ensure the superconducting state of the conductors. Therefore a thermal-fluid dynamics analyses are needed to assess relevant quantities such as the flow distribution within the control volumes, the pressure drops and the temperature distributions (with identification of possible not optimal hot/cold spots that go against DS1-2).
In order to do that, numerical methods are necessary since the starting point to describe the motion of a viscous fluid are the Navier-Stokes equations which, despite for very simple geometry in a laminar regime, still miss an analytical solution.

The Navier-Stokes equations are a set of non-linear equations that describe the momentum conservation and transport, considering both the advective term (first order derivative in space, non linear) and the diffusion term (second order derivative term). When coupled to the continuity equation, the full set can be condensed in two vectorial equations (incompressible flow hypothesis $\rho = const$, constant properties):

$$\nabla \cdot \mathbf{V} = 0 \tag{3.1}$$

$$-\nabla p + \rho \mathbf{g} + \mu \nabla^2 \mathbf{V} = \rho\Big(\frac{\partial \mathbf{V}}{\partial t} + \mathbf{V} \cdot \nabla \mathbf{V}\Big) \tag{3.2}$$

The problem is well posed and closed, since there are four equations (continuity and momentum conservation along $\mathbf{x} = (x, y, z)$) in four variables (scalar pressure field $p(x, y, z, t)$) and velocity field $\mathbf{V} = \Big(u(\mathbf{x}, t), v(\mathbf{x}, t), w(\mathbf{x}, t)\Big)$.
However a numerical solution is an approximation of the real solution, and therefore *verification* and *validation* are mandatory to assess the goodness of the outputs.
When dealing with numerical methods, and thus numerical solutions, some essential

properties must be considered very carefully. Between the features that a numerical method must satisfy (as *consistency*, *stability*, *convergence*, *conservation*...) there's one that directly capture the physics involved in the problem: the *accuracy* of the solution. In fact, as the discretization of independent variables (space and time) becomes finer and finer, the numerical solution must approach the exact solution. However, the discretization step cannot reach zero in reality and therefore the discretization error cannot be deleted.
On top of that, modelling errors are introduced when simplified geometry and/or boundary conditions are considered, for sake of simplicity or missing information. Therefore, if the convergence of the numerical method is more related to the *verification* of the numerical solution (verify that equations are solved correctly, by means of a mesh independence study for instance), on the other hand the *accuracy* of the solution is also strictly related to the validation process (verify that the solved equations fully capture all the essential features/physics involved in the real problem, by doing comparisons with experimental data if available).
The next sections will be therefore dedicated to the discussion of the physics involved in the TH analyses of the 12 control volumes, in order to justify the choice of the models in the commercial software *Star-CCM+*.

3.2 Flow Regime and Turbulence Closures

When dealing with fluid flows in very complex geometries, as any of the 12 different control volumes that make up the DTT VV, the estimation of the flow regime if far from being simple. From a visual inspection of the geometry it is clear that the borated water will flow macroscopically from bottom to top, but a broad range of possible paths (with several both length and velocity scales) are expected, and the Reynolds number cannot be therefore defined unequivocally. However, the estimation of the flow regime is key to correctly set and solve the Navier-Stokes equations, since in case of turbulent regime additional very efficient momentum (Reynolds stresses) and energy fluxes are introduced as a consequence of the strong mixing done by the vortices (eddies). If these effects are not captured by the model, both computed temperature and pressure distributions may be not representative of the real physics and therefore almost useless.

If the attention is focused on the inlet section for instance, the estimation of the Reynolds number for the circular pipe is possible because both characteristic scale (pipe's diameter $D = 54.76$ [mm]) and mass flow rate ($\dot{m}_{INLET} = 2.22$ [kg/s], see section 3.7 dedicated to boundary conditions for details) are known a priori:

$$\mathrm{Re} = \frac{\rho \bar{u} D}{\mu} = \frac{4\dot{m}_{INLET}}{\mu \pi D} \approx 88000 \tag{3.3}$$

where $\mu = 5.8613 \cdot 10^{-4}$ [Pa s] is the viscosity of borated water at 333.15 [K] evaluated in the section dedicated to thermo-physical properties of borated water 3.10.
In literature, the transition between laminar and turbulent regime for circular pipe is located at $\mathrm{Re} \approx 2100 \div 2500$[1] , meaning that the flow at the inlet section is fully turbulent, and therefore turbulent models and closures are needed.
For what regards other characteristic lengths, the different sectors are characterized by the presence of button-holes (Ø16/20/24x55 [mm]), of semi-rectangular channels (because of the curvature of the torus) connected by circular holes (Ø48 [mm]) in the poloidal ribs (see figure 3.1). In this case, a possible strategy consists of computing the equivalent diameter, or hydraulic diameter, exploiting the cross section crossed by the flow A_F and the wetted perimeter P_W:

$$D_h = \frac{4A_F}{P_W} \tag{3.4}$$

and to insert it in the computation of the Reynolds number.

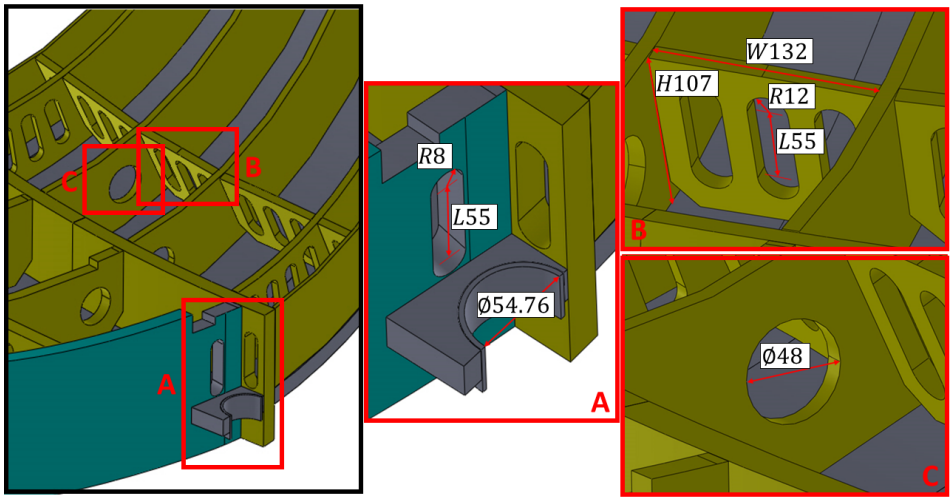

Figure 3.1: Examples of some of the many different characteristic length scales within VV sectors. Reported dimensions in [mm] are approximative.

However, each button-hole, semi-rectangular channel and hole will be characterized by specific velocities (i.e mass flow rates), and the computation of the Reynolds number can become very tedious.
One possible way to grossly assess where the flow is turbulent or not is to consider turbulent descriptors as the turbulent kinetic energy k [J kg^{-1}], whose definition

[1]From "Fundamentals of Fluid Mechanics" Munson, Okiishi, Huebsch, Rothmayer[8].

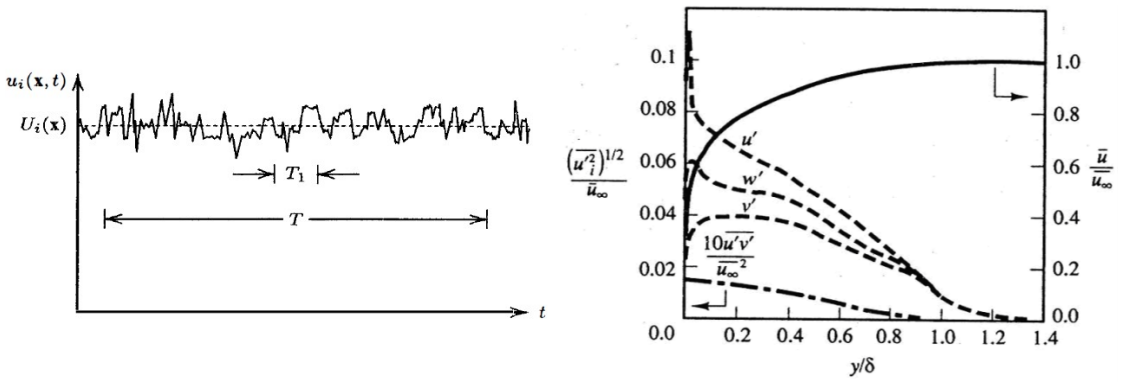

Figure 3.2: (a) Representation of time averaging for stationary turbulence ($\bar{u_i}(\mathbf{x}) \equiv U_i(\mathbf{x})$). The time window T over which integration is performed is chosen to guarantee that $T >> T_1$, where T_1 is the maximum period of the velocity fluctuations. By doing that the average becomes independent of the time. Source: [9]. (b) Evolution of momentum fluxes along the thickness of the boundary layer δ. Source: material of the course "Computational and Thermal Fluid Dynamics" held by prof. Zanino at Politecnico di Torino (2022).

takes into account all the fluctuating components of the velocity $u'(\mathbf{x},t)$, $v'(\mathbf{x},t)$ and $w'(\mathbf{x},t)$ derived from the Reynolds decomposition of the velocity vector components. Following this concept, if a stationary turbulent flow is considered (i.e the mean flow quantities don't vary in time) each instantaneous flow variable can be written as the summation of a time-independent mean value $U_i(\mathbf{x})$ and of a fluctuating term $u'(\mathbf{x},t)$ both space and time dependent (see figure 3.2(a)):

$$u_i(\mathbf{x},t) = U_i(\mathbf{x}) + u_i'(\mathbf{x},t) \tag{3.5}$$

where the mean value is evaluated as:

$$U_i(\mathbf{x},t) = \lim_{T\to\infty} \frac{1}{T} \int_t^{t+T} u_i(\mathbf{x},t)\mathrm{dt} = \bar{u}_i(\mathbf{x},t) \tag{3.6}$$

to filter out the turbulent motion.
Therefore, the turbulent kinetic energy is defined as the summation of the momentum fluxes (time and space dependencies are not shown explicitly for sake of brevity):

$$k = \frac{1}{2}\overline{(u' \cdot u' + v' \cdot v' + w' \cdot w')} \tag{3.7}$$

which can be condensed exploiting the Einstein's notation:

$$k = \frac{1}{2}\overline{u_i' \cdot u_i'} \tag{3.8}$$

The turbulent kinetic energy is not the only one turbulent descriptor, if one would like to focus the attention on a specific fluctuating component, the momentum fluxes can be normalized to the reference mean flow velocity $\overline{u_\infty}$ obtaining thus a measure of the turbulence intensity:

$$T_i \propto \frac{\overline{(u_i')^2}^{\frac{1}{2}}}{\overline{u_\infty}} \tag{3.9}$$

However, one of the key points derived from experimental analysis of simple turbulent flows (as flat plate boundary layer), is that near the wall the turbulence production is maximized because of large gradients in the mean flow, but exactly at the wall the turbulence is dumped, being the latter not exempt from no-slip or impermeable wall conditions (see figure 3.2(b)). Therefore, sections of the turbulent kinetic energy scalar field in *Star-CCM+* are needed to visualize inside the fluid domain and to fully capture regions characterized by remarkable turbulent kinetic energy production.

Having assessed that the flow is turbulent (at least at inlet and outlet regions a priori), special treatment of the Navier-Stokes equation is needed to take into account the bidirectional relation derived from the fact that additional turbulent momentum fluxes, generated from the shear in the mean flow, have an effect in turn on mean flow characteristics. A detail review of all the turbulent models developed in literature is far beyond the scope of this work, but it is worth mentioning that different strategies have been developed to treat and characterize turbulence according to the desired level of accuracy and flexibility.
The accuracy (and thus the computational cost) and the flexibility are actually key-aspects during the choice of the turbulent model, but unfortunately they typically compete between each other: as the desired level of accuracy increases, the flexibility of the model decreases.
Accuracy in turbulence modelling is mainly related to the range of scales that the model is able to capture: the chaotic, three-dimensional and unsteady rotating structures (eddies from now on) that characterize the turbulence exist over a wide range of different scales, which interact with the mean flow and between each other, exchanging energy in the so-called energy cascade process.
This information is efficiently summarized in the energy spectrum distribution (spectral energy E_{sp} [$\mathrm{m^3\,s^{-2}}$]) of turbulence theorized by the mathematicians Andrej Nikolaevič Kolmogorov, as a function of the wave number $2\pi/L$ of the eddies, where L is the characteristic length, as reported in figure 3.3.
From the energy spectrum it can be noticed that most of the energy is contained in the larger scale: this actually the key reasoning behind the turbulence model of **RANS** type (Reynolds-Averaged Navier-Stokes), where the attention is focused only on mean flow characteristics, without investigating the eddies structures.

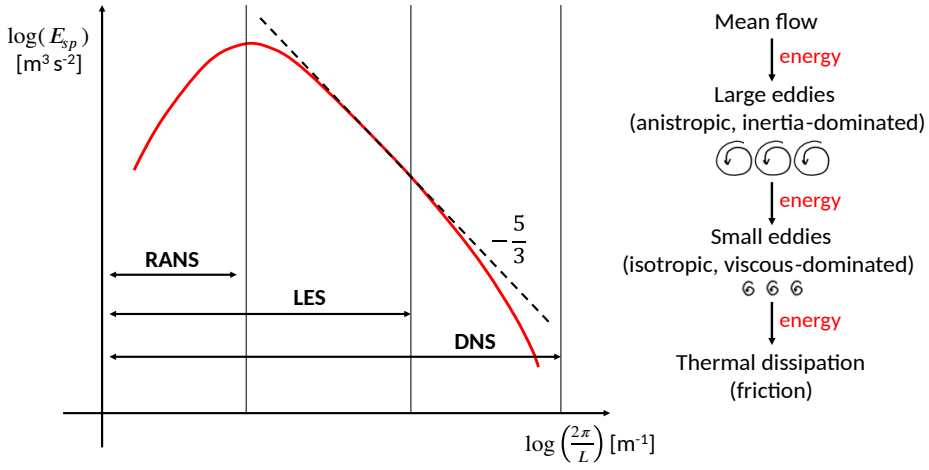

Figure 3.3: Vortex stretching: the process over which the turbulent kinetic energy is transferred form larger to smaller eddies, where it is finally dissipated at the level of molecules. For that reason, turbulent flows are always dissipative.

This kind of turbulence modelling is by far the easiest and the most flexible among the existing ones, and it is typically sufficient to correctly predict relevant engineering quantities for industrial applications.
As can be appreciated in figure 3.3, two additional families of turbulent models are available: the Large Eddy Simulation **LES** and the Direct Numerical Simulation **DNS**. The former aims at describing at least the behaviour of the largest eddies (smallest frequencies) exploiting then sub-grid scale models to consider smaller length scales, while the latter explores all the different scales down to the Kolmogorov's one.
In these two cases, the computational cost increases remarkably, since all simulation will be intrinsically three dimensional and transient. As a positive side-effect though, the accuracy of the solution increases, and in case of DNS it can actually be considered equivalent to a short laboratory experiment.

In view of the requested outcomes for the VV characterization, turbulence models of RANS type are preferred because of the winning trade-off between accuracy and computational cost, but it must be stressed that this is not always the case.
In the next lines, a quick derivation of Reynolds-Averaged Navier-Stokes equations is presented with the goal of understanding how these equations are managed by the commercial software *Star-CCM+*, in order to correctly select the models during the setup of the different simulations.

3.3 Turbulence Modelling

As previously introduced, the starting points for TH simulations are the mass and momentum conservation equations for an incompressible flow, which can be elegantly written exploiting the Einstein's notation as:

$$\frac{\partial u_i}{\partial x_i} = 0 \tag{3.10}$$

$$\rho\frac{\partial u_i}{\partial t} + \rho u_j\frac{\partial u_i}{\partial x_j} = -\frac{\partial p}{\partial x_i} + \frac{\partial}{\partial x_j}\left(2\mu s_{i,j}\right) + b_i \tag{3.11}$$

Where b_i is a generic momentum source (which can include the body force as an effect of the gravity acceleration $f_{g,i} = \rho g_i$, in this case some books modify the definition of pressure so that the static pressure is incorporated with the pressure due to fluid motion), and $s_{i,j}$ is the symmetric strain-rate tensor:

$$s_{i,j} = \frac{1}{2}\left(\frac{\partial u_i}{\partial x_j} + \frac{\partial u_j}{\partial x_i}\right) \tag{3.12}$$

After having performed the time-averaging, the Reynolds-Averaged equations of motion in conservation form are obtained:

$$\frac{\partial \overline{u_i}}{\partial x_i} = 0 \tag{3.13}$$

$$\rho\frac{\partial \overline{u_i}}{\partial t} + \rho\frac{\partial}{\partial x_j}\left(\overline{u_j u_i} + \overline{u_j' u_i'}\right) = -\frac{\partial P}{\partial x_i} + b_i + \frac{\partial}{\partial x_j}\left(2\mu S_{i,j}\right) \tag{3.14}$$

where P and $S_{i,j}$ are the mean value of pressure and the mean strain-rate tensor respectively, according to the Reynolds decomposition:

$$p = P + p'$$
$$s_{i,j} = S_{i,j} + s'_{i,j}$$

It can be noticed that the time averaged rate of momentum transfer due to turbulence $\overline{u_j' u_i'}$ survives the integration in time, and it is exactly here where the problem of modelling turbulence is hidden: these additional terms, that can be interpreted as additional stresses influencing the behaviour of the mean flow, are unknown and therefore extra equations (namely turbulence closures) must be introduced to close the problem. To underline the nature of these terms the momentum equation is typically re-arranged in the following form:

$$\rho\frac{\partial \overline{u_i}}{\partial t} + \rho\overline{u_j}\frac{\partial \overline{u_i}}{\partial x_j} = -\frac{\partial P}{\partial x_i} + \rho g_i + \frac{\partial}{\partial x_j}\left(2\mu S_{j,i} + T_{\mathrm{RANS}_{i,j}}\right) \tag{3.15}$$

where $T_{\mathrm{RANS}_{i,j}} = -\rho\overline{u_i' u_j'} = \rho\tau_{i,j}$ is the symmetric Reynolds stress tensor (3x3 matrix, six unknows).
There are several turbulence closures available in literature, and they are classified according to the number of additional transport equations added to the original formulation of the problem. *Star-CCM+* deals with the T_{RANS} term in two different ways, by means of Eddy viscosity models or Reynolds stress transport models.
The attention will be focused on the first type of model only, where the Reynolds stress tensor is written exploiting the introduction of an eddy viscosity μ_t through the so-called *Boussinesq assumption*:

$$T_{\mathrm{RANS}_{i,j}} = 2\mu_t S_{i,j} - \frac{2}{3}\mu_t \frac{\partial \overline{u_k}}{\partial x_k}\delta_{i,j} - \frac{2}{3}\rho k \delta_{i,j} \tag{3.16}$$

Where k is the turbulent kinetic energy and $\delta = \begin{cases} 1, i = j \\ 0, i \neq j \end{cases}$ is the Kronecker delta while repeated subscript k indicates summation in tensor notation.
The Boussinesq assumption simply consists in the hypothesis of considering the normal stresses isotropic, with a linear dependence with respect to shear of the mean flow, which is already proven to be not true for simple 2D flows like the flat plate boundary layer example (see figure 3.2(b)), where turbulence intensities have different magnitudes.
The eddy viscosity is not a physical property of the fluid, but it depends mainly on the characteristic of the flow and on the position. Within the turbulence models that relay on this assumption, the k-Epsilon and k-Omega models are the most widely exploited and validated two-equations turbulence closures, and they are both available in the commercial software *Star-CCM+*.
The choice of one model over the other actually requires some justifications, since one model could perform better with respect to another in a specific situation. For the present work, the choice of a strain stress transport $SST\ k-\omega$ derives from three main considerations:

1. The good performances of the turbulent model in the thermal-hydraulic simulation of a regular sector in the work done by the NEMO group in 2021 [5].

2. Better prediction of the heat transfer coefficient in stagnation regions, where the $k-\varepsilon$ is known to overestimate the turbulence providing non conservative solutions.

3. Reduced computational cost with respect to more complex and expensive turbulence closures as the seven equations Reynolds Stress Transport.

Moreover, the Menter's $SST\ k-\omega$ combined with an *all* y^+ treatment is the recommended choice by *Star-CCM+* among $k-\omega$ models, but a dedicated section will address the wall treatment in details.

3.4 The $k-\omega$ and $SST\ k-\omega$ Turbulence Models

The standard $k-\omega$ model is based on A.N Kolmogorov intuition [10], back in 1942, to express the turbulence length scale l by means of the velocity scale $k^{\frac{1}{2}}$ and of a specific dissipation rate ω as:

$$l \propto \frac{k^{\frac{1}{2}}}{\omega} \tag{3.17}$$

The version adopted by CFD codes today, with all its extensions, is formally described in D.C Wilcox book [9].
The model introduces two additional transport model equations for the turbulent kinetic energy k budget and for the specific dissipation rate or turbulent frequency ω [s^{-1}], obtained by combining together the turbulent kinetic energy k [$\mathrm{J\,kg}^{-1}$] and the turbulent dissipation ε [$\mathrm{J\,kg}^{-1}\,\mathrm{s}^{-1}$] as:

$$\omega = \frac{1}{C_\mu}\frac{\varepsilon}{k} \tag{3.18}$$

with $C_\mu = 0.09$.
The two model equations are reported in *Star-CCM+* user's manual as follows:

$$\frac{\partial}{\partial t}(\rho k) + \nabla \cdot \left(\rho k \overline{\mathbf{V}}\right) = \nabla \cdot \left[\left(\mu + \sigma_k \frac{\rho k}{\omega}\right)\nabla k\right] + P_k - \rho\beta^* f_{\beta^*}(\omega k - \omega_0 k_0) \tag{3.19}$$

$$\frac{\partial}{\partial t}(\rho \omega) + \nabla \cdot \left(\rho \omega \overline{\mathbf{V}}\right) = \nabla \cdot \left[\left(\mu + \sigma_\omega \frac{\rho k}{\omega}\right)\nabla \omega\right] + P_\omega - \rho\beta f_\beta\left(\omega^2 - \omega_0^2\right) \tag{3.20}$$

they are classical transport equations with a transient term, production/sink term, advective (first order) and diffusion (second order) transport terms.
More specifically P_k and P_ω are production terms; σ_k, σ_ω, β^*, β are model coefficients and f_{β^*}, f_β are the free-shear modification factor and the vortex-stretching modification factor respectively. The terms ω_0, k_0 are defined as "*ambient turbulence values*" and have been discussed in [11].
In the standard $k-\omega$ model, the production terms include the following quantities:

$$P_k = G_k + G_b \tag{3.21}$$

$$P_\omega = G_\omega \tag{3.22}$$

Without going to much in details (for which the *Star-CCM+* user manual is suggested) the production terms consider production of turbulent kinetic energy or of turbulent frequency by several phenomena: G_k represents the "most classical way" for turbulent kinetic energy production, related to the shear in the mean flow according to the already discussed Boussinesq assumption as:

$$G_k = \mu_t S^2 - \frac{2}{3}\rho k \nabla \cdot \overline{\mathbf{V}} - \frac{2}{3}\mu_t \left(\nabla \cdot \overline{\mathbf{V}}\right)^2 \rightarrow \rho \tau_{i,j} \frac{\partial u_i}{\partial x_j} \tag{3.23}$$

Being S the magnitude of mean strain-rate tensor $S_{i,j}$.
The variable G_b instead takes into account the production of turbulent kinetic energy as a consequence of buoyancy (if the case):

$$G_b = \beta_v \frac{\mu_t}{\mathrm{Pr}_t} \left(\nabla \overline{T} \cdot \mathbf{g}\right) \tag{3.24}$$

where the volumetric thermal expansion coefficient β_v has to be specified by the user when the Boussinesq model is selected, and Pr_t is the turbulent Prandtl number. Dedicated sections will address the definitions of these last two terms in details.
As far as G_ω is concerned, its definition is given as:

$$G_\omega = \rho\alpha \left[\left(S^2 - \frac{2}{3}\left(\nabla \cdot \overline{\mathbf{V}}\right)^2\right) - \frac{2}{3}\omega \nabla \cdot \overline{\mathbf{V}}\right] \rightarrow \alpha \frac{\omega}{k} \rho \tau_{i,j} \frac{\partial u_i}{\partial x_j} \tag{3.25}$$

To close the system of equations, the eddy viscosity is written as a function of both k and ω:

$$\mu_t = \rho \frac{k}{\omega} \tag{3.26}$$

Here it can be appreciated one of the greatest advantage of the model in the standard formulation, which doesn't require wall damping functions: in the viscous-dominated region at the wall in fact $\omega \rightarrow \infty$ is expected but the sensitivity of arbitrarily setting large values of ω has proven to be totally negligible on final results, removing therefore additional possible source of inaccuracies derived by the employment of wall functions when adverse pressure gradients exist (see empirical damping functions needed in the viscous sub-layer for the $k-\varepsilon$ model). The two model transport equations revisited formulation by Wilcox [12] appear as:

$$\frac{\partial}{\partial t}(\rho k) + \frac{\partial}{\partial x_j}(\rho u_j k) = \rho \tau_{i,j} \frac{\partial u_i}{\partial x_j} - \beta^* \rho k \omega + \frac{\partial}{\partial x_j}\left[\left(\mu + \sigma^* \frac{\rho k}{\omega}\right) \frac{\partial k}{\partial x_j}\right] \tag{3.27}$$

$$\frac{\partial}{\partial t}(\rho \omega) + \frac{\partial}{\partial x_j}(\rho u_j \omega) = \alpha \frac{\omega}{k} \rho \tau_{i,j} \frac{\partial u_i}{\partial x_j} - \beta \rho \omega^2 + \sigma_d \frac{\rho}{\omega} \frac{\partial k}{\partial x_j} \frac{\partial \omega}{\partial x_j} + \frac{\partial}{\partial x_j}\left[\left(\mu + \sigma \frac{\rho k}{\omega}\right) \frac{\partial \omega}{\partial x_j}\right] \tag{3.28}$$

These are model equations since the six constants α, β^*, σ^*, β, σ_d, σ have been assessed by fitting several experimental data, and are therefore known coefficients tuned to match experimental results:

$$\alpha = \frac{\beta_0}{\beta^*} - \frac{\sigma_\omega \kappa^2}{\sqrt{\beta^*}} = \frac{13}{25}\ , \beta = \beta_0 f_\beta\ , \beta^* = \frac{9}{100}\ , \sigma = \frac{1}{2}, \sigma^* = \frac{3}{5}$$

$$\sigma_d = \begin{cases} 0, \frac{\partial k}{\partial x_j}\frac{\partial \omega}{\partial x_j} \leq 0 \\ \frac{1}{8}, \frac{\partial k}{\partial x_j}\frac{\partial \omega}{\partial x_j} > 0 \end{cases}$$

$$\beta_0 = 0.0708, \quad f_\beta = \frac{1 + 85\ \chi_\omega}{1 + 100\ \chi_\omega}\ , \quad \chi_\omega = \left| \frac{\Omega_{i,j}\Omega_{j,k}S_{k,i}}{(\beta^*\omega)^3} \right|$$

Being $\Omega_{i,j}$ and $S_{k,i}$ the mean rotation and the mean strain-rate tensors respectively:

$$\Omega_{i,j} = \frac{1}{2}\left(\frac{\partial \bar{u_i}}{\partial x_j} - \frac{\partial \bar{u_j}}{\partial x_i}\right), S_{i,j} = \frac{1}{2}\left(\frac{\partial \bar{u_i}}{\partial x_j} + \frac{\partial \bar{u_j}}{\partial x_i}\right) \tag{3.29}$$

Again it is worth mentioning that an in deep analysis of the $k-\omega$ model is far beyond the scope of this work and of the expertise of the author: if the reader curiosity may claim for additional info, there are no better resources than Wilcox publications and books or the constantly updated NASA dedicated website on turbulence modelling [13].
The definition of the kinematic eddy viscosity also slightly changes, where the stress-limiter modification appears:

$$\nu_t = \frac{k}{\widetilde{\omega}}\ , \quad \widetilde{\omega} = max\left\{\omega,\ C_{lim}\sqrt{\frac{2S_{i,j}S_{i,j}}{\beta^*}}\right\}, \quad C_{lim} = \frac{7}{8} \tag{3.30}$$

The latter allows to limit the magnitude of the eddy diffusivity when the production of turbulence energy exceeds its dissipation (condition known as "*non-equilibrium flow*", due to large pressure gradients responsible of possible onset of flow separation) resulting in improved incompressible flow predictions: further details are available in [14].
The second most relevant addition is the presence of the cross-diffusion term $CD_\omega = \sigma_d \frac{\rho}{\omega}\frac{\partial k}{\partial x_j}\frac{\partial \omega}{\partial x_j}$, already exploited by Menter in its $SST\ k-\omega$ model to reduce sensitivity to free-stream value of ω.
To help the understanding, it is worth mentioning that the general formulation presented by Wilcox can be retrieved from the one used in *Star-CCM+* by setting the free-shear modification factor $f_{\beta^*} = 1$ (i.e by activating the cross-diffusion limiter option in the standard $k-\omega$ model options, which in turn introduces the cross-diffusion term CD_ω in the ω transport equation) and by assuming null ambient turbulence values and no buoyancy contributions.Moreover, model coefficients

appears under different symbols (left *Star-CCM+*, right Wilcox [12]):

$$\sigma_k \equiv \sigma^*$$
$$\sigma_\omega \equiv \sigma$$
$$\beta \equiv \beta_0$$

And the mean strain-rate tensor $\mathbf{\Omega}$ is identified as $\mathbf{W}$ in *Star-CCM+*.
Despite the improvements, the user's manual points out that validation results of the revised formulation cover mainly two dimensional simple flows and therefore the revised formulation *"should be used with caution"*: it means that each correction is not set as a default option in the standard $k-\omega$ model, but it has to be selected manually by the user.
Looking to turbulence closures from an historical point of view, despite the $k-\omega$ intuition by A.N Kolmogorov in 1942, the $k-\varepsilon$ model developed by Saiy in 1974 can be considered the initiator of two-equation turbulence closures. Indeed the limitations of the latter (turbulent shear over-prediction, poor performance in swirling flows etc.) pushed Wilcox in 1988 to develop the first version of the $k-\omega$ model, improving in a remarkable way boundary layer computation.
On the other hand however, as already seen before, the $k-\omega$ model introduced an unpleasant sensitivity on final results to ω free-stream values.
In 1994 Dr. Florian Menter [15] succeed in developing a new turbulence closure capable of sensibly reduce the drawbacks of the original $k-\omega$ model. He derived the ω transport equation by doing a variable substitution, exploiting the known identity between ω and ε (3.18), from the original ε transport equation finding out an additional term not present in Wilcox's ω equation:

$$2\frac{\rho\sigma_{\omega_2}}{\omega}\nabla k\cdot\nabla\omega = 2\frac{\rho\sigma_{\omega_2}}{\omega}\left(\frac{\partial k}{\partial x}\frac{\partial\omega}{\partial x}+\frac{\partial k}{\partial y}\frac{\partial\omega}{\partial y}+\frac{\partial k}{\partial z}\frac{\partial\omega}{\partial z}\right) \tag{3.31}$$

This additional term is nothing but the cross-diffusion term discussed before in the latest release of the $k-\omega$, used to reduce effectively the sensitivity to arbitrarily defined free-stream ω values; the model coefficient is equal to $\sigma_{\omega_2}=0.856$.
To simplify at maximum, Menter tried to couple the main advantages of both $k-\omega$ (e.g better performances near the wall) and $k-\varepsilon$ models (e.g less sensitive to arbitrary free-stream assumptions) by means of an hybrid model able to switch from one model to the other via blending functions. In fact by introducing a blending function F_1, it is possible to smoothly shift from the two models:

$$2\left(1-F_1\right)2\frac{\rho\sigma_{\omega_2}}{\omega}\nabla k\cdot\nabla\omega = D_\omega \tag{3.32}$$

In *Star-CCM+* when the $SSTk-\omega$ model is selected the production term P_ω is modified by adding the term above:

$$P_\omega = G_\omega + D_\omega \tag{3.33}$$

When $F_1 = 0$, the $k - \varepsilon$ model is exploited (outer layer), alternatively ($F_1 = 1$) the $k - \omega$ is used (sublayer and logarithmic region).
The blending function F_1 is a scalar function that assumes a specific value, between zero and one, in each cell of the computational domain. To assess the scalar field, in the definition of F_1 the distance from the closest wall d is exploited: in case of stationary meshes (as for this work) the F_1 distribution can be computed once at the beginning of the simulation while for moving or adaptive meshes it has to be evaluated each time.
In *Star-CCM+* the blending function appears as follows:

$$F_1 = \tanh\left(\left[\min\left(\max\left(\frac{\sqrt{k}}{0.09\omega d}, \frac{500\nu}{d^2\omega}\right), \frac{2k}{d^2 CD_{k,\omega}}\right)\right]^4\right) \tag{3.34}$$

Where $CD_{k,\omega}$ is the cross-diffusion coefficient, limited by the following statement:

$$CD_{k,\omega} = \max\left(\frac{1}{\omega}\nabla k \cdot \nabla\omega, 10^{-20}\right) \tag{3.35}$$

The blending function it is also used to weight the model coefficients appearing in equations 3.19 and 3.20 as:

$$\sigma_k = F_1\sigma_{k_1} + (1 - F_1)\,\sigma_{k_2},\ \sigma_{k_1} = 0.85,\ \sigma_{k_2} = 1$$
$$\sigma_\omega = F_1\sigma_{\omega_1} + (1 - F_1)\,\sigma_{\omega_2},\ \sigma_{\omega_1} = 0.5,\ \sigma_{\omega_2} = 0.856$$
$$\beta = F_1\beta_1 + (1 - F_1)\,\beta_2,\ \beta_1 = 0.075,\ \beta_2 = 0.0828$$
$$\beta^* = F_1\beta_1^* + (1 - F_1)\,\beta_2^*,\quad \beta_1^* = 0.09,\ \beta_2^* = 0.09 \rightarrow \beta^* = 0.09$$

while $f_{\beta^*} = f_\beta = 1$, being the free-shear modification already included in the SST model and the vortex-stretching modification not available.
Menter noticed that its base model still tend to overestimate wall shear stresses, delaying or even totally hindering flow separation in presence of adverse pressure gradients. To avoid that, a *viscosity limiter* was introduced in the definition of the eddy viscosity for the turbulence time scale T_t:

$$\mu_t = \rho k \cdot T_t = \rho k \cdot \min\left(\frac{\alpha^*}{\omega}, \frac{a_1}{SF_2}\right) \tag{3.36}$$

being:

$$\alpha^* = F_1\alpha_1^* + (1 - F_1)\,\alpha_2^*,\ \alpha_1^* = 1, \alpha_2^* = 1 \rightarrow \alpha^* = 1$$
$$a_1 = 0.31$$

and F_2 another blending function:

$$F_2 = \tanh\left(\left(\max\left(\frac{2\sqrt{k}}{\beta^*\omega d}, \frac{500\nu}{d^2\omega}\right)^2\right)\right) \tag{3.37}$$

So as the wall is approached, the wall distance d decreases while the blending function F_2 increases limiting therefore the turbulent viscosity and the turbulent shear stress.
At this point one may argue that the computation of two additional blending functions and the modification of the eddy viscosity could represent a price in terms of computational efforts witch is not balanced by the avoided free-stream dependency. This observation could be considered even more justified for the problem under investigation, where the flow is completely confined within inner and outer shells of the VV. However, Menter himself reiterates that both blending functions have to be computed only once for stationary meshes and that the added modifications, which surely represents an additional programming effort at the beginning, do not affect overall computing time and codes' numerical stability once they have been implemented.

Durbin P.A. (1996) [16] noticed however that two-equation models ($SST\ k-\omega$ with viscosity limiter included) still over-predicts turbulent kinetic energy in stagnation regions, which are not consistent with experimental observations and that can affect the accuracy of the overall solution. This issue, known as "*Stagnation Anomaly*", is a consequence of large strain rate $S_{i,j}$ which may lead to negative normal component of the Reynolds stress $\overline{u_i' u_j'} = -2\nu_t S_{i,j} - \frac{2}{3}k\delta_{i,j}$, as explained in [17].
To limit that, Durbin proposed a "*realizability*" constraint, which imposes a lower limit on the large-eddy turbulence time scale T_t, implemented in *Star-CCM+* as follows:

$$T_t = \min\left(\frac{1}{\max\left(\frac{\omega}{\alpha^*}, \frac{SF_2}{a_1}\right)},\ \frac{C_T}{\sqrt{3}\ S}\right) \tag{3.38}$$

This feature is a default choice in *Star-CCM+* known as *Durbin Scale Limiter*, where the realizability coefficient is set to $C_T = 0.6$. Even if the problem under investigation does not suggest extreme care for tricky stagnation regions (which would be the case, for instance, of airfoil aerodynamics characterization at the leading edge), the realizability option has been kept activated.

To conclude, it is worth mentioning the way the production term P_k is expressed for the SST model:

$$P_k = G_k + G_b + G_{nl} \tag{3.39}$$

In addition to the term G_k and G_b already discussed before[2], the term G_{nl} includes inside one of the most relevant modifications of the $k-\omega$. The term G_{nl} in fact, where the subscript "nl" stands for non-linear, permits to include anisotropy of turbulence removing the strong simplification of the Boussinesq assumption.
This can be done through quadratic and cubic constitutive relations: following the user's manual, the former improves secondary flows prediction while the latter improves sensitivity to streamline curvature. An investigation of non linear constitutive relations effect on final results is far from being the main objective of the present work, but it could be considered as an interesting topic for future works. For this reason, the Boussinesq assumption, which is the default option, has been used as a constitutive relation for the TH analysis.
In the section dedicated to wall treatment (3.9), the way $k-\omega$ deals with rough walls will be discussed together with the definition of standard and blended wall functions.

3.5 Buoyancy Effect

Having discussed the need for a turbulence model and the reasons behind the specific choice of the turbulent closure, additional physics have to be discussed in order to fully prepare the thermal-fluid dynamics simulations.
First of all, as already anticipated, the flow of borated water will move globally in the vertical direction, being the inlet and outlet located at the bottom and at the top of each control volume respectively. For that reason, the effect of gravity should be taken into account when computing the fluid dynamics solution, because the flow has to win the inlet-outlet difference in height in addition to the pressure losses due to friction, as can be easily understood by applying the first law of thermodynamics for an incompressible flow between CV's boundaries, ignoring the thermal related aspects as a first approximation:

$$\frac{P_{out}}{\rho g}+\frac{V_{out}^2}{2g}+z_{out}=\frac{P_{in}}{\rho g}+\frac{V_{in}^2}{2g}+z_{in}-h_l \tag{3.40}$$

The inlet and the outlet pipes are characterized by the same diameter, and from the continuity equation it is derived that $\dot{m}_{INLET}=\dot{m}_{OUTLET}$ therefore the terms related to kinetic contributions cancel out each other, resulting in a outlet pressure

[2]Actually G_k has a slightly different expression with different model coefficients for the *SST* $k-\omega$ model, for details check *Star-CCM+* user's manual. The different expression doesn't upset the physical intuition behind, which is the reason why this aspect has not been investigated deeply.

for the control volume defined as:

$$P_{out} = P_{in} - \rho g \cdot (\Delta z + h_l) \tag{3.41}$$

Where h_l takes into account the head losses due to friction and $\Delta z = z_{out} - z_{in} = 3905$ [mm] takes into account the difference between inlet and outlet elevation (geodetic height).
However, it must be stressed that most probably the cooling circuit will be a closed one, with the borated water continuously recirculated. In this case of course, the different elevation between inlet and outlet is not relevant, because in a closed circuit the different elevation is always compensated.
To compute the pressure losses related to friction only it is sufficient to subtract the hydrostatic pressure ($\rho g \Delta z$) to the computed pressure drops.

However, the effect of gravity must be included mainly for another reason, which is related to the thermal part of the problem. In fact, due to the negative radiative load acting on the outer wall of the VV, the borated water will cool down, with consequent variations of the density. Density gradients, in a gravitational fields, result in modified body forces which could be the driver of natural convective flows inside the VV: since they actively participate to the energy exchange, they should be correctly captured by the model.
The possibility of including density gradients and thus buoyancy forces actually goes against the initial hypothesis of incompressible flow: in this cases to enhance the convergence of the simulation while limiting as much as possible the complexity of the model, the Boussinesq model can be exploited.
The latter simply neglects any density variation in the terms of the momentum conservation equation except for the one where the acceleration due to gravity appears. The variation in density is modelled by means of the volumetric thermal expansion coefficient β_v [K^{-1}], which is a thermodynamic property of the fluid that provides a measure of density variation in response to temperature variation at constant pressure.
The rigorous definition of β_v can be approximated by the following form:

$$\beta_v = -\frac{1}{\rho}\left(\frac{\partial \rho}{\partial T}\right)_{p=const} \approx -\frac{1}{\rho}\frac{\rho_\infty - \rho}{T_\infty - T} \tag{3.42}$$

Where ρ_∞ and T_∞ are the density and the temperature of the fluid outside the boundary layer. From this relation the core of the Boussinesq approximation is obtained:

$$\rho_\infty - \rho \approx \beta_v \cdot \rho \cdot (T - T_\infty) \tag{3.43}$$

From a more practical point of view, it means that a relation for the density as a function of temperature is introduced in the definition of body forces due to

buoyancy acting on the finite volume of fluid:

$$\rho(T) = \rho_0 \cdot 1 - \beta_v \Delta T \tag{3.44}$$

$$\mathbf{f}_g = \rho_0 \cdot \mathbf{g} \cdot \beta_v \cdot (T - T_0) \tag{3.45}$$

where ρ_0 is the reference value of density at the reference operating temperature T_0. Concerning the latter, by substituting the Boussinesq approximation in the momentum equation the reference density cancels itself out, as shown in the simplified 2D example:

$$\rho\left(u\frac{\partial u}{\partial x} + v\frac{\partial u}{\partial y}\right) = g\left(\rho_0 - \rho\right) + \mu\frac{\partial^2 u}{\partial y^2}$$

$$\downarrow$$

$$\rho\left(u\frac{\partial u}{\partial x} + v\frac{\partial u}{\partial y}\right) = \rho g \beta_v \left(T - T_0\right) + \mu\frac{\partial^2 u}{\partial y^2}$$

The reference temperature T_0 is therefore the only relevant quantity that has to be specified for the numerical simulations.
For the problem under investigation, the latter coincides with the design inlet temperature of 333.15 [K], from which all the density variations are computed.
If the default value of 293.15 [K] is left, the buoyancy forces will be overestimated and, being the expected minimum temperature larger than 293.15 [K], buoyancy forces will also have a positive sign, helping the fluid to flow from bottom to top and therefore reducing the pressure drops with respect to the isothermal case.
Instead, being the thermal driver -70 [$\mathrm{W\,m^{-2}}$] for the simulations (see section dedicated to boundary conditions 3.7), the fluid will cool down and the buoyancy forces (negative) will further pull down the fluid towards its way up, increasing the expected pressure drop.

It must be stressed that the Boussinesq approximation is valid only for small temperature differences and thus density variations, and that the coefficient β_v must be taken from appropriate property tables.
As far as the first warning is concerned, it has been already computed that the surface integral over the regular sector outer wall surface of the TS radiative load of -70 [$\mathrm{W\,m^{-2}}$] results in a total power of ≈ 395 [W] [5].
If a mass flow rate of 1.11 [$\mathrm{kg\,s^{-1}}$] of borated water with specific heat $c = 4019.68$ [$\mathrm{J\,kg^{-1}\,K^{-1}}$] (see section 3.10 for material properties) is considered, and the contribution of pressure is neglected, from the first law of thermodynamics it can be derived that:

$$-\Phi = \dot{m}c\left(T_{in} - T_{out}\right)$$

$$T_{in} - T_{out} = -\frac{\Phi}{\dot{m}c} \approx -\frac{-395}{1.11 \cdot 4019.68} \approx 0.09[\mathrm{K}]$$

Such a limited temperature gradient between inlet and outlet satisfy the first constraint and it can justify also the initial hypothesis of constant fluid properties. For the second warning instead, in literature there are no available data regarding the computation of β_v for solutions of borated water as a function of temperature and boron concentration. In absence of better values therefore, the volumetric thermal expansion of pure water at 333.15 [K] is considered as input for the Boussinesq approximation implementation in *Star-CCM+*:

$$\beta_{v_{water}}\,(@333.15\ [\mathrm{K}]) = 5.82 \cdot 10^{-4}\ [\mathrm{K}^{-1}] \tag{3.46}$$

If that value of β_v is considered, then the constraint suggested by *Star-CCM+* for the Boussinesq approximation validity is largely satisfied:

$$\beta_v \Delta T \approx 5.82 \cdot 10^{-4} \cdot 0.1 \ll 1 \tag{3.47}$$

By non-dimensionalizing the governing equations of free convection, the Grashof dimensionless parameter is obtained:

$$\mathrm{Gr}_L = \frac{g\beta_v \left(T_\infty - T_s\right) L^3}{\nu^2} \tag{3.48}$$

Where $\nu = \mu/\rho$ is the kinematic viscosity of the fluid, T_s is the temperature of the surface lapped by the fluid and T_∞ is the bulk temperature of the fluid.
The Grashof number is a measure of the ratio between buoyancy and viscous forces acting on the fluid and it is usually compared with the Reynolds number in order to assess the relevance of natural convection over forced convection.
More specifically, if the ratio $\mathrm{Gr}_L/\mathrm{Re}_L^2$, known as Richardson number Ri, is much lower than one, then the effect of natural convection could be neglected.
For this reason, it makes sense to perform an exploring simulation considering the effect of gravity by selecting "*Gravity*" and "*Boussinesq model*" in the model selection window of *Star-CCM+* then, where possible, the Reynolds and the Grashof number could be compared in order to quantify the relevance or not of free-convection.
This is a key aspect because when buoyancy forces are involved in the numerical model it is generally preferred to exploit a coupled approach rather than a segregated one; the former though is much more computationally expensive and the eventuality of neglecting the free-convection could open up the possibility for computational cost reduction (i.e segregated solver).
Exploiting the definition of Reynolds and Grashof number, the Richardson number can be approximated as:

$$\mathrm{Ri} = \frac{\mathrm{Gr}_L}{\mathrm{Re}_L^2} = \frac{\frac{g\beta_v(T_\infty - T_s)L^3\rho^2}{\mu^2}}{\frac{\rho^2\bar{u}^2L^2}{\mu^2}} \approx \frac{g\beta_v \left(T_{in} - T_{f,wall}\right) L_{max}}{\bar{u}^2} \tag{3.49}$$

Where the surface temperature T_s is replaced by the fluid temperature at the wall $T_{f,wall}$ (since no solids are considered at this stage), the bulk temperature T_∞ is replaced by the fluid inlet temperature T_{in} and for the characteristic length the local equivalent diameter of the geometry is considered.
By imposing the lowest temperature at the wall $T_{f,wall,min} \approx 332$ [K] (see chapter 4), the largest equivalent diameter $L_{max} \approx 216$ [mm] (that corresponds to the central path OB2 on the outboard leg at the equatorial plane) and the lowest average velocity $\bar{u} = 0.006$ [$\mathrm{m\,s^{-1}}$], the largest possible Richardson number is obtained:

$$\mathrm{Ri}_{max} = \frac{9.81 \cdot 5.82 \cdot 10^{-4} \cdot (333.15 - 332) \cdot 0.216}{0.006^2} = 39 \tag{3.50}$$

It must be stressed that the Richardson number found above is not really representative of the problem since the different terms appearing in its definition are

not necessarily strictly correlated between each other. Instead, they are picked up on purpose from different parts of the computational domain so that its value is maximized.
The magnitude of such number (much larger than one) suggests however the need for a more detailed evaluation of the Richardson number across the computational domain, using this time values that are physically correlated.
To do that, a local Richardson map can be generated over different slices of the computational domain at different heights: in each slice the dimensionless number can be approximated by considering the largest equivalent diameter $L_{max} \approx 216$ [mm], the difference between minimum and average temperature $\left(\overline{T_k} - T_{min,k}\right)$ over the cross-section k and the average velocity $\overline{u}_k$, always evaluated on the same cross-section:

$$\mathrm{Ri}_k = \frac{g\beta_v \left(\overline{T_k} - T_{min,k}\right) L_{max}}{\overline{u}_k{}^2} \tag{3.51}$$

The choice of considering the largest characteristic length, independently of the specific channel under investigation, derives from the fact that there's not built-in report in *Star-CCM+* to automatically compute the perimeter of a constrained plane section, fundamental ingredient for the hydraulic diameter definition.
It could be possible to export the constrained plane and then evaluate its perimeter in a CAD software but, since the characteristic length appears with exponent one in the Richardson expression, the effect of considering only one value for each channel is limited, and in any case, it always represents a conservative assumption.

With all of that being said, the resulting Richardson map is reported in table 3.1.
The largest value, computed in the upper region of the outboard channel number three, is not far from the largest Richardson number estimated previously.
As further confirmation of this result, it can be demonstrated that by considering specifically the equivalent diameter $L_{OB3,up} \approx 0.157$ [mm], the Richardson number in this region becomes equal to $\mathrm{Ri} = 14$. The updated value is still larger than one, meaning that for the thermal-fluid dynamics problem under investigation the contribution of buoyancy forces must not be neglected.
A coupled approach as global solution strategy is therefore recommended to correctly capture such complex flow in one hand, but on the other hand it hinders the possibility to save computational resources with a segregated solver .
In the next section, a more comprehensive discussion about *Star-CCM+* available solvers is presented: a full understanding of how the CFD software operates is key to ensure goodness of results but also to speed up convergence process towards solution.

CHANNEL		T_{min} [K]	$T_{average}$ [K]	$V_{average}$ [m/s]	L_{max} [m]	g [m/s^2]	β_v [1/K]	Ri [-]
IB1	bottom	332.86	333.13	0.021	0.216	9.81	5.82E-04	0.80
	eq.	333.06	333.12	0.0432				0.04
	up	332.82	333.09	0.0180				1.03
IB2	bottom	332.73	333.09	0.0067				9.82
	eq.	333.06	333.07	0.0144				0.06
	up	332.67	333.02	0.0062				11.18
IB3	bottom	332.86	333.13	0.0328				0.31
	eq.	333.06	333.13	0.0382				0.06
	up	332.80	333.10	0.0171				1.30
OB1	bottom	332.65	333.09	0.0167				1.96
	eq.	332.58	333.05	0.0116				4.31
	up	332.60	333.05	0.0147				2.61
OB2	bottom	332.69	333.11	0.0142				2.57
	eq.	332.61	333.09	0.0079				9.33
	up	332.54	333.08	0.0077				11.26
OB3	bottom	332.96	333.14	0.0263				0.32
	eq.	332.62	333.08	0.0092				6.84
	up	332.53	333.04	0.0057				19.28

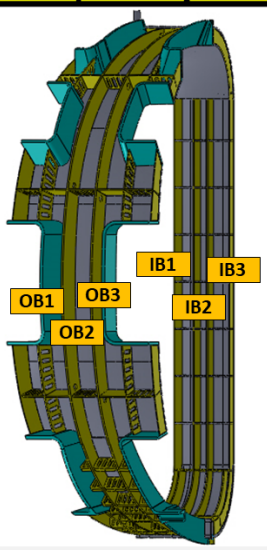

Table 3.1: Richardson number evaluated at different sections of the computational domain. Results are taken from control volume CV1, medium mesh. See section 4.1.5 for details on the definition of the different cross-sections and section 4.1.4 for meshes definition.

3.6 *Star-CCM+* Coupled Solver and Energy and Time Modelling

Software like *Star-CCM+* exploit finite volume method to discretize governing equation in space. The advantage of a finite volume method over finite differences or finite elements methods is the possibility to ensure conservation of fundamentals quantities as mass and energy. By doing that, governing equations are written in a conservative form and then integrated over each final volume, applying Gauss's divergence theorem.
As an example, when considering the general transport equation of the scalar quantity Φ, the conservative form on a finite volume dV becomes:

$$\frac{d}{dt}\int_V \rho\Phi \ \mathrm{dV} + \int_A \rho\Phi\mathbf{V}\cdot\hat{\mathbf{n}} \ \mathrm{dA} = \int_A \Gamma\nabla\Phi\cdot\hat{\mathbf{n}} \ \mathrm{dA} + \int_V S_\Phi \ \mathrm{dV} \tag{3.52}$$

where $\frac{d}{dt}\int_V \rho\Phi \ \mathrm{dV}$ represents the rate of change in time of the scalar quantity in the control volume, $\int_A \rho\Phi\mathbf{V}\cdot\mathbf{n} \ \mathrm{dA}$ the advective/convective flux over the boundary surfaces of the discrete volume (which are identified by the locally perpendicular versor $\mathbf{n}$), $\int_A \Gamma\nabla\Phi\cdot\mathbf{n} \ \mathrm{dA}$ the diffusive flux (where Γ identifies a diffusivity) and

finally $\int_V S_\Phi \, \mathrm{dV}$ the generation/sink term of the scalar quantity inside the control volume.
The global conservation is ensured only if robust approximation of integrals and integrands are adopted to guarantee local conservation, but a detailed discussion of quadrature formulae and interpolation schemes lies outside the intended objectives of this Master Thesis.
The mass, momentum and energy equations for fluids are implemented in *Star-CCM+* in the following integral forms respectively:

$$\frac{\partial}{\partial t}\int_V \rho \, \mathrm{dV} + \int_A \rho \mathbf{V} \cdot \hat{\mathbf{n}} \, \mathrm{dA} = 0 \tag{3.53}$$

$$\frac{\partial}{\partial t}\int_V \rho \mathbf{V} \, \mathrm{dV} + \int_A (\rho \mathbf{V} \cdot \mathbf{V} + \sigma) \cdot \hat{\mathbf{n}} \, \mathrm{dA} = \int_V \mathbf{f_b} \, \mathrm{dV} \tag{3.54}$$

$$\frac{\partial}{\partial t}\int_V \rho E \, \mathrm{dV} + \int_A \rho H \mathbf{V} \cdot \hat{\mathbf{n}} \, \mathrm{dA} = -\int_A \mathbf{q}'' \cdot \hat{\mathbf{n}} \, \mathrm{dA} + \int_A (\mathbf{T} \cdot \mathbf{V}) \cdot \hat{\mathbf{n}} \, \mathrm{dA} + \int_V \mathbf{f_b} \cdot \mathbf{V} \, \mathrm{dV} + \int_V S_E \, \mathrm{dV} \tag{3.55}$$

being:

$$\sigma = -p\mathbf{I} + \mathbf{T} = -p \begin{bmatrix} 1 & 0 & 0 \\ 0 & 1 & 0 \\ 0 & 0 & 1 \end{bmatrix} + \mu \begin{pmatrix} 2\frac{\partial u}{\partial x} & \frac{\partial u}{\partial y} + \frac{\partial v}{\partial x} & \frac{\partial u}{\partial z} + \frac{\partial w}{\partial x} \\ \frac{\partial v}{\partial x} + \frac{\partial u}{\partial y} & 2\frac{\partial v}{\partial y} & \frac{\partial v}{\partial z} + \frac{\partial w}{\partial y} \\ \frac{\partial w}{\partial x} + \frac{\partial u}{\partial z} & \frac{\partial w}{\partial y} + \frac{\partial v}{\partial z} & 2\frac{\partial w}{\partial z} \end{pmatrix} \tag{3.56}$$

the stress tensor constitutive equation for incompressible Newtonian fluids, where p is the fluid pressure (normal stresses) and $\mathbf{T}$ is the viscous stress tensor (shear stresses proportional to the fluid viscosity μ). The latter provide a closure between stress tensor and fluid velocity field.
The term $\mathbf{f_b}$ collects all the possible body forces: in the specific case under consideration, the only relevant term is the body force due to gravity $\mathbf{f_g}$ introduced during the Boussinesq assumption derivation.
As far as the energy equation is concerned, it is derived by putting together the equation for the internal energy conservation e and the equation for the mean flow kinetic energy k:

$$\begin{cases} \frac{\partial(\rho e)}{\partial t} + \nabla \cdot (\rho \mathbf{V} e) = -\nabla \cdot \mathbf{q}'' + S_e \\ \frac{\partial(\rho k)}{\partial t} + \nabla \cdot (\rho \mathbf{V} k) = \nabla \cdot (\sigma \cdot \mathbf{V}) + \rho \mathbf{g} \cdot \mathbf{V} \end{cases} \tag{3.57}$$

obtaining an equation for the total energy $E = e + k$:

$$\frac{\partial (\rho E)}{\partial t} + \nabla \cdot (\mathbf{V} \cdot (\rho E + p)) = -\nabla \cdot \mathbf{q}'' + S_e + \nabla \cdot (\mathbf{T} \cdot \mathbf{V}) + \rho \mathbf{g} \cdot \mathbf{V} \tag{3.58}$$

which is then integrated over each volume as shown previously, incorporating the term $\rho\mathbf{g}$ in the more general vector of body forces $\mathbf{f_b}$ (which can include electromagnetic forces...).
The variable E is related to the total enthalpy H as:

$$E = H - \frac{p}{\rho} \tag{3.59}$$

where in turn the total enthalpy is obtained from the isentropic arrest condition (stagnation), by adding the mean flow kinetic energy per unit of mass:

$$H = h + \frac{|\mathbf{V}^2|}{2} \tag{3.60}$$

The variable h is the static enthalpy, which is a function of temperature:

$$h = c(T - T_0) + h_0 \tag{3.61}$$

Solving for the total enthalpy means to derive the temperature field.
More in details, the term $\int_A (\mathbf{T} \cdot \mathbf{V}) \cdot \hat{\mathbf{n}}\ \mathrm{dA}$ in the total energy equation expresses the viscous work (viscous dissipation): it is important to stress that the viscous stress tensor $\mathbf{T}$ refers to the dissipation of mean flow kinetic energy due to viscosity only, and it does not include the additional Reynolds stresses due to turbulence, which are responsible of the turbulent kinetic energy dissipation. The term $-\int_A \mathbf{q}'' \cdot \hat{\mathbf{n}}\ \mathrm{dA}$ is the heat conduction term, being $\mathbf{q}''$ the heat flux vector computed from the Fourier's law:

$$\mathbf{q}'' = -\lambda \nabla T$$

which is derived from the differential form of the energy conservation equation for a moving fluid after the application of the Gauss' theorem:

$$\nabla \cdot (\lambda \nabla T) \rightarrow \int_A \lambda \nabla T \cdot \hat{\mathbf{n}}\ \mathrm{dA}$$

As for momentum and continuity equations, also the advection-diffusion total energy equation requires to be averaged when turbulence is introduced, in order to find the mean flow temperature field. Following the same concepts analysed before, the partial differential equation of the total energy can be averaged in time after the Reynolds decomposition, assuming no volumetric energy source as for the problem under investigation:

$$\frac{\partial\left(\rho\overline{E}\right)}{\partial t} + \nabla \cdot \left(\overline{\mathbf{V}} \cdot \left(\rho\overline{E} + P\right)\right) = -\nabla \cdot \overline{\mathbf{q}''} + \nabla \cdot \left(\overline{\mathbf{T}} + \mathbf{T_{RANS}}\right) \cdot \overline{\mathbf{V}} + \mathbf{f_b} \cdot \overline{\mathbf{V}} \tag{3.62}$$

where $\overline{E}$ and $\overline{\mathbf{q}''}$ are the mean total energy and mean heat flux vector respectively:

$$E = \overline{E} + E' \tag{3.63}$$

$$\mathbf{q}'' = \overline{\mathbf{q}''} + (\mathbf{q}'')' \tag{3.64}$$

If the definition of total energy is introduced, the mean temperature can be highlighted, but again both velocity field and temperature fluctuating components will survive the averaging process, resulting in additional unknown terms:

$$
\begin{aligned}
&\rho c\left(\frac{\partial \overline{T}}{\partial t}+\overline{u}\frac{\partial \overline{T}}{\partial x}+\overline{v}\frac{\partial \overline{T}}{\partial y}+\overline{w}\frac{\partial \overline{T}}{\partial z}\right) && \Big\} \text{ advection}\\
&=\lambda\left(\frac{\partial^2 \overline{T}}{\partial x^2}+\frac{\partial^2 \overline{T}}{\partial x^2}+\frac{\partial^2 \overline{T}}{\partial x^2}\right) && \Big\} \text{ diffusion}\\
&\quad-\rho c\left(\frac{\partial \overline{u'T'}}{\partial x}+\frac{\partial \overline{v'T'}}{\partial y}+\frac{\partial \overline{w'T'}}{\partial z}\right) && \Big\} \text{ turbulent heat transport}\\
&\quad+\mu\left(2\left(\frac{\partial \overline{u}}{\partial x}\right)^2+2\left(\frac{\partial \overline{v}}{\partial y}\right)^2\right. && \Bigg\}\\
&\quad\left.+2\left(\frac{\partial \overline{w}}{\partial z}\right)^2+\left(\frac{\partial \overline{v}}{\partial z}+\frac{\partial \overline{w}}{\partial y}\right)^2\right) && \Big\} \text{ direct dissipation}\\
&\quad+\mu\left[2\overline{\left(\frac{\partial u\prime}{\partial x}\right)^2}+2\overline{\left(\frac{\partial v\prime}{\partial y}\right)^2}\right. && \Bigg\}\\
&\quad+2\overline{\left(\frac{\partial w}{\partial z}\right)^2}+\overline{\left(\frac{\partial u\prime}{\partial y}+\frac{\partial v\prime}{\partial x}\right)^2} && \Big\} \text{ turbulent dissipation}\\
&\quad\left.+\overline{\left(\frac{\partial u\prime}{\partial z}+\frac{\partial w\prime}{\partial x}\right)^2}+\overline{\left(\frac{\partial v\prime}{\partial z}+\frac{\partial w\prime}{\partial y}\right)^2}\right] && \Bigg\}
\end{aligned}
$$

Where $\overline{T}$ is the mean temperature and T' the fluctuating part:

$$T(t)=\overline{T}+T'(t) \tag{3.65}$$

The energy equation is formally identical to the laminar one except for two additional terms: the turbulent heat transport ($\overline{u_i'T'}$) and the turbulent dissipation ($\rho\widetilde{\varepsilon}$), which is exactly the concept of energy cascade discussed before.
It means, from a pure mathematical point of view, that in addition to the Reynolds stresses, $\overline{u_i'T'}$ and $\rho\widetilde{\varepsilon}$ are two additional unknows.
Almost all turbulence models, $SST\ k-\omega$ included, rely on the concept of constant turbulent Prandtl number to solve that inconvenience.
The turbulent Prandtl number is an additional input required for the thermal-hydraulic simulation in *Star-CCM+* and in appendix A the reasoning behind the choice of this value will be derived from simpler 2D turbulent flow.

In a coupled approach, the governing equations are efficiently condensed together as:

$$\frac{\partial}{\partial t}\int_V \mathbf{W}\ \mathrm{dV} + \int_A [\mathbf{F}-\mathbf{G}]\cdot\hat{\mathbf{n}}\ \mathrm{dA} = \int_V \mathbf{H}\ \mathrm{dV} \tag{3.66}$$

with:

$$\mathbf{W} = \begin{bmatrix}\rho\\ \rho\mathbf{V}\\ \rho E\end{bmatrix},\ \mathbf{F} = \begin{bmatrix}\rho\mathbf{V}\\ \rho\mathbf{V}\cdot\mathbf{V}+p\mathbf{I}\\ \rho H\mathbf{V}+p\mathbf{V}\end{bmatrix},\ \mathbf{G} = \begin{bmatrix}0\\ \mathbf{T}\\ \mathbf{T}\cdot\mathbf{V}+\mathbf{q}''\end{bmatrix},\ \mathbf{H} = \begin{bmatrix}0\\ \mathbf{f_b}\\ S_E\end{bmatrix}$$

and solved once without the exploitation of iterative procedures as in a segregated global solution strategy, like the SIMPLE algorithm.
As already mentioned above, the coupled solver is more computational expensive, but since no iterative procedures are foreseen, the convergence is safer.

As far as the time modelling is concerned, there are no strong indications that the thermal-fluid dynamics solution is unsteady being the forcing functions (negative radiative load from TS) and material properties constant over time (see section 3.7 dedicated to boundary conditions and section 3.10 on material properties).
In case of steady-state model selection, the coupled energy model exploits a pseudo-time-marching approach: the time derivative is substituted by a pseudo-transient term which is progressively pushed towards zero.
The coupled implicit solver specifically, which is the default option, discretizes the set of equations in time with an Euler implicit scheme, with "*Automatic Courant-Friedrichs-Lewy*" (CFL) number selection. The automatic selection tries to identify the best CFL compromise between number of iterations needed to reach convergence and the requested time to solve each iteration, ranging from minimum (0.1) and maximum (100000) default constraints.
There's a strong conceptual parallelism between the coupled solver CFL number and the under relaxation factors of the segregated one. Concerning the maximum constraint, it is of interest to stress that unphysical values much larger than one are possible because the problem is steady: intermediate solutions don't have to be time-accurate. Larger CFL value could speed up the convergence of the implicit solver, but too high values can lead to oscillations which can hinder the convergence (stability bounds are exceeded and the software starts introducing limitation on min/max temperature/pressure).
The optimal CFL choice is a function of several parameters as mesh quality and body forces' magnitudes, and there are no general laws to easily identify optimal values.

In order to further speed up the convergence, which is quite slow due to the mass imbalance between inlet and outlet mass flow rates, the continuity convergence accelerator (CCA) is exploited.

Without going to much in details, the CCA introduces a pressure correction equation to correct the face mass fluxes, minimizing cell mass imbalances at each iteration, improving the continuity convergence. The CCA under relaxation factor can be tuned in order to further improve the convergence, avoiding possible oscillations or even divergence.
With the coarse mesh ($\approx$ 1.8 million cells, see section 4.1.4), the hydraulic solution converges in less than 10000 iterations starting directly with the coupled energy solver.
As far as the medium or finer meshes are concerned instead, the discretized equations are much more sensible to the physics and to the CFL number selected, and in order to obtain convergence it is strongly advised to initialize the solution with the results from coarser meshes or to solve for pressure and velocity fields separately before the introduction of the energy equation, letting the latter to start from a more reasonable and coherent initial hydraulic condition.
Moreover, small values of CFL (< 200) are needed to avoid residuals' explosions and or variables' max/min bounds introduction: it is strongly advised to shift the CFL control from "*Automatic*" to "*Constant*".
A conservative value CFL$= 5$ has been proven to be reliable also for the finest mesh but such small value requires lots of iterations ($\approx$ 100000) to reach convergence.
Anyhow, to find the best CFL control strategy is far from the scope of this work but it could be considered a priority in the future to speed up thermal-fluid dynamics analyses of possible next designs.

3.7 Boundary Conditions

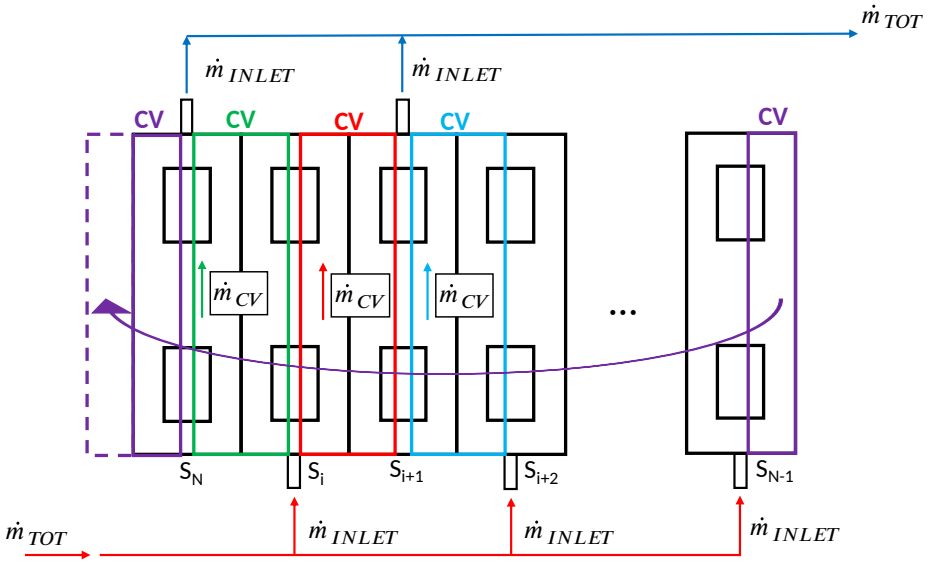

Figure 3.4: Schematic representation of initially guessed mass flow rate distribution within the control volumes. By doing that, each control volume is characterized separately, ignoring the existing pressure coupling at inlets and outlets.

According to the operating parameters presented in the DTT "*Green Book*" [4] and in [5], a total mass flow rate $\dot{m}_{TOT} = 20$ [kg s^{-1}] is assumed in the 18 sectors of the VV. As already discussed in previous chapters, the number of inlets (and thus outlets) has been reduced to 9 only, with a staggered arrangement.
As a first guess, which has to be validated by thermal-fluid dynamics simulations, it is assumed that the total mass flow rate is perfectly distributed among the inlet pipes, with a resulting value at each inlet of $\dot{m}_{INLET} = 2.22$ [kg s^{-1}].
Moreover, it is also assumed initially that the mass flow rate of each inlet is equally distributed in the two adjacent control volumes: the prescribed mass flow rate in half of the inlet pipe is therefore equal to $\dot{m}_{CV} = 1.11$ [kg s^{-1}]. A schematic representation of the VV is presented in figure 3.4 to clarify the mass flow rates initially guessed distribution.
It must be stressed that these hypotheses were particularly appropriate in [5] because of the perfect mirrored symmetry between adjacent regular control volumes sharing the same inlet pipe. With the latest update of the VV geometry however (19/10 REV03), it has been already shown how this time adjacent control volumes are characterized by different geometries and therefore not equal hydraulic resistance is expected a priori.

Going more in details, each control volume is characterized by multiple surfaces and, being the original set of partial differential equations parabolic, then proper boundary conditions must be specified in all the boundaries of the computational domain.
The boundary conditions (BCs from now on) applied can be divided in two families according to the piece of physics that they refer to and, within the same family, macroscopic BCs (which involve global quantities) and local BCs (which refer to a specific part or subsets of the computational domain) are further distinguished:

- **Hydraulic BCs**:
  - Macroscopic:
    1. BC of "*Mass Flow Inlet*" type with a prescribed mass flow rate of 1.11 [$\mathrm{kg\,s^{-1}}$] at the inlet pipe.
    2. BC of "*Pressure Outlet*" type at the outlet section.
  - Local:
    1. BC of "*Wall*" type with "*smooth*" wall surface specification for all the surfaces in contact with the VV structure.
    2. BC of "*Symmetry Plane*" type for the vertical cross section of inlet/outlet pipes.
- **Thermal BCs**:
  - Macroscopic:
    1. Prescribed uniform inlet temperature of 333.15 [K].
  - Local:
    1. Prescribed heat flux of -70 [$\mathrm{W\,m^{-2}}$] as thermal specification for the surfaces of the fluid in contact with the outer wall of the VV (both inboard and outboard legs).
    2. Adiabatic BC for all the remaining surfaces: for the two vertical cross sections of inlet and outlet pipes this condition holds automatically in view of the imposed symmetry condition.

A detailed close up of prescribed BCs is presented in figure 3.5.
All the thermo-physical properties of the fluid have been evaluated at the operating condition foreseen for the VV operation (333.15 [K] and 4 [bar]) when possible, as reported in the dedicated section 3.10.
The total temperature T_{tot} prescribed at the inlet corresponds to the static temperature T, being the Mach number (Ma) small and the flow incompressible

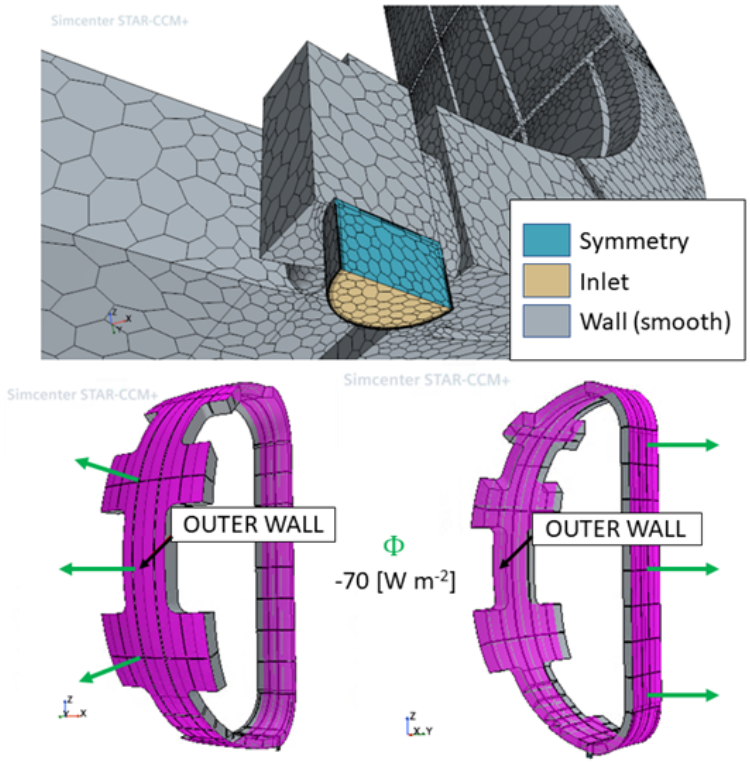

Figure 3.5: Close-up of different BCs at the inlet section (top) and visualization of the constant and uniform heat flux Φ acting on the Outer Wall (bottom).

(Ma < 0.3):

$$T_{tot} = T\left(1 + \frac{\gamma - 1}{2}\mathrm{Ma}^2\right), \ \gamma = \frac{c_p}{c_v}$$
$$\mathrm{Ma} = \frac{V_{INLET}}{c} = \frac{\frac{\dot{m}_{INLET}}{\rho A}}{c} \approx 0.0006$$
$$T_{tot} \equiv T$$

Being $c = 1552$ [m s^{-1}] the speed of sound for water at 60 °C [18].
At the outlet, a "*Pressure Outlet*" BC is chosen, imposing the desired working pressure. Being the gravity included in the model, the working pressure field function P_w (gauge) coincides with the relative piezometric pressure $P_{piezo,rel}$; the latter is defined taking into account also the hydrostatic pressure P_{hydro} in addition to the static relative pressure $P_{static,rel}$ as:

$$P_w = P_{static,rel} + P_{hydro} = P_{static,rel} - \rho g(z - z_0) \tag{3.67}$$

The imposition of the working pressure must therefore take into account the hydrostatic contribution, or alternatively, the pressure field has to be scaled down

coherently during the post-processing.
It is of interest to stress that the choice of the reference altitude z_0 is in theory arbitrary; however for numerical stability it is suggested to set the reference altitude exactly at the centre of the computational domain, in order to obtain a symmetric hydrostatic pressure distribution (positive and negative values) around zero.
In addition, the choice of a "*Pressure Outlet*" rather than simple "*Outlet*" BC comes from the fact that, for the second one, reverse flow is avoided a priori and relevant flow variables at the boundary are derived based solely on what happens upstream. This condition is not optimal because at the outlet the elongation of the pipe in the original CAD is comparable to the diameter, and a fully developed velocity profile is very unlikely to exist. In fact, reverse flow occurs.
In that case, such condition implies a non uniform distribution of pressure at the outlet and, for this reason, the computed surface average pressure can differ from the imposed one. That will in turn affect the pressure drop evaluation, being the latter defined as the difference between surface average reports of absolute pressure at inlet and outlet sections.
Moreover, in case of reverse flow at the outlet, also the temperature must be defined, because it will affect the overall advective energy flux through the boundary.
As already analysed before, by applying the first law of thermodynamics over the entire control volume, a ΔT of around 0.1 [K] is expected between inlet and outlet. For that reason, a Tout=333.05 [K] should be imposed at the outlet for the fluid that enters the domain in case of backflow.
This last condition in particular is not optimal, because it could be seen as a strategy to force the expected integral energy balance of the control volume, hiding possible discrepancies in the numerical solution.
To avoid uncomfortable situations dictated by reverse flow, the outlet pipe has been elongated to reach a total length corresponding to three-times the pipe's diameter, proven to be sufficient for the flow to re-organize itself in a almost fully developed condition (i.e no reverse flow).
To conclude, it is worth reporting two additional considerations:

1. Being the flow regime turbulent, proper boundary conditions have to be discussed wisely also for turbulence quantities (e.g turbulence intensity, turbulence length scale etc. . .). Next section will address this specific point in details.

2. By modelling the fluid volume only (no conjugate heat transfer) the solution will be a conservative one since additional thermal resistance introduced by solid walls is neglected. Moreover, the fact of neglecting that parallel channels in the CV are thermally coupled (increased diffusive mechanism that can smooth out the temperature field, levelling possible hot/cold spots) represents again a simplistic but conservative choice.

3.8 Inlet Turbulence Specification

In sections 3.3 and 3.4 turbulence modelling by means of RANS has been introduced, with a specific focus on $k-\omega$ two equation model. However, it has not been stressed that both k and ω model equations are partial differential equations (PDEs from now on) which require proper BCs.
Specifically, turbulence values have to be prescribed at inlet and outlet sections, at the interface with solid walls and also at the interface with free-stream if any.
However, definition of such quantities is far from being trivial. Each boundary in fact, requires a proper strategy/reasoning:

- For an inflow boundary, both k and ω (or ε) profiles must be prescribed, but most of the time they might be not available. In *Star-CCM+* several turbulence specifications are at disposal: the user can impose directly k and ω profiles (or constant values) or alternatively she/he can specify quantities such as turbulence intensity and viscosity ratio, which are then automatically translated into k and ω values. By default the CFD code will prescribe constant values of $k = 0.001$ $[\mathrm{J\,kg^{-1}}]$ and $\omega = 1e^{-4}$ $[\mathrm{s^{-1}}]$, which of course have no specific meaning at all.
  The best option available, in absence of experimental values, is to simulate a fully developed flow within the inlet pipe of the CV, in order to prescribe fully developed velocity, k and ω profiles at the inlet for the TH simulation.

- For an outflow boundary instead, it is recommended to impose the weakest BC possible (i.e homogeneous Neumann) to avoid artificial boundary layers.

- At the interface with solid walls, as it will be discussed in section 3.9, *High Reynolds* or *Low Reynolds* approaches are available in general depending on the refinement of the mesh near the wall. It is exactly at this stage that one of the greatest advantage of the $k-\omega$ model becomes undeniable: the negligible sensitivity of arbitrarily high ω values at the wall prevents the introduction of additional uncertainties related to wall damping functions exploitation.

- At the interface with the free-stream turbulence values must be prescribed. As seen in section 3.4, the SST $k-\omega$ model switch to $k-\varepsilon$ model in this region to avoid Standard $k-\omega$ disadvantages.

In general, it's always a good practice to check the sensitivity of boundary conditions modification on final solution.
This is indeed the final goal of this section, namely to compute proper inlet profiles to be prescribed at the inflow boundary of the TH simulation. Each sector of the VV, no matter if regular or special, is characterized by the same inlet pipe and by the same inlet mass flow rate (as supposed in the section dedicated to

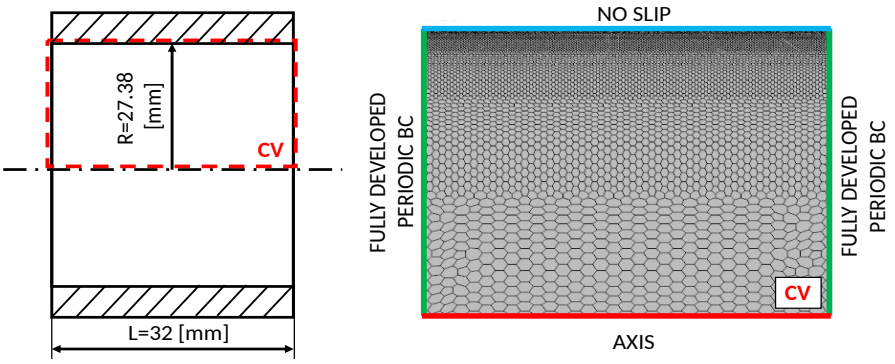

Figure 3.6: Schematic representation of the simulated control volume (inlet) with BCs and mesh visualization.

boundary condition 3.7). For this reason, inlet turbulence interesting profiles can be computed once and then prescribed for each CV.
The inlet pipe has a cylindrical shape, with an inner diameter $D = 54.76$ [mm], and for this reason an axis-symmetric solution is expected. This is a good news which allows to reduce the dimensionality of the problem (from 3D x, y, z reference system to 2D cylindrical r, z reference system) simulating only half of the inlet section as shown in figure 3.6.
As far as the physics of the problem is concerned, pure hydraulic simulation was performed with a segregated solver to reduce the computational burden.
This choice is justified from the fact that no radiative loads are foreseen at inlet pipe's external surface for the TH simulation.
Gravity contribution has also been neglected in view of the limited elongation of the inlet pipe in the vertical direction.
Fully developed conditions are achieved by means of periodic interfaces between inlet and outlet sections, which allow to drastically reduce the axial extension of the numerical domain: from experiments with confined viscous flow the ratio between the entry length L_{FD} and the pipe diameter D in turbulence regime is approximated as follows[3]:

$$\frac{L_{FD}}{D} = 4.4 \cdot \mathrm{Re}^{\frac{1}{6}} \tag{3.68}$$

It means that, for the case under consideration, a minimum length of $L_{FD} = 0.05574 \cdot \left(4.4 \cdot 88000^{\frac{1}{6}}\right) \approx 1.6$ [m] should be considered while only few centimeters have been simulated. The numerical savings are not negligible therefore.

[3]From "Fundamentals of Fluid Mechanics" Munson, Okiishi, Huebsch, Rothmayer[8].

Some care must be reserved to the imposition of the mass flow rate at the inlet: for an axis-symmetric simulation at the inlet the mass flow rate per radian must be specified:

$$\dot{m}_{rad} = \frac{\dot{m}_{INLET}}{2\pi} = \frac{2.22}{2\pi} = 0.353 \ [\mathrm{kg\,rad^{-1}\,s^{-1}}]$$

Three meshes (3000, 10000, 120000 cells respectively) have been investigated to conduct the grid independence study, while in figure 3.7 below velocity, turbulent kinetic energy and specific dissipation rate profiles are shown:

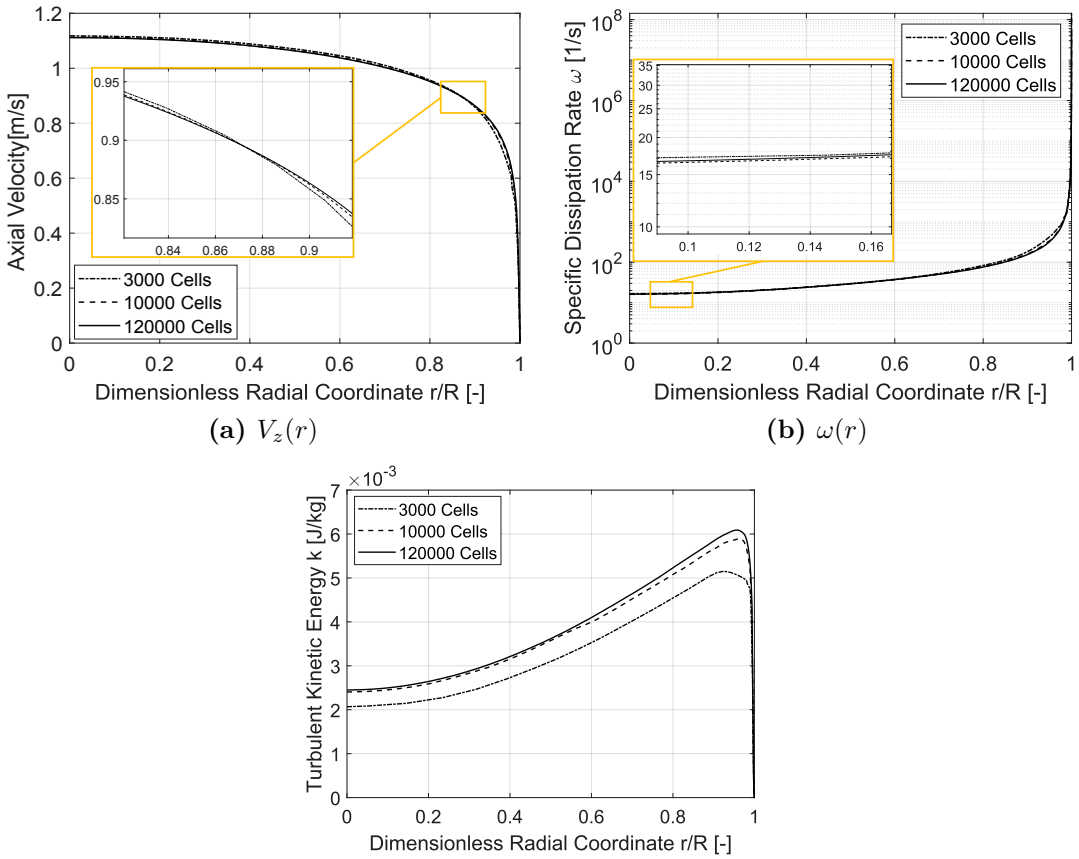

(a) $V_z(r)$ **(b)** $\omega(r)$

(c) $k(r)$

Figure 3.7: Axial Velocity (a), Specific Dissipation Rate (b) and Turbulent Kinetic Energy (c) profiles obtained at the inlet pipe in a fully developed condition.

3.9 Wall Treatment, Wall Functions and Roughness Modelling

3.9.1 Wall Function Derivation and Prism Layer Mesh Setup

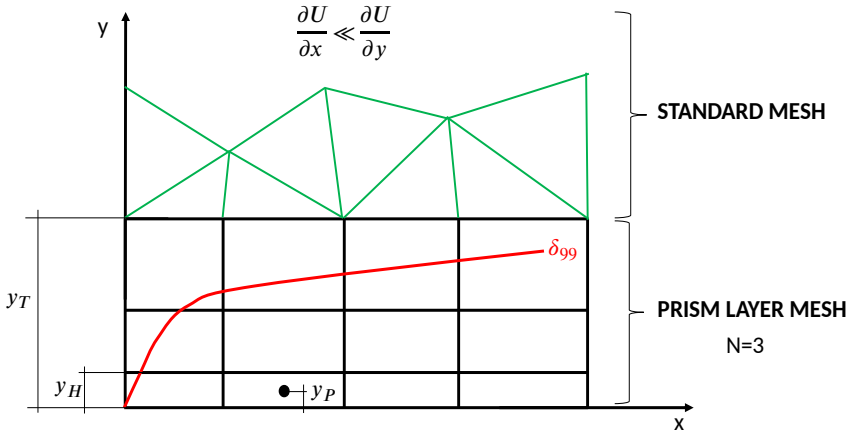

Figure 3.8: Schematic representation of a prism layer mesh made of $N = 3$ layers, with first layer height y_H, total prism layer height y_T, height of the first cell centroid y_p and boundary layer thickness δ_{99}. A smooth transition between the two meshes (Volume Change ≈ 1) is key for numerical accuracy.

When dealing with numerical methods, the values of the unknows are evaluated in a discrete number of points only. Software like *Star-CCM+* rely on finite-volume space discretization strategies, where variables are generally cell-centred.
The value of the unknow between two nodes it's approximated by a linear interpolation, which is in general a reasonable approach. However, in regions where large gradients of the unknows are expected, if the number of cells is not enough, the reconstruction of the solution might be poor or even wrong where theory already suggests non linear profiles of relevant flow quantities.
This specific situation is present whenever the flow has to interact with a solid surface: due to the viscous forces the information of null velocity at the wall (no-slip condition) is "propagated" backwards by diffusion to the core of the flow, with the consequent formation of a boundary layer.
An unstructured polyhedral mesh doesn't guarantee an uniform cell centroid distance with respect to the wall, and for this reason, when resolving the boundary layer, a prism layer mesh is generally adopted to increase the accuracy.
The prism layer mesh, when properly refined, allows better representation of the variables' gradients in the direction locally perpendicular to the wall, while reducing

the resolution in the direction parallel to the wall thanks to very elongated cells, in view of the small gradients expected in that direction.
The prism layer mesh is generally controlled by three parameters:

1. Number of inflation/prism layers N.

2. Geometric growth rate or stretch factor G, relating the size of one layer with respect to the one below.

3. Height of the first layer y_H

A proper prism layer mesh must resolve entirely the boundary layer, whose thickness δ_{99} and features can differ according to the flow regime (see figure 3.8).

For the present work, it's worth mentioning the turbulent law of the wall, derived empirically and represented by the dimensionless velocity u^+ and the dimensionless coordinate y^+ (see figure 3.9).
Without going too much in details, it is sufficient to recall that the turbulent inner boundary layer can be divided into three main regions:

1. **Viscous sublayer**: it's a very thin layer dominated by viscous forces (laminar). The thickness of this layer could be of the order of ≈µm and it decreases as the Reynolds number of the flow increases.
   The relation between dimensionless quantity u^+ and y^+ is linear:

$$u^+ = y^+ \tag{3.69}$$

2. **Buffer layer**: it is a transition region, in the range $5 < y^+ < 30$, where neither linear and logarithmic profiles approximate well the real velocity distribution measured by experiments or DNS.

3. **Log layer**: it is outer-most region of the inner portion of the boundary layer, typically extended in the range $30 < y^+ < 500$, here both viscous and turbulent effects are relevant. The relation between dimensionless quantities follows a logarithmic law:

$$u^+ = \frac{1}{\kappa} \ln\left(Ey^+\right) \tag{3.70}$$

   Being $\kappa = 0.42$ the Von Karman's constant.

Relations 3.69 and 3.70 are known as *standard wall functions*, but *blended wall functions* have been introduced too in order to cover all the three regions with one

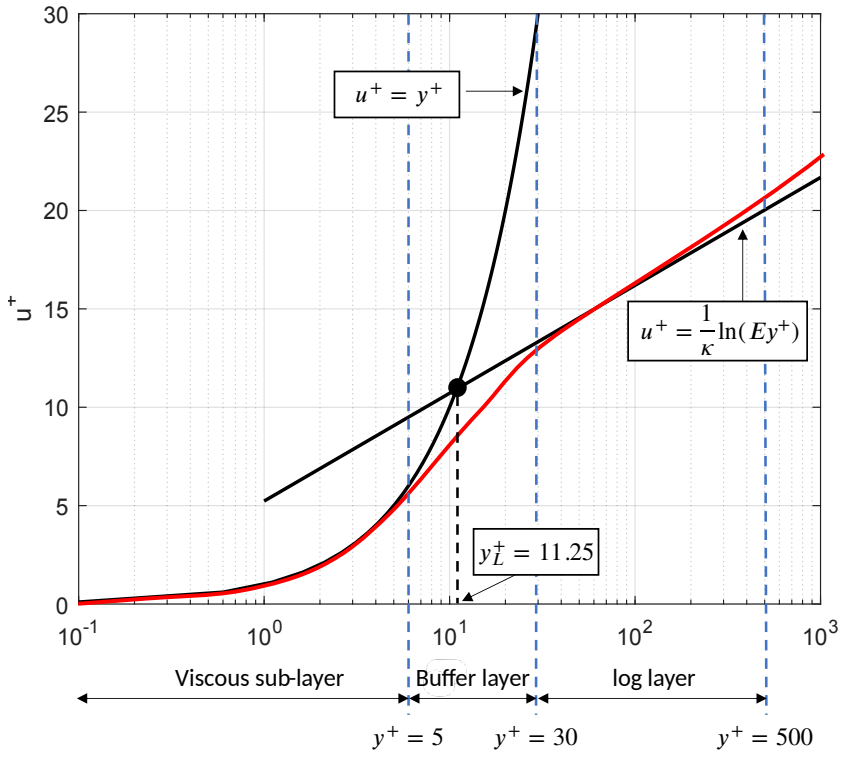

Figure 3.9: Law of the wall

expression only. In *Star-CCM+*, the formulation by Reichardt [19] is used:

$$u^+ = \frac{1}{\kappa}\ln\left(1+\kappa y^+\right) + \frac{1}{\kappa}\ln\left(\frac{E}{\kappa}\right)\left(1 - e^{\left(-\frac{y^+}{y_m^+}\right)} - \frac{y^+}{y_m^+}e^{(-by^+)}\right) \tag{3.71}$$

$$b = \frac{1}{2}\left(y_m^+\frac{\kappa^2}{\ln\left(\frac{E}{\kappa}\right)} + \frac{1}{y_m^+}\right) \tag{3.72}$$

$$y_m^+ = \max\left[3267\left(2.64 - 3.9\kappa\right)E^{0.0125}\right] - 0.987 \tag{3.73}$$

The exploitation or not of such relations depends on the wall treatment that the user decides to apply for his/her simulations. In *Star-CCM+*, three wall treatment are available depending on the mesh refinement (computational cost) that can be afforded to resolve the boundary layer and the selected turbulence closure:

- Low y^+
- High y^+
- All y^+

The *low* y^+ approach is equivalent to *low Reynolds* number approaches, so the viscous sublayer is resolved by the mesh (y^+ order one) and no laws of the wall are exploited. This strategy permits the most accurate prediction of relevant quantities and features such as friction factor/heat transfer coefficient and flow detachment, but becomes very expensive as the Reynolds number increases (since viscous sublayer becomes thinner and thinner).
On the contrary, with a *high* y^+ treatment the first layer of the prism mesh must lay in the log region ($y^+ > 30$): below that threshold flow interesting quantities are approximated by proper wall functions seen above. This strategy allows the lowest computational cost, thanks to the significant savings in near-wall cells number.
In view of the complex geometry of the VV (characterized by different length and velocity scales) in one hand, and the desire to only have a gross estimation of pressure drops and temperature distribution in each control volume on other hand, an *all* y^+ wall treatment has been chosen as a first attempt, following the approach suggested in *Star-CCM+* user's manual.
This third option uses blended wall functions allowing an *high* y^+ treatment for coarser meshes (or regions of the domain where the mesh refinement is lower) and *low* y^+ treatment for finer meshes. With an *all* y^+ treatment, the centroid of the near wall cell should preferably lay in the viscous sublayer (y^+ order one) or in the log layer ($y^+ > 30$), limiting as much as reasonably possible the number of cells in the buffer layer ($1 < y^+ < 30$), where however *Star-CCM+* will perform an interpolation to limit the inaccuracy of the result.

It is important to stress that in any case the CFD code will not exploit wall functions to directly prescribe velocity profile near the wall: the velocity gradient will be always approximated by a linear interpolation, introducing therefore an error if it is not the case in reality (i.e if the near wall cell lays outside the viscous sub-layer). What the CDF code does instead is to guarantee a correct estimation of the wall shear stress despite possible wrong approximation of the velocity gradient, by properly modifying the value of the viscosity, taking into account also the eddy kinematic viscosity ν_t.
It has been already introduced that in the boundary layer dimensionless quantities u^+ and y^+ are related between each other:

$$u^+ = f_u^+(y^+) \tag{3.74}$$

where the function f_u^+ can assume different shapes depending on the specific region of the boundary layer considered. The dimensionless velocity u^+ is defined by normalizing the velocity with the so-called friction velocity u_τ which is determined

starting from the wall shear stress[4] $\overline{\tau_w}$ as:

$$u_\tau = \sqrt{\frac{\overline{\tau_w}}{\rho}} \tag{3.75}$$

Exploiting relations 3.74 and 3.75 it can be derived an expression for the wall shear stress:

$$\overline{\tau_w} = -\frac{\overline{u}\rho u_\tau}{f_u^+(y^+)} \tag{3.76}$$

This expression is general (f_u^+ shape has not been specified yet) and it represents the real wall shear stress.
As already stated however, the CFD code computed the wall shear stress with the velocity gradient, namely with the velocity U_p evaluated at the centroid y_p of the near wall cell as:

$$\overline{\tau_{w,CFD}} = -\rho\nu_w\frac{\overline{u_p}}{y_p} \tag{3.77}$$

To ensure a correct wall shear estimation $\overline{\tau_{w,CFD}} = \overline{\tau_w}$ the effective kinematic viscosity ν_w is therefore modified based on the distance from the wall of each near wall cell:

$$\nu_w = \nu\left(\frac{y^+}{f_u^+(y^+)}\right) \tag{3.78}$$

By replacing f_u^+ with standard wall functions 3.69, 3.70 it is derived the following if-statement which is at the base of any CFD code:

$$\nu_w = \nu + \nu_t = \begin{cases} \nu, & \text{if } y^+ < y_L^+ \\ \frac{u_\tau y_p}{\frac{1}{K}\ln(Ey^+)}, & \text{if } y^+ > y_L^+ \end{cases} \tag{3.79}$$

Where $y_L^+ = 11.25$ is the intercepting point between viscous sub-layer and log-layer wall functions. In case of blended wall functions, the if-statement is of course replaced by an unique expression.
Closing this little parenthesis on how a CFD code operates, it is now possible to discuss how the wall treatment has been practically implemented for the VV analysis.

[4]The friction velocity can be defined starting from the turbulent kinetic energy as $u_\tau = \sqrt{C_\mu^{\frac{1}{2}}k}$. In this case, the dimensionless velocity is generally called u^* in literature. Despite having $u^+ \equiv u^*$ most of the time, this option is preferred because it allows to estimate the dimensionless coordinate y^* with non-iterative methods, reducing the computational effort. Despite that, a detailed discussion about y^+ and y^* falls outside the main interests of this work.

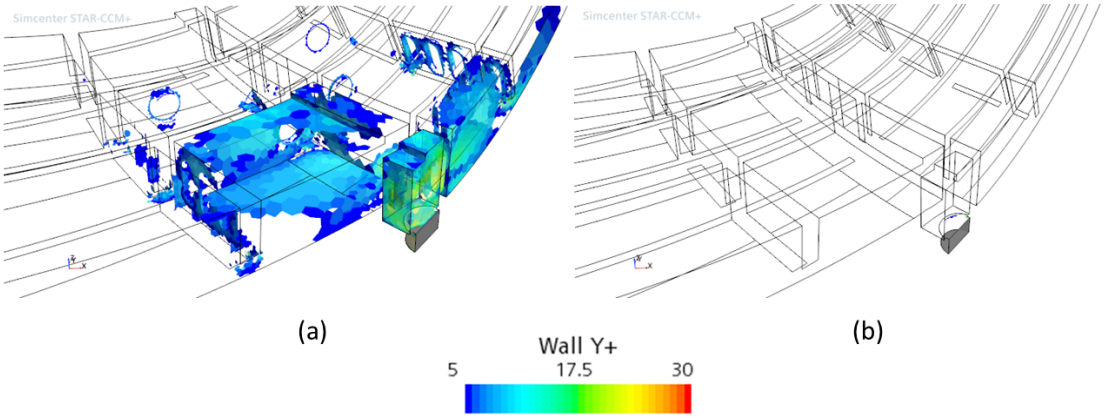

Figure 3.10: Comparison between $y_h = 0.5$ [mm] (a) and $y_h = 0.05$ [mm] (b) wall y^+ distribution. In (b), the number of cells in the buffer layer are drastically reduced. Acceptable values of $y^+ < 5$ and $y^+ > 30$ are out of the selected scale and therefore they do not appear in the plots.

As already anticipated, the prism layers must resolve entirely the boundary layer, namely the region of the flow in which the velocity is lower than 99% of the mean flow velocity. However, a definition of the latter can be only done by performing numerical computations, whose accuracy depends on the mesh refinement in turn. There are available some relations to estimate the parameters of the prism layer mesh, but typically the final setup, which is the best trade-off between target y^+ and volume change between adjacent finite volumes, is obtained in an iterative procedure that starts from an exploring mesh.
According to the law of the wall, the transition between the viscous dominated region and the inertia dominated region (core of the flow) is generally placed at $y^+ = 500$. It is possible to say therefore that in general viscous and log regimes are within $y^+ = 1000$. The total thickness of the prism layer y_T can be then computed from the target y^+ of the first layer and the estimated near wall cell thickness y_H , set to 0.5 [mm] as a first guess:

$$\delta_{99} = y_T = \frac{1000}{y^+_{TARGET}} \cdot y_H \tag{3.80}$$

The result provides a total prism layer thickness $y_T = 15$ [mm], which corresponds to 30% of the polyhedral mesh base size when the coarse mesh (base size $Bs = 50$ [mm]) is considered.
As far as the number of layers is concerned, suggested starting values for *low* y^+ treatment are around 10-15 layers, while for *high* y^+ treatment 2-3 layer may already be enough. A value of $N = 7$ has been chosen as a starting value.

Once prism layer total thickness, near wall thickness and number of layers have been set, the stretch factor can be computed exploiting the geometric progression:

$$y_T = y_H \cdot \frac{1 - G^N}{1 - G}$$

where the stretch factor G can be found numerically. By considering the above mentioned values, a stretch factor of approximately $G \approx 1.5$ is found, which is the default value in *Star-CCM+* when the distribution mode of the prism layer mesher is set to "*Stretch Factor*".
The first simulation with $y_H = 0.5$ [mm] provides a wall y^+ distribution characterized by several cells' centroids located in the buffer layer ($y^+ \approx 15$), in the regions of the computational domain close to the inlet and the outlet, where the maximum of turbulence intensity is expected (see figure 3.10(a)). A well-educated second explorative run therefore is set with a near wall prism layer thickness reduced of one order of magnitude with respect to the previous one, resulting in $y_H = 0.05$ [mm].
The total prism layer thickness is reduced proportionally to $y_T = 2.5$ [mm] and by keeping the number of prism layers unchanged ($N = 7$) the resulting stretch factor, larger than the previous one, remains acceptable, with $G = 1.65$. Since N has not changed, the total number of cells is not remarkably different from the previous run, while the volume change has worsened a bit.
The wall y^+ distribution of this second run at the inlet region is compared to the previous one in figure 3.10, where it is possible to notice that the number of cells in the buffer layer have been almost removed completely.

3.9.2 Modelling Surface Roughness

In addition to what stated above, it is worth mentioning the effect on the boundary layer of the surface roughness.
In fact, it is well known that for the flow of a fluid in turbulent regime, differently from the laminar case, the extremely thin viscous sublayer can be comparable to the surface roughness of the wall, resulting in a significant modification of the flow field.
The functional relation for distributed pressure losses in a circular pipe for turbulent flow, obtained by means of a dimension analysis, suggests that the friction factor f_f is a function of both the Reynolds number and of the relative roughness of the pipe K_s/D, being K_s [µm] the absolute roughness of the pipe:

$$f_f = f_f\left(Re, \frac{K_s}{D}\right)$$

This conclusion has been widely corroborated by experiments and practically summarized in the so-called Moody diagram, where it can be appreciated how,

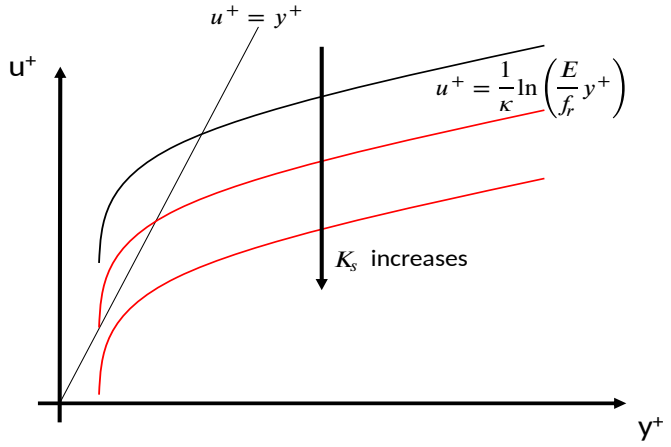

Figure 3.11: Log velocity profile translation as the surface roughness increases.

as the Reynolds number increases, the effect of the surface roughness becomes predominant on the estimation of the friction factor.
From a law of the wall perspective, the different surface roughness has an impact on the relation between the two dimensionless quantities u^+ and y^+: in general this effect is modelled by translating the log layer closer to the wall as the roughness increases, by decreasing the wall function coefficient $E' = E/f_r$ through the roughness function f_r (see figure 3.11).
The latter is a function of the roughness parameter K_s^+, defined as:

$$K_s^+ = \frac{\rho K_s u_\tau}{\mu} \tag{3.81}$$

It can be noticed that its definition is similar to the one of the dimensionless coordinate y^+.
The roughness parameter takes into account the height of the roughness element, while the shape of the roughness is typically described in literature through the coefficient C_s that, from Nikuradse studies, is set to $C_s = 0.5$ for uniform sand grains. More information are available in [20].

According to the value of the roughness parameter, three regions are distinguished:

1. Hydrodynamically smooth, $K_s^+ \leq K_{smooth}^+ = 2.25$.
   In this case the surface roughness is totally contained in the viscous sublayer, and therefore the logarithmic profile is not influenced.
   In this region the roughness function is equal to:

$$f_r = 1 \tag{3.82}$$

2. Transition, $K^+_{smooth} \leq K^+_s \leq K^+_{rough} = 90$.
   Here the roughness function assumes the following form:

$$f_r = e^{\left\{ \frac{1}{\kappa} \ln\left(\frac{K^+_s - K^+_{smooth}}{K^+_{rough} - K^+_{smooth}} \right) + C_s K^+_s \cdot \sin\left(0.4258\left[\ln K^+_s - 0.811\right]\right) \right\}} \tag{3.83}$$

3. Hydrodynamically rough, $K^+_s \geq 90$.
   A saturation is reached and the effect of higher surface roughness becomes smaller and smaller. The roughness function is given as follows:

$$f_r = e^{\left\{ \frac{1}{\kappa} \ln\left(1 + C_s K^+_s\right) \right\}} \tag{3.84}$$

However, with this simple model for small values of E' (and thus high value of surface roughness) it can happen that the logarithmic profile no longer intersects the linear one (see figure 3.11).
This is not an issue if the flow is in the fully rough regime, since the sublayer is irrelevant and pressure losses are related to tangential stresses of inertia-type (pressure drag) rather than of viscous-type, but for moderate value of Reynolds number *Star-CCM+* limits the height of the roughness locally to avoid negative value of u^+.

From a more operational point of view, in the *"Green Book"* it is reported that the new DTT VV design foresees a double-wall stainless-steel (AISI 316L) torus structure with "D" shaped cross section, but there are no information concerning the manufacturing processes involved in the construction of the component, which directly affect the surface roughness.
There are available in literature some reference values for new circular pipes' roughness based on the material [21, 22], but in view of the desired outputs of the TH simulations, for the present work it has been initially assumed that the surfaces of the VV were smooth ($E' = E = 9.0$, $\kappa = 0.42$ as coefficients for the logarithmic profile), with a null surface roughness.
This hypothesis, which is a non-conservative assumption, has been verified once, at the end of November 2022, a provisional document containing technical specification for the VV call for tenders came out. In this document, delivery conditions of semi-finished products have been specified, with a surface finish of $K_s = 6.3$ [µm]. In the same document it was however specified that reported info had not to be intended as official technical specifications.
The updated surface roughness has been therefore included in the model to quantify the sensitivity on the final result with respect to the original smooth approximation. All the conclusions are reported in the results chapter 4, section 4.1.2.

In case of rough walls, for $k-\omega$ models the value of the specific dissipation rate is prescribed in the closest cell to the wall. With an *all* y^+ treatment, it holds:

$$\omega = \gamma \frac{u_\tau^2}{\nu} S_r + (1-\gamma) \frac{u_\tau}{\kappa y \sqrt{C_\mu}} \tag{3.85}$$

where:

$$S_r = \begin{cases} \left(\frac{50}{K_s^+}\right)^2, & \text{if } 5 \leq K_s^+ \leq 25 \\ \frac{100}{K_s^+}, & \text{if } K_s^+ \geq 25 \end{cases} \tag{3.86}$$

and γ is the blending function:

$$\gamma = e^{-\frac{Re_d}{11}}, \; Re_d = \frac{\sqrt{k} d}{\nu} \tag{3.87}$$

which is used to define the velocity scale u_τ with the non-iterative blended wall function:

$$u_\tau = \gamma \frac{\mu u}{\rho y} + (1-\gamma) C_\mu^{\frac{1}{4}} k^{\frac{1}{2}} \tag{3.88}$$

Again, for more details the *Star-CCM+* user's manual is suggested.

3.10 Thermo-physical Properties of Borated Water

The water flowing in the double-shell D-shaped VV has, in addiction to the temperature control objective, to provide a neutronic barrier to the ex-vessel components, like the very delicate, complex and expensive superconducting TF coils while reducing at maximum neutron-induced radioactivity to simplify the decommissioning, waste management and, last but not least, public acceptance phases.
In 2021, Villari et al.[23] carried out an in deep study to assess three-dimensional neutronics, activation and dose rate analyses for the design and licensing of DTT. They considered a 20° sector model including the Central Solenoid (CS), the Toroidal Field (TF) winding pack, the VV made of stainless steel and filled with borated water (0.8 wt%, 95% ^{10}B enriched) and the First Wall (FW), the latter water cooled and provided with a tungsten jacket, as shown below in figure 3.12:

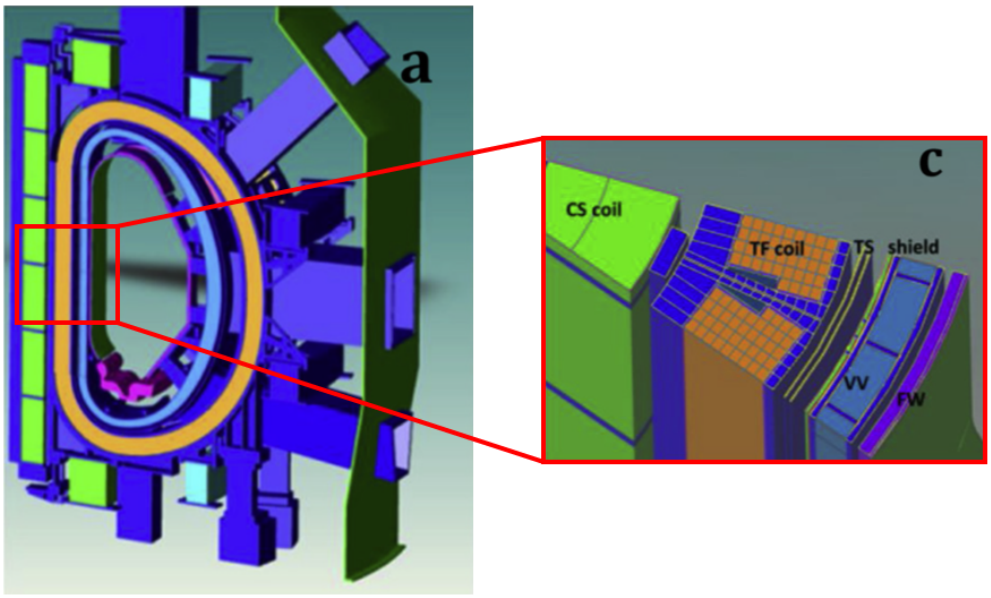

Figure 3.12: MCNP (Monte Carlo N-Particle) 20° domain simulated by Villari et al. with a close-up on the radial distribution of the different components at the inboard leg of the DTT machine. Images are taken from the original paper [23].

Such share of boron in water was considered sufficient in terms of TF thermal load constraints (heat deposition of nuclear type in the superconducting magnets below 1 [mW cm^{-3}][4]) during high-performance operation (maximum $1.5 \cdot 10^{17}$ neutron s^{-1} 2.5 MeV from D-D reactions and $1.5 \cdot 10^{15}$ neutron s^{-1} 14 MeV from D-T reactions) for the outboard side, while for the inboard side it has been concluded that the borated water has to be paired with a neutron/gamma shield to satisfy design

requirements.
More in details, the most effective VV design foresees an IB thickness of 11 [cm] at the equatorial plane (1.5 [cm] front and real shells, 8 [cm] of borated water), coupled with 2.5 [cm] of neutron/gamma shield made of W and B_4C (boron carbide) high density compacted powder (again with boron 95% ^{10}B enriched)[5] for a total of 13.5 [cm], which reduces the nuclear load down to 0.86 [mW cm^{-3}] (1.5 safety factor included) in the first TF turn.
In the latest design, the thickness of the IB leg has been increased to 13 [cm] (10 [cm] of borated water) and, because of volume constraints at the inner side of the machine, the neutron shield attached to the IB rear shell has been removed. As a consequence, the share of boron in water has been re-evaluated recently to work around the missing neutronic protection offered by the latter.

At the time of the present Thesis, there's still a lack of detailed guidelines as far as water chemistry requirements are concerned for fusion applications.
In a work published in March 2022 [24], the available requirements for fission plants were used and investigated as starting point specifically for the DDT vacuum vessel, considering then a mixture of 8000-ppm B borated water (95% enriched in ^{10}B) at 80°C in order to assess its corrosion effect on stainless steel (AISI316L type family) base microstructure as well as welding-induced microstructures[6], in view of the many welded joints foreseen in the VV design.
As already stated, the design requirement during high performance plasma tests is to limit the heat deposition below 1 [mW cm^{-3}] in TF coils while ensuring the integrity of the materials, reducing the so-called stress corrosion cracking (SSC, combined effect of corrosion and constant load).
During one week of testing, the amount of released ions [µg cm^{-2}] from steel samples were measured via ICP-MS (inductive coupled plasma mass spectrometry) whose details are far beyond the scope of the present paragraph. No significant differences were found in terms of Fe, Ni, Cr and Mo releases with respect to the microstructure, but higher Fe and Cr releases have been detected when exposing steel to borated water rather than ultra pure water. This result could be related to the acidic pH of the borated water, but it is important to stress that the corrosion protection of stainless steel relies on the so-called duplex spinel oxide, which creates a passivating protection layer. Being the latter mostly made of chromium, larger release of it can decrease or even nullify the protection against corrosion.

[5]The ^{10}B isotope is characterized by a larger neutron absorption cross section (0.2 barn at 1 MeV) with respect to the ^{11}B isotope. However the ^{10}B content in natural boron is limited to 19.9%.

[6]TIG (tungsten inert gas) and SMAW (shielded metal arc welding) welding strategies have been considered.

However, assessing the passivation mechanism of 316L in boric acid solutions requires longer exposures of metal samples (>1 month) and thus further investigations are needed and planned for the future.
As an hypothesis for the present work therefore, buffered solutions (introduction of a base like LiOH or KOH to neutralize the acid pH of borated water) will not be considered, and the estimation of thermo-physical properties to use as inputs for thermal-fluid dynamics simulations will be restricted to simple aqueous solutions of boric acid.

3.10.1 Solubility of Boric Acid in Water

Boric acid H_3BO_3 is moderately soluble in water and it is characterized by a negative heat of solution. That means the solubility process is endothermic and, according to the Le Chatelier's principle, an increase in temperature will shift the equilibrium condition towards the products, increasing thus boric acid solubility in water:

$$\text{heat} + B(OH)_3 + H_2O \longleftrightarrow B(OH)_4^- + H^+$$

A literature review of boric acid solubility data [25] compares the measured value of boric acid solubility in water with respect to temperature. Recalling that the solubility refers to the maximum quantity of solute that can dissolve in a certain quantity of solvent, it is found that at the target operating temperature of VV borated water (60°C, 333.15 K) the solubility is around 148.1 $[g_{H_3BO_3}\, kg^{-1}_{H_2O}]$.
The borated water for the DTT VV is obtained by adding boric acid H_3BO_3 to ultra pure water, so to reach the desired concentration.
Being the latter higher than conventional values for fission plants' normal operations (reactor's power adjustment) and off-normal/emergency operations (e.g passive safety system to cool the core in case of loss of coolant accident in WWER type reactors), but still not so relevant on an absolute scale, the density of the resulting mixture can be approximated to the one of pure water.
By doing that, it is possible to approximate 1-ppm ≈ 1 $[mg\, L^{-1}]$, obtaining:

$$8000\text{-ppm} \approx 8000\ [mg\, L^{-1}] = 8[g\, L^{-1}] \approx 8\ [g\, L^{-1}_{H_2O}]$$

The obtained concentration refers to mass of pure B over mass of water.
However, as already anticipated before, the borated water is obtained by diluting boric acid H_3BO_3 with ultra pure water. Being the molar mass of boric acid $\overline{M}_{H_3BO_3}$= 61.83 $[g\, mol^{-1}]$ and 1.00784, 15.999 and 10.811 $[g\, mol^{-1}]$ the atomic weight of hydrogen, oxygen and boron respectively, it can be computed that for each gram of H_3BO_3 there are approximately 0.1748 [g] of boron.
It means that the concentration of boric acid $[g\, L^{-1}_{H_2O}]$ needed to get 8000-ppm of B

is defined as:

$$C_{H_3BO_3} = \frac{8\ [g_B\, kg^{-1}_{H_2O}]}{0.1748\ [g_B\, g^{-1}_{H_3BO_3}]} = 45.8\ [g_{H_3BO_3}\, kg^{-1}_{H_2O}] \tag{3.89}$$

which recovers exactly the 4.575 wt% of boric acid used in [24] to prepare the different samples.
The resulting concentration is well below the maximum one, and it roughly corresponds to the solubility in the temperature range between $10 \div 20$°C. Therefore it must be checked that a minimum temperature constraint of $T_{min} = 293.15$ [K] is not violated in the TH results. However, as seen at the beginning of this chapter, the design requirement on minimum temperature constraint (DS2) was set at $T_{min} = 313.15$ [K], which is therefore largely conservative.
For sake of completeness, it must be stressed that the solubility values reported in [25] are evaluated at atmospheric pressure, while the absolute pressure in the VV will be around 4 [bar]: however it must be also recalled that for solids and liquids changes in pressure do not leads to significant changes in solubility. Looking at the Le Chatelier's principle again, it can be noticed that stoichiometric coefficients of reactants and products balance themselves, corroborating the negligible effect of pressure.

3.10.2 Density, Dynamic Viscosity, Specific Heat and Thermal Conductivity of Borated Water

In literature, experimental data measuring the density of aqueous solutions of boric acid on a wide range of temperatures ($298 \div 573$ [K]) and pressures ($100 \div 500$ [bar]) have been provided in [26] for H_3BO_3 concentrations between $3.1 \div 44.4$ [$g\, kg^{-1}$]. Values of density and viscosity for borated water with concentrations of $2.52, 25$ and 45 [$g\, kg^{-1}$] in the temperature window $339 \div 373$ [K] and at atmospheric pressure have been assessed in [27] and values of dynamic viscosity of $2 \div 20$ [$g\, kg^{-1}$] borated water mixtures within $298 \div 423$ [K] and $1 \div 30$ [MPa] are presented in [28].
None of the three available studies actually cover exactly the specific conditions realized in the DTT VV, being the concentration higher than 45 [$g\, kg^{-1}$], the pressure of the coolant around 4 [bar] and the temperature lower than 333 [K] [5]. To cover the lack of available data, in 2018 an experimental study was conducted to asses thermo-physical properties of boric acid solutions [29], even if the final goal was to cover a range of parameters specific for WWER possible accidents.
The density of the solution have been assessed experimentally by a pycnometric method considering a temperature range between $298 \div 403$ [K] (± 1 [K] of accuracy), a concentration of boric acid between $2.5 \div 450$ [$g\, kg^{-1}$] and values of pressures coherent with water-water energetic reactor (WWER) off-normal condition (LOCA, $0.1 \div 0.4$ [MPa]) down to the atmospheric pressure.

To assess the kinematic viscosity, the capillary viscometry method was exploited instead. From the experimental data, correlations for both density and kinematic viscosity have been then obtained.

Starting from the density of the solution, the following relation was found:

$$\rho_{mix}(T_{mix}, C_{\mathrm{H_3BO_3}}) = A + B \cdot C_{\mathrm{H_3BO_3}} \tag{3.90}$$

where $A = 1141 - 0.48 \cdot T_{mix}$ and $B = 39217 \cdot T_{mix}^{-0.843}$ while $C_{\mathrm{H_3BO_3}}$ [$\mathrm{kg\,kg^{-1}}$], T_{mix} [K] and ρ_{mix} [$\mathrm{kg\,m^{-3}}$] are instead the concentration, the temperature and the density respectively of the solution. The maximum mismatch between the values computed with correlation 3.90 and the experimental ones does not exceed 2%.

Concerning the kinematic viscosity ν_{mix} [$\mathrm{m^2\,s^{-1}}$] it was found instead:

$$\nu_{mix}\left(T_{mix}, C_{\mathrm{H_3BO_3}}\right) = \nu_{H_2O}\left(T_{mix}\right) + C\left(C_{\mathrm{H_3BO_3}}\right)^D \tag{3.91}$$

where $\nu_{H_2O}\left(T_{mix}\right)$ is the kinematic viscosity of pure water, defined as:

$$\nu_{H_2O}\left(T_{mix}\right) = \frac{1.78 \cdot 10^{-6}}{1 + 3.37 \cdot 10^{-2} \cdot (T_{mix} - 273.15) + 2.21 \cdot 10^{-4} \cdot (T_{mix} - 273.15)^{-2}}$$

and coefficients C and D are defined as:

$$C = 1.86 \cdot 10^{-7} + 1.08 \cdot 10^{-5} \cdot e^{(-0.119 \cdot (T_{mix} - 273.15))}$$
$$D = 1.224 - 2.83 \cdot 10^{-2} \cdot (T_{mix} - 273.15) + 2.19 \cdot 10^{-4} \cdot (T_{mix} - 273.15)^2$$

In this case the discrepancy between approximated values obtained with the correlation above and experimental data does not exceed 5.5%.
Once density of the solution and kinematic viscosity are known, the dynamic viscosity of the solution can be easily defined as:

$$\mu = \nu \cdot \rho$$

However, being the dynamic viscosity derived indirectly from both density and kinematic viscosity, the error propagation must be taken into account. The most probable error is therefore defined as:

$$\delta\mu = \sqrt{\left(\left.\frac{\partial\mu}{\partial\rho}\right|_{\bar{\nu}} \cdot \delta\rho\right)^2 + \left(\left.\frac{\partial\mu}{\partial\nu}\right|_{\bar{\rho}} \cdot \delta\nu\right)^2} \tag{3.92}$$

with $\delta\rho = \pm 2\%$ and $\delta\nu = \pm 5\%$ the accuracy of the density and of the kinematic viscosity respectively. It reaches a maximum value of $\approx 4.4 \cdot 10^{-5}$, but it must be

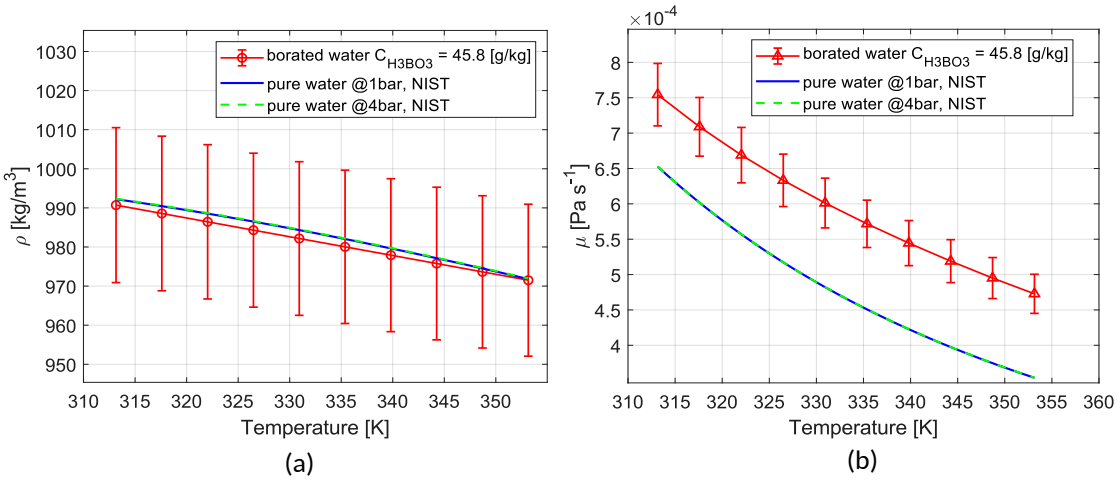

Figure 3.13: Borated water density (a) and dynamic viscosity (b) evolution as a function of temperature at the target concentration of DTT VV. Correlations from Morozov et al.

stressed that this uncertainty only takes into account the deviation with respect to experimental data, without considering the accuracy of pycnometric and capillary viscometry methods.
As shown in figure 3.13, in view of a deviation between mean values always greater than 13%, it could make sense to consider the effect of boron for the dynamic viscosity of the mixture while for the density the effect is completely negligible (which justify a posteriori the approximation of considering 1ppm $\approx$ 1 mg L^{-1}).

From a purely thermal point of view, specific heat c [$\mathrm{J\,kg^{-1}\,K^{-1}}$] and thermal conductivity λ [$\mathrm{W\,m^{-1}\,K^{-1}}$] have to be assessed as well, investigating their dependence, if any, with respect to temperature, pressure and boron concentration.
Regarding the first parameter, in [30] the isobaric heat capacity of boric acid solutions has been measured for a concentration of 0.648 [$\mathrm{mol\,kg^{-1}}$] (which corresponds to 40.1 [$\mathrm{g\,kg^{-1}}$]) for a wide range of temperatures (303.15 $\div$ 394.15 [K]) and pressures (0.1-5.11 [MPa]).
The resulting interpolation of data leads to the following correlation:

$$c = (a_1 + a_2 \cdot T + a_3 \cdot P) \cdot 1000 \tag{3.93}$$

where the interpolation coefficients are respectively equal to:

$$a_1 = 3.651 \ [\mathrm{J\,g^{-1}\,K^{-1}}]$$
$$a_2 = 1.116 \cdot 10^{-3} \ [\mathrm{J\,g^{-1}\,K^{-2}}]$$
$$a_3 = -7.788 \cdot 10^{-3} \ [\mathrm{J\,g^{-1}\,K^{-1}\,MPa^{-1}}]$$

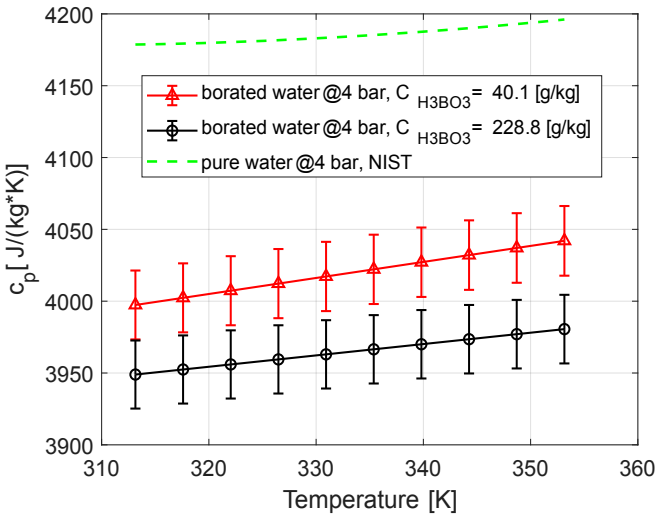

Figure 3.14: Comparison of the evolution of specific heat at constant pressure with respect to temperature for borated water solutions and pure water. Correlations from He et al.

With a relative deviation always less than 0.6% with respect to measured data.
As reported in the conclusion of the study and in figure 3.14, the dependence of the specific heat with respect to the boron concentration is limited, with a maximum deviation of 1.53% in the range of temperature and pressures explored, when considering a concentration deviation of 471% (passing from 40.1 [g kg^{-1}] to 228.8 [g kg^{-1}]).
Keeping in mind the computed pressure drops in the regular sector, the effect of pressure results to be negligible as well.
Noted that the concentration of boric acid in borated water has small effects on the thermal capacity, the investigated concentration of 40.1 [g kg^{-1}] can be confused with the target concentration of 45.8 [g kg^{-1}].
However, it can be appreciated that from pure water to borated water the difference in the specific heat is not negligible, and it increases as the temperature of the solution increases. More specifically, when the design operating thermodynamic conditions foreseen for VV are considered, the relative difference between the specific heats is approximately 4%: therefore it makes sense to consider it in the thermal-hydraulic simulations.

To conclude, thermal conductivity of boric acid-water solutions has been investigated experimentally in [31], exploiting transient hot wire source method for five different boric acid loadings, specifically 0.1,0.3,0.5,1 and 3 wt%, in a temperature range between 298.15 and 328.15 [K].

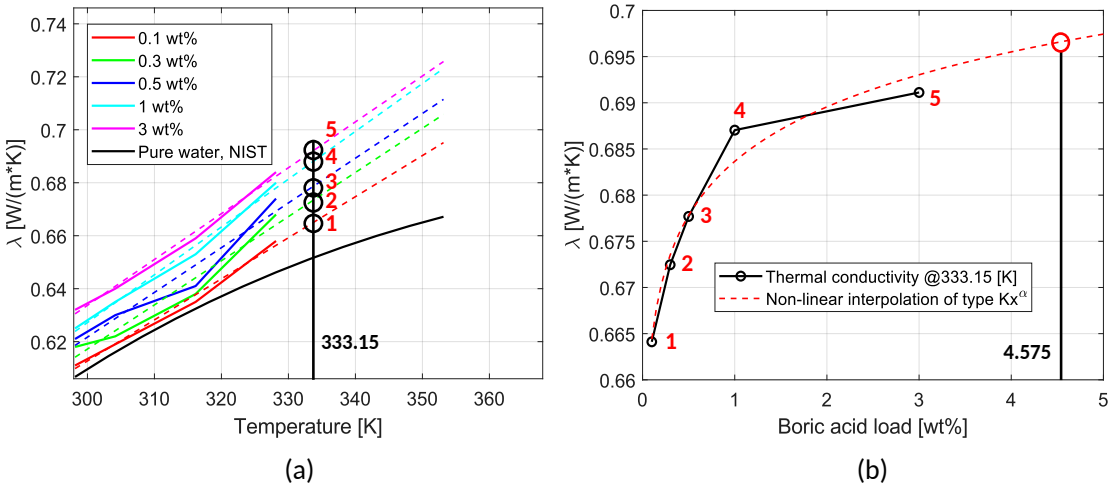

Figure 3.15: (a) Linear interpolation of thermal conductivity with respect to temperature. Data are available up to 328.15 [K] only. The highest standard error of the least square estimation is found for 0.5 wt% data: $\delta\lambda = \pm 0.0068$ [$\mathrm{W\,m^{-1}\,K^{-1}}$]. (b) The five extrapolated data at $T = 333.15$ [K] are interpolated in turn with the non-linear relation $\lambda = K\,(wt\%)^{\alpha}$, with $K = e^{-0.3803}$ and $\alpha = 0.0124$ as interpolating coefficients. The thermal conductivity at the target boric acid concentration is finally extrapolated.

It must be stressed out that the explored ranges do not cover DTT VV operating conditions, and therefore two extrapolations from available data are needed.
As stated by the author of the study, the dependence of thermal conductivity could be well approximated by a linear relationship with respect to temperature while, as the concentration of boric acid increases, the thermal conductivity reaches a sort of saturating value.
If available data are linearly interpolated, the values of thermal conductivity at target temperature of $T = 333.15$ [K] could be extrapolated (see figure 3.15(a)).
Then the five points (corresponding to different concentrations) can be interpolated in turn with a power relation to extrapolate the thermal conductivity at the desired boric acid concentration, finding the indicative value of $\lambda\,(333.15\ [\mathrm{K}],\ 4.575\ \mathrm{wt\%}) = 0.6967$ [$\mathrm{W\,m^{-1}\,K^{-1}}$] (see figure 3.15(b)).
The standard error of the least square estimation for the second interpolation only, can be computed as:

$$\delta\lambda = \pm\sqrt{\frac{1}{N-2}\cdot\sum_i\left[\lambda_i - (K\cdot wt_i\%^{\alpha})\right]^2} = \pm 0.0023\ [\mathrm{W\,m^{-1}\,K^{-1}}] \qquad (3.94)$$

where N represents the number of data samples (five in this case) and λ_i the linearly extrapolated thermal conductivity.
By considering only the mean value of 0.6967 [$\mathrm{W\,m^{-1}\,K^{-1}}$], the deviation with respect to the pure water thermal conductivity (@1 [bar], NIST) at the same temperature is around +6.6%.
The computed thermal conductivity enhancement is in line with the results found in [31], being the latter larger and larger as the temperature increases (5.39% at 323.15 [K]).
In light of the obtained results, it makes sense to consider the effect of boron dissolved in water as far as thermal properties are concerned.
To conclude, it must be pointed out that the effect of pressure has been neglected for the evaluation of the thermal conductivity, starting from the observed weak dependence in the case of pure water.

To summarize, material properties exploited in preliminary TH analysis by the NEMO group reported in table 2.1 have been updated to take into account, when reasonable, the effect of dissolved boron as shown in table 3.2 below:

Property	**Value**
Density [$\mathrm{kg\,m^{-3}}$]	983.3
Dynamic viscosity [Pa s]	$5.8613 \cdot 10^{-4}$
Specific heat [$\mathrm{J\,kg^{-1}\,K^{-1}}$]	4019.68
Thermal conductivity [$\mathrm{W\,m^{-1}\,K^{-1}}$]	0.6967
Thermal expansion coefficient [$\mathrm{K^{-1}}$]	$5.82 \cdot 10^{-4}$
Turbulent Prandtl number	0.9

Table 3.2: Thermo-physical properties of borated water exploited for the material characterization in new TH simulations.

Details regarding the choice of the Turbulent Prandtl number are available in appendix A.

Chapter 4

Thermal-Hydraulic Results and Discussion

"The purpose of computing is insight, not numbers"
Richard Hamming, 1962

4.1 Regular CV1

In this section, the most relevant conclusions found for the regular control volume CV1 will be presented.
The first regular CV has been selected as reference domain to tune and adjust all the simulation choices, including the evaluation of results' sensitivity to different simulation settings.
Despite non negligible (a priori) peculiarities which distinguish the different CVs, it can be stated that overall velocity and length scales are similar in each CV and for that reason, all the conclusions found specifically for CV1 will be extended to all the other geometries without the need to start every time from scratch.
In the following sections, mesh independence study together with sensitivity assessment with respect to prism layer setup, inlet BC and surface roughness will be presented.
On top of that, results from unsteady simulation will be shown as well to justify numerical oscillations in simulation reports found for increasing level of mesh refinement.

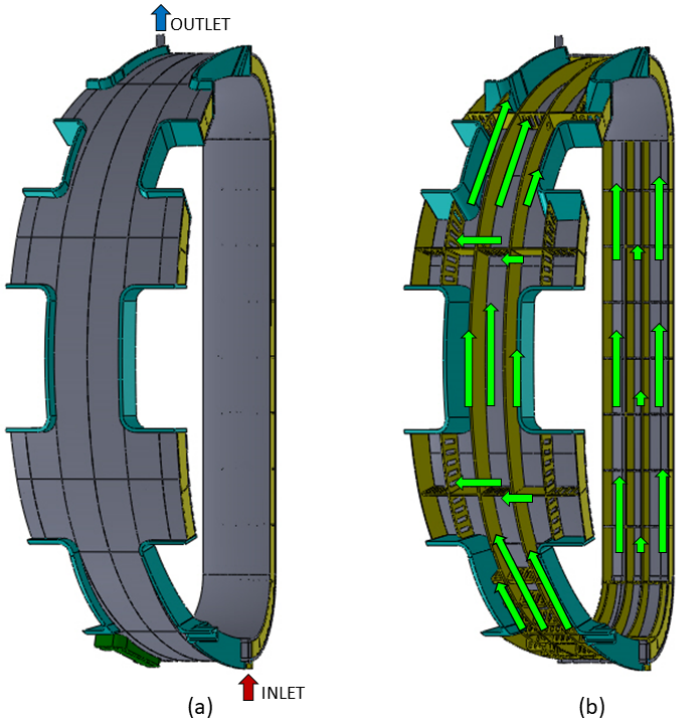

Figure 4.1: (a) Extrapolated CAD of CV1-type R. (b) Qualitative schematization of the mass flow distribution inside OB and IB channels. Length of green arrows is proportional to the mass flow magnitude.

4.1.1 CV1 Geometry

The first regular control volume, highlighted with the red color in figure 2.5, is the most recurring geometry inside the VV. It appears four times, three of them with the inlet located on the right-end side (hydraulic sectors $i1$, $i3$ and $i7$) and only once with the mirrored configuration (hydraulic sector $i9$).
The extrapolated geometry together with insights on poloidal and toroidal ribs distribution is presented in figure 4.1.
As most of all the CVs, following what has been achieved by previous TH simualtions, three parallel channels can be identified both on outboard an inboard legs. The former are hydraulically connected also in the core of the geometry thanks to pipes for toroidal flow while the latter are independent everywhere but in inlet and outlet sections.
In section 4.1.5, a detailed description on how to compute mass flow rate distribution in each channel will be presented together with a method to correctly detect and quantitative assess reverse flow or stagnation.

4.1.2 Sensitivity to Prism Layer Mesh Refinement, Surface Roughness and Inlet BC Specification.

In section 3.9 the importance of the prism layer mesh for the correct evaluation of velocity and temperature gradients near the wall has been introduced.
However, despite indicative constraints on y^+ and suggested starting values for the number of prism layers N and the total thickness y_T, there are still infinite combinations that can be chosen among the acceptable ranges.
For that reason, a good practice in CFD is to perform a mesh-refinement study focusing solely on prism layer parameters exploration, to assess the sensitivity on final results of almost arbitrary choices (again, general rules of thumb adopted in section 3.9 only provide constraints on acceptable ranges for prism layer parameters, not unique values).

In the following table 4.1, the influence of prism layer parameters variation on the pressure drop is shown for some relevant cases, in comparison to the reference case adopted for medium mesh (Base Size $Bs = 15$ [mm], see section 4.1.4 for details.):

Mesh	**Target y^+**	**y_H [mm]**	**N**	**G**	**Δp [Pa] (% dev. w.r.t Ref. Δp)**
Ref.	all y^+	0.05	10	1.33	2734.8 (0%)
1	all y^+	0.05	7	1.65	2705.5 (-1.1%)
2	low y^+	0.01	15	1.34	2745.5 ($+0.4$%)
3	high y^+	1	2	1.5	2525.7 (-7.6%)

Table 4.1: Prism layer mesh refinement study for medium mesh $Bs = 15$ [mm]. In mesh number three, pure *high* y^+ approach has been investigated revealing a significant deviation with respect to reference data. In addition, residuals for this attempt are significantly larger and therefore an *high* y^+ is not recommended.

In section 3.7 the boundary conditions for the TH model has been discussed.
As a modelling choice, it has been decided to set the inlet BC as "*mass flow inlet*" (MFI) prescribing thus uniquely the total mass flow rate, assuming therefore uniform velocity and $k - \omega$ profiles.
In section 3.8 instead, pure hydraulic simulations have been carried out on CV1 inlet (axisymmetric 2D domain) to compute fully developed velocity and $k - \omega$ profiles.
Moreover, in view of initially missing information on surface roughness specification, all the solid interfaces has been considered ideally smooth. Then, as already discussed in section 3.9.2, indications of roughness constraints for semi-finished surfaces came out in November and therefore an investigation of surface roughness effect on final results became mandatory.

In table 4.2, again for the medium mesh ($Bs = 15$ [mm]), the resulting pressure drop in case of FDI (fully developed inlet) and FDI+Rough (fully developed inlet plus rough surfaces) is compared with the reference MFI case.

Case	**Δp [Pa] (% dev. w.r.t Ref. Δp)**
FDI	2670.4 (−2.4%)
FDI+Rough	2675.7 (−2.2%)

Table 4.2: Dependence of the evaluated pressure drop on inlet boundary conditions and surface roughness characterization. Medium mesh $Bs = 15$ [mm].

In conclusion, keeping in mind the maximum percentage deviations with respect to the reference case shown in the two tables above (4.1, 4.2) and the pressure drop difference between different CVs (see next sections), it can be stated that, for the present work, the sensitivity with respect to prism layer refinement, inlet turbulent specification and surface characterization can be considered negligible except for the *high* y^+ treatment, that should be avoided.
It is however important to stress that FDI condition is by far more realistic than MFI because, at the inlet pipe of each CV, the velocity profile resulting from the complete VV P&ID cooling system will be in any case much more similar to FDI solution rather than an uniform and unperturbed one.
The reader may rebut saying that once axial velocity, k and ω fully developed profiles are known they can be just imposed to all the other CVs without the need to re-do the simulation for each inlet, being the initial prescribed mass flow rate and the pipe's diameter identical for each CV.
This is true in theory, but not so efficient in practice: each CV is extracted from the complete VV CAD and therefore it preserves the global VV reference system (inlet axis oriented vertically along z).
Imposing the 2D axisymmetric profiles implies a specific roto-translation for each inlet (remember that in *Star-CCM+* the user is obliged to exploit the x axis as symmetry axis for axisymmetric simulations).
The effort of correctly implementing the roto-traslation twelve times is not justified by what the simulation returns back, and a MFI condition remains the most effective, but also conservative, solution for the specific problem under consideration.
For what regards the surface characterization instead, the introduction of surface roughness is almost effortless and, even if captured differences are totally negligible ($\approx$ 5 [Pa] between FDI/FDI+Rough cases), it can be implemented for all the other CVs. Also the $\approx$ 65 [Pa] difference detected between MFI and FDI will be contained in the uncertainty introduced by unsteady simulations, as shown in the next section.

4.1.3 Unsteady Simulations

While developing the mesh independence study (see next section 4.1.4), it was noticed that as the refinement of the computational mesh increased, also the fluctuations of simulation reports (pressure drop, total mass flow rate in IB and OB legs...) where increasing as well.
More precisely, for the finest mesh ($Bs = 5$ [mm]) it was almost impossible to obtain a flat steady-state as for previous meshes.
Even if such deviations (of purely numerical nature) were actually of modest size ($\approx \pm 2.4\%$) and somehow expected due to the increasing numerical complexity, it has been decided to further investigate the problem with an unsteady approach, to assess if those fluctuations could be actually translated into physical ones.

An implicit solver, safer from the stability point of view, was used to march in time with a first order temporal discretization. A constant CFL of 50 was used for the 20 inner iterations of each time step.
Three time steps have been explored ($\Delta t = 0.001$,0.01,0.1 [s]) when simulating a physical time of at least 1500 [s].
The choice of the considered time steps derives indirectly from numerical and physical considerations: it is known that for a pure advection problem for instance, an explicit time marching approach coupled with an upwind difference scheme is stable if the following relation is satisfied:

$$c_o = \left| u \frac{\Delta t}{\Delta x} \right| \leq 1 \tag{4.1}$$

Where c_o is the Courant number.
This condition, when a base size of 5 [mm] is considered, provides a time step of:

$$\Delta t \leq \begin{cases} 0.5 \text{ [s]} & \text{if } u = 0.01 \text{ [m s}^{-1}\text{]} \\ 0.005 \text{ [s]} & \text{if } u = 1 \text{ [m s}^{-1}\text{]} \end{cases} \tag{4.2}$$

when average core and inlet velocities are considered respectively.
This is trivial: being $\Delta x/u$ the convective time, a time step smaller than that is needed to capture the transport by advection of a certain quantity between adjacent nodes of the computational grid.
Higher it is the velocity flow, smaller will be the convective time and thus the needed time step to capture the physics.
On the other hand, when a pure diffusive problem is considered instead, the second derivative will tend to smooth everything out reducing the unpredictability of the phenomenon. From an hydraulic point of view it is found that for numerical stability:

$$\mu \frac{\Delta t}{\Delta x^2} < \frac{1}{2} \tag{4.3}$$

from which the condition for the time step is derived:

$$\Delta t < 12 \text{ [s]} \tag{4.4}$$

From a thermal point of view instead, the dynamic viscosity is replaced by the thermal diffusivity:

$$\Gamma \frac{\Delta t}{\Delta x^2} < \frac{1}{2} \tag{4.5}$$

from which:

$$\Delta t < 70 \text{ [s]} \tag{4.6}$$

As already introduced at the beginning of chapter 3, Navier-Stokes equations are actually of advective-diffusion type.
Moreover, by employing an implicit solver coupled with a central difference scheme the stability problem is solved as far as pure advection is concerned.
Purely numerical considerations are therefore not sufficient, since the choice of the time step has also a strict relation to the physics of the problem: if relevant quantities such as velocity and pressure vary in the domain faster than what the implicit solver is able to capture, then the transient condition is not correctly reconstructed.
From the previous considerations, it has been decided therefore to put a limit on the largest time step of $\Delta t \leq 0.1$ [s], being the conditions found for pure diffusive problems too soft, and to check the goodness of the solution through a mesh independence study.

As far as the total simulated physical time is concerned, it roughly corresponds to twice the "*time of flight*" which can be estimated knowing the fluid's volume and the volumetric mass flow rate as:

$$t_f = \frac{\iiint_{fv} 1 \text{ dV}}{\dot{m}/\rho} = \frac{0.697 \text{ [m}^3\text{]}}{1.11 \text{ [kg s}^{-1}\text{]} \text{ / } 983.33 \text{ [kg m}^{-3}\text{]}} \approx 620 \text{ [s]} \tag{4.7}$$

This is done to obtain (or to try at least) a full replacement of water inside the control volume for overall flow stabilization.

From transient simulations it turns out that, after approximately the time of flight, the solution reaches a *quasi* steady-state where, as for the steady simulations, relevant reports such as pressure drop and IB/OB mass flow rates oscillate around defined average values.
Differently from the steady-state though, this time captured fluctuations are physical and non purely numerical: for the finest mesh inboard and outboard mass flow rates oscillates with a period of $T \approx 3$ [s], with a maximum amplitude of the oscillation constrained in $\pm 4.4\%$ of the average value. In absolute terms, it

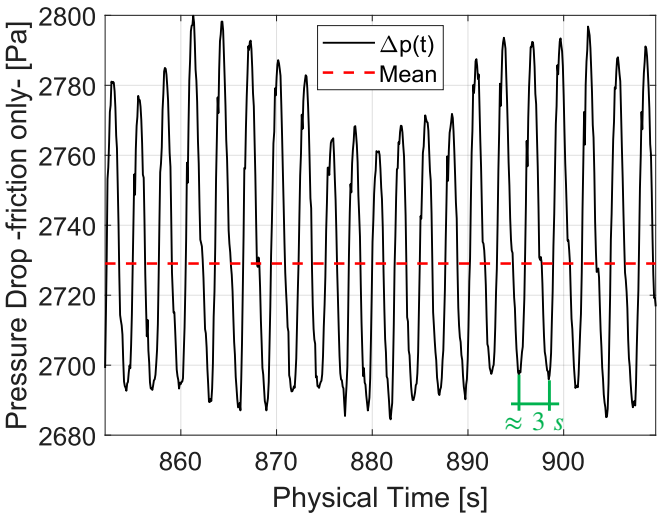

Figure 4.2: Visualization of the pressure drop report, fine mesh, unsteady simulation ($\Delta t = 0.001$ [s]), 60 [s] time interval after reaching the quasi steady-state condition.

corresponds to an uncertainty of ± 20 [g s^{-1}].
Coherently, also the pressure drop shares the same period, with maximum deviation of $\pm 4.2\%$ around the mean value (1.8% larger with respect to the steady-state). Again, in absolute terms, the uncertainty on the pressure drop is limited to ± 115 [Pa] (see figure 4.2).
For the medium mesh instead, reports fluctuations are dumped also with the unsteady solver and remain comparable to steady-state results, no matter the exploited time step.

To summarize, the most relevant conclusions are:

1. The unsteady simulation with the finest mesh reveals that reports' fluctuations are physical and the amplitude of the oscillations is larger than the numerical one found with steady-state solver. For the medium mesh instead, a steady-state is reached also with the unsteady solver.

2. The deviations between average values found with steady and unsteady approaches is of the order of 1.2% if the comparison is done for the medium mesh and of 0.16% with the finest mesh.

3. For the finest mesh, the pressure drop oscillates with a period of $T \approx 3$ [s] and an absolute maximum amplitude of 115 [Pa] around the mean value. Inboard and outboard mass flow rates share the same period, with an absolute amplitude limited to 20 [g s^{-1}] around the mean value.

4. A time step of $\Delta t = 0.1$ [s] is already sufficient to correctly capture reports' fluctuations in view of their physical oscillating frequency.

5. With the unsteady approach, the mesh fine is able to correctly converge without specific variables' initialization. The steady solver on the contrary requires solution on coarser meshes as a starting point and it is much more susceptible to CFL number higher than the default one.

To conclude, even if the exploitation of a steady solver for an unsteady problem is not correct a priori (it can be compared to using a not suitable time step in an unsteady simulation) as long as the steady simulation is able to capture a steady-state where reports' deviations are constrained within 1.2% with respect to the mean value found by transient simulations, it represents the fastest and cheapest way to characterize the control volumes in a reliable way.

4.1.4 Mesh Independence Study, Thermal-Hydraulic Results and Computational Cost Scalings

In this section, all the reasonings done above are summarized and compared in a grid independence study. The latter is needed to confirm the convergence of the numerical solution.
From theory, a numerical method converges if the numerical solution, which is the solution of the discretized equations, tends to the exact solution as the grid spacing is reduced ($\Delta h \longrightarrow 0$).
The grid independence study is therefore a fundamental ingredient of the *verification* process, which basically answer the question: "*are the equations chosen for the CFD model solved correctly*?".
From a practical point of view, convergence studies are needed to demonstrate that the numerical error of the solution is bounded and that, for finer and finer meshes, the influence of the number of nodes on final results becomes progressively less relevant (up to the condition where approximation errors due to finite machine precision prevail).

For the present work, six meshes have been investigated during the grid independence study. All the meshes are characterized by the same thickness of the first layer $y_H = 0.05$ [mm] (because of wall y^+ constraints), while the number of prism layers is tuned to guarantee the smoothest volume change to the polyhedral mesh. On the same line, for very coarse mesh a lower surface growth rate (SGR) is needed to obtain decent mesh transitions.
The most relevant parameters of the six meshes are presented in table 4.3.
As can be appreciated in figure 4.3 the coarser mesh requires a larger prism layer total thickness and a lower number of prisms. Moreover, the prism's elongation

Mesh	Base Size Bs [mm]	MSS (%Bs)	SGR	N	y_T [mm]	Cells
Very Coarse	100	7	*slow*	7	5	$679k$
Coarse	50	10	*slow*	7	2.5	$1.8m$
Quasi-Medium	25	10	*default*	10	2.5	$3.9m$
Medium	15	10	*default*	10	2.5	$6.5m$
Quasi-Fine	7.5	10	*default*	10	2.5	$12.3m$
Fine	5	10	*default*	10	2.5	$21.8m$

Table 4.3: Most relevant parameters of the six meshes employed for the grid independence study. MSS stands for *Minimum Surface Size* while SGR stands for *Surface Growth Rate*.

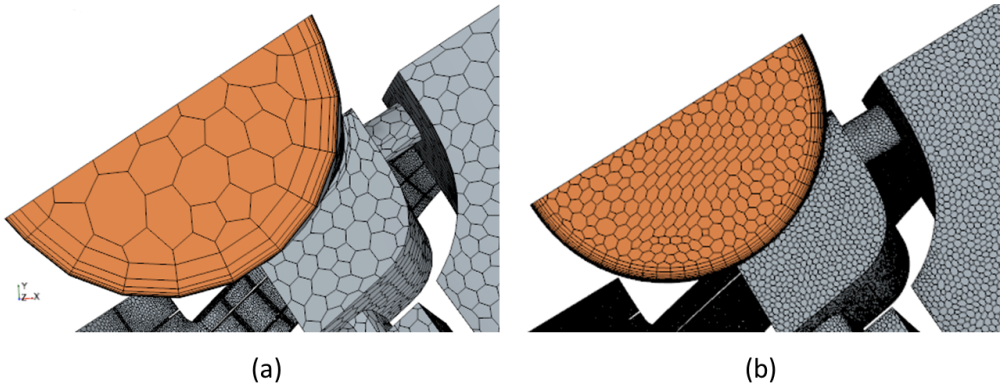

Figure 4.3: Close-up of the outlet region for Very Coarse (a) and Fine (b) meshes.

leads to a quite poor approximation of the outlet's diameter.
Before discussing the grid independence results, it is important to stress that for finer meshes (medium or above) some geometric peculiarities of the extracted and then simulated fluid volume leads to severe unphysical temperature values due to numerical instabilities.
To overcome that, local volumetric/surface mesh refinements by means of spheres were employed to guarantee stability in the regions of the geometry characterized by sharp edges, real nightmares of CAE engineers, as shown in figure 4.4.
With the mesh refinement, a custom base size of $Bs' = 25\%Bs$ together with a custom number of prism layers $N' = 15$ was imposed in the regions of the fluid volume intercepted by the different spheres.
With a Java Macro, this strategy has been extended a priori to all the other CVs (since similar/same geometric peculiarities were found as well) but also to coarser meshes, where despite little local mesh worsening (higher volume changes) the convergence was not affected.

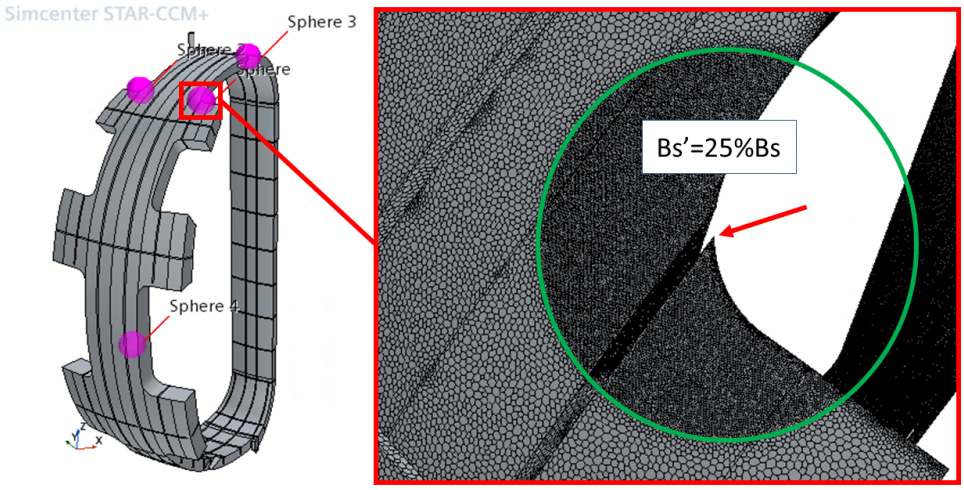

Figure 4.4: Volumetric/Surface mesh refinement by means of spheres (in purple) centered on the the sharp edges of the fluid geometry (or in general where instabilities occur) with a close-up on the resulting refined mesh.

All things considered, the resulting convergence study is presented in figure 4.5 as far as pressure drop, IB/OB mass flow rates, outlet/min/max temperatures and continuity verification are concerned.
All the relevant results (coming from the unsteady simulation on the finest mesh which represents the best available solution) of CV1 are summarized in table 4.4, while in figure 4.6 scalar scenes of pressure and temperature distribution are presented.

General Info	
CV	1
CV type	Regular
Sectors	S1,4,5,12,13,17,18
Hydraulic Sectors	i1,3,7,9
Inlet	R/L
Fluid Volume [m^3]	0.697
Outer Wall Surface [m^2]	5.56

Results	
Δp **[Pa]**	2732 ± 115
T_{out} **[K]**	333.06
T_{max} **[K]**	333.15
T_{min} **[K]**	331.83
$\dot{m}_{OB}$ **[g s^{-1}]**	620 ± 20
$\dot{m}_{IB}$ **[g s^{-1}]**	490±20

Table 4.4: Relevant geometric and simulation info for CV1. Results are taken from the unsteady fine simulation.

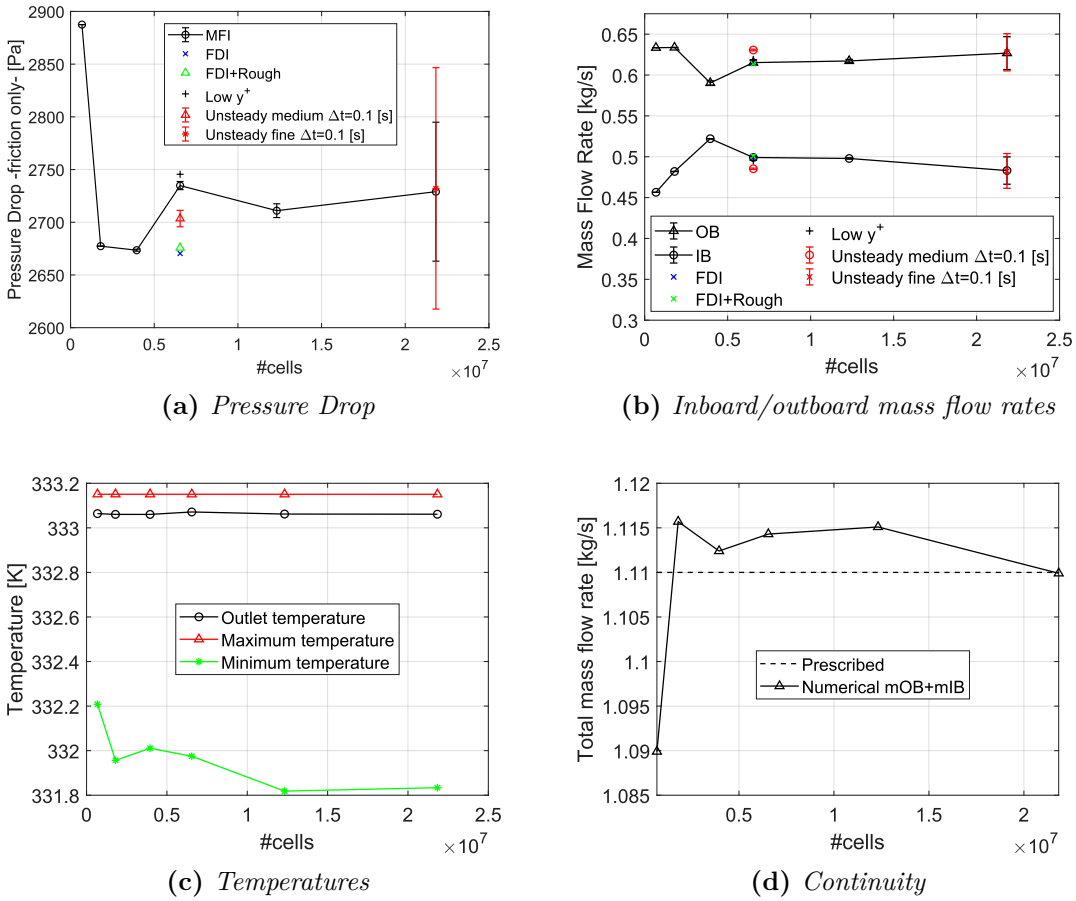

(a) *Pressure Drop* **(b)** *Inboard/outboard mass flow rates*

(c) *Temperatures* **(d)** *Continuity*

Figure 4.5: Mesh independence study for pressure, mass flow rates and temperature carried on six the meshes presented in table 4.3. It can be noticed how the effect of turbulence inlet specification and surface roughness is negligible with respect to physical fluctuations captured by unsteady fine simulation.

As can be seen from the reported results, regarding CV1 no criticalities in terms of pressure drop and min/max temperature were found.
In comparison to the previous TH simulations performed in 2021 it can be summarized that:

- Coherently to what concluded in 2021, pressure drops are heavily concentrated at inlet and outlet regions, where fluid's velocity is almost two orders of magnitude larger than fluid velocity in the core of the domain.
- Differently from the previous design of the regular sector, pressure drops result to be larger with the newest design. This aspect can be explained by looking

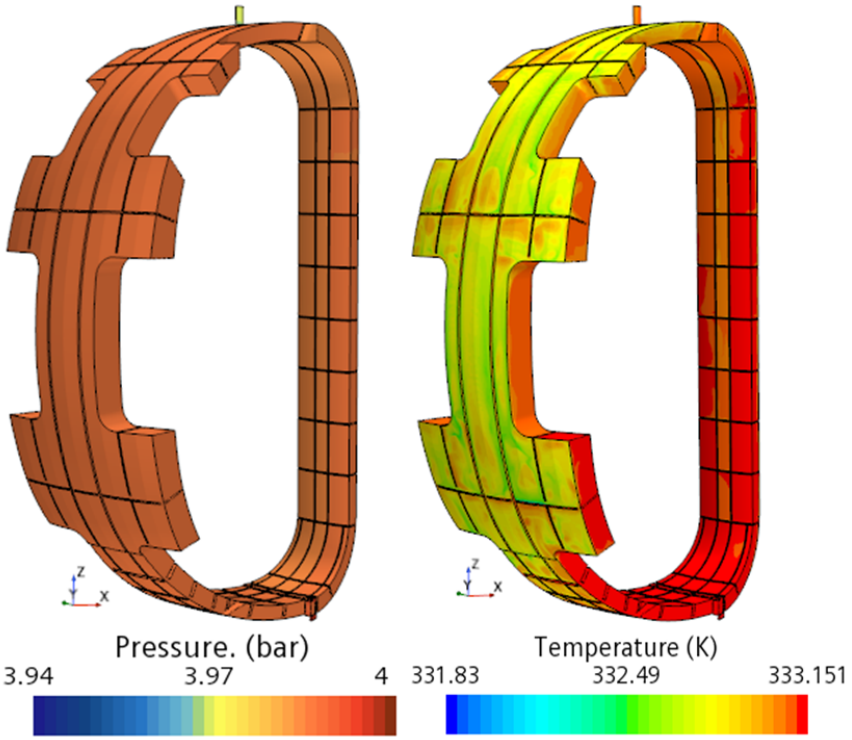

Figure 4.6: Pressure and Temperature scalar scenes for CV1. Looking at the pressure field (left), it can be noticed that pressure drops are concentrated at inlet and outlet regions, while in the rest of the domain pressure is almost uniform. From the temperature scene (right) it can be noticed that the minimum temperature is coherently experienced at the outer wall and that the lower velocity in IB2 results in a lower temperature w.r.t IB1 and IB3 channels.

at the updated distribution of toroidal ribs in the bottom region of the VV, introduced to provide structural support to the divertor rail as discussed in section 2.2.

- Being the extension of the outer wall surface very similar to the one of the old design and the radiative negative load kept unchanged, the resulting outlet, minimum and maximum temperatures are almost unaffected by the updated desing.

Accuracy in the results however is not the only thing that has to be considered in numerical computing.
CtFD simulations carried out on such high number of cells require huge amount of computational power. Unfortunately, numerical performances typically do not scale linearly with respect to the number of workers (cores) over which the simulation is run. For this reason, this concluding paragraph addresses the evaluation of the computational cost for medium and fine steady/unsteady simulation, with the estimation of the parallelization efficiency and the memory request evaluated through the built-in *Star-CCM+ -benchmark* flag. The latter allows the estimation of numerical performance of specific simulation on the specific employed hardware. As far as the latter is concerned, the performances have been evaluated on **MARCONI**, one of the most powerful supercomputer (theoretical peak performance of 18.82 PFlop/s) of the italian High Performance Computing (HPC) CINECA[1].

The report generated by *Star-CCM+* contains lots of interesting information, but for the present work it is sufficient to focus on two of them specifically.
The first information is the simulation speedup: the latter provides an indication of *how good* additional workers are exploited to carry out the simulation. Assuming 100% Parallel Efficiency (PE), by doubling the number of workers (e.g. passing from 48 to 96) each iteration should be done twice as fast as recorded in the reference case. In reality this is never the case and PE lower than 100% are expected. In figure 4.7 (a) and (b) the speedup for medium/fine both steady/unsteady simulation is reported. It can be noticed that medium steady simulation scales quite efficiently, while medium unsteady it is already below 50% PE at 96 cores. For the fine mesh instead, the PE saturates at 480 cores for the steady simulation while the unsteady ones scales quite efficiently up to 1440 cores.
The second information that it's worth reporting is instead the average resident high watermark (HWM) memory per host. To simplify, this parameters is an indication of which RAM percentage of the host is occupied (on average) by the processes related to the simulation. Differently from the PE, this time lower RAM usage is preferred.
This last parameter is reported in figure 4.7 (c) for all the explored simulations. Coherently, being the total cell count ratio equal to three between medium and fine meshes, the requested RAM (when considering the single host, 48 cores) is also three times larger.

[1]More information about CINECA Consortium and MARCONI architecture are available at: https://www.cineca.it/

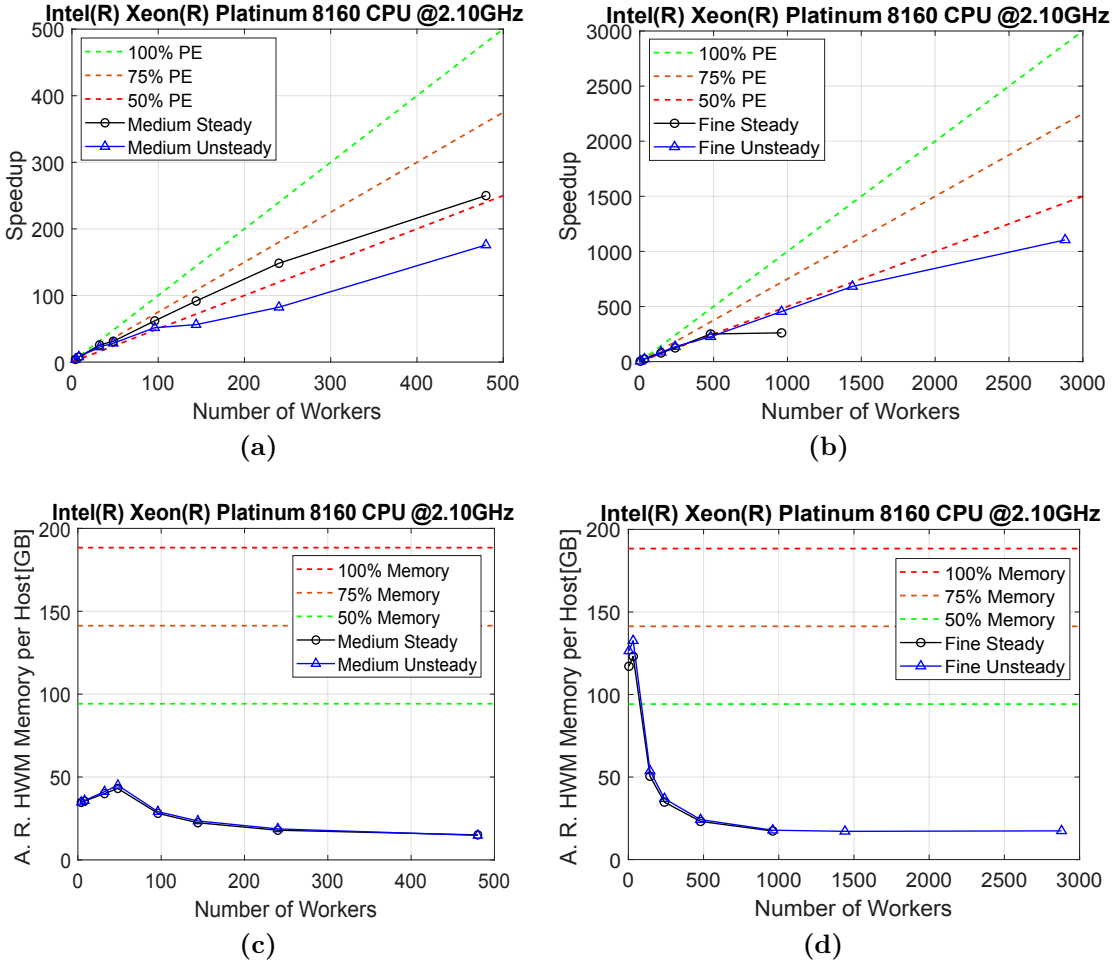

Figure 4.7: (a) Speedup for medium steady and unsteady simulations according to the number of workers (cores) exploited. (b) Speedup for fine mesh steady/unsteady simulations. Higher the parallelization efficiency (PE) better it is. (c) Averaged Resident High Watermark (HWM) Memory usage per host according to the number of workers fo medium simulations and fine ones (d). Lower memory usage is better (100% memory refers to single host memory of 188.4 [GB]). All benchmarks are evaluated on the *Intel(R) Xeon(R) Platinum 8160 CPU @2.10GHz* chip.

From the convergence study, coupled with the above-mentioned evidences for what regards the computational cost, it can be concluded therefore that the medium mesh ($\approx$ 6 million cells) with a steady solver represents the best compromise in terms of computational cost and accuracy to estimate the mean values; unsteady uncertainties will then be added. However, in case of suspicious behavior of the simulation reports (i.e too large fluctuations, as it will be discussed for special

control volumes CV6, CV7 and CV9) it is always suggested to carry an unsteady simulation with the finest mesh to avoid possible misleading results.
Lastly, it must be stressed that all the reported results still miss the validation process, which is typically done by comparing the numerical outputs with results coming from experiment. Unfortunately, no experiments are foreseen to test thermal-fluid dynamics results.

4.1.5 Mass Flow Rate Distribution and Stagnation/Reverse Flow Evaluation

One of the key output expected from the TH analyses, beyond the estimation of pressure drops and of critical spots in terms of too hot/too cold temperatures if any, is to provide an indication of how the borated water is distributed between the different available paths inside the CV.
As already specified, the following reasoning is developed having in mind the specific geometry of CV1-R, but it can be extended similarly for all the CVs of the VV with few/no modifications.

As shown in figure 4.1, and as already anticipated in the summary of previous work done by the NEMO group, the CV can be always macroscopically divided into an outboard and an inboard legs, which hydraulically communicate at inlet and outlet sections only.
The first indication that the TH simulation must provide therefore is if the mass flow rate in these two regions is balanced or not, highlighting possible macroscopical undesired imbalances between the two (which will be translated into strong flow resistance imbalances).
More in details, it can be appreciated that both IB and OB legs are then further divided into three parallel paths: the estimation of the amount of coolant flowing in each channel is key to spot possible imbalances within the same leg, which have to be avoided as much as possible to homogenise pressure and temperature fields.
If attention is focused on the OB leg of CV1-R (but again it can be extended to all the CVs), it can be noticed that the three parallel channels are not hydraulically independent thanks to the presence, at different sector's heights, of holes in the poloidal ribs. For that reason the estimation of the mass flow rate distribution in a single horizontal section may not capture possible flow's imbalances at different CV's latitudes.
To provide a more refined estimation of the borated water distribution the mass flow rate is therefore evaluated in each channel (three OB channels and three IB channels respectively) at three different latitudes, for a total of 18 measurements as shown in figure 4.8.
The discrete map of mass flow rate distribution is also a powerful but simple tool

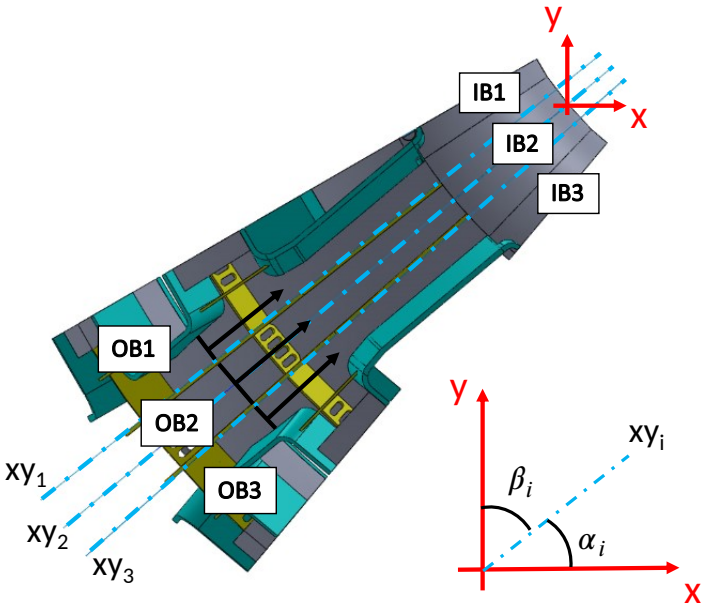

(a) *Top view.*

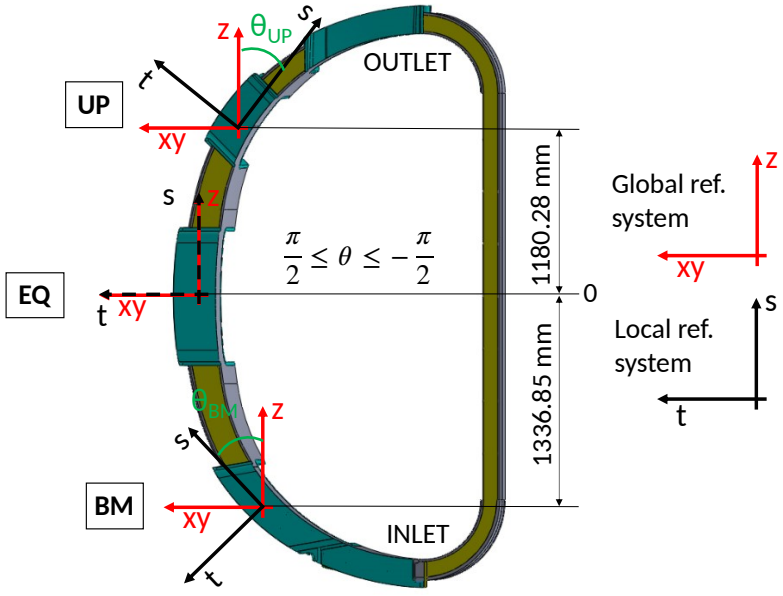

(b) *Side view.*

Figure 4.8: Visualization of the orientation (a) and latitude (b) of the 18 resulting cross-sections exploited for mass flow rate and backflow evaluation in the six OB/IB parallel channels.

to check if the numerical solution is physically acceptable: the sum of measured mass flow rates must always recover the total mass flow rate prescribed at the inlet, verifying continuity equation.
However this output does not provide a qualitative indication of the flow inside each channel, because the identification of severe recirculation or stagnation zones cannot be immediately retrieved from global information.
To do that, plots of velocity distribution at each section are helpful to capture where recirculation is strong.
However, differently from mass flow rate estimation, velocity plots are focused only in the component V_s which is locally tangent to the orientation of the channel: at the equatorial plane recirculation can be easily spotted by highlighting negative values of $\mathbf{V}(z) = w \equiv V_s$, since the orientation $\mathbf{s}$ of the channel coincides with z axis. This is the case also for up and bottom IB sections.
The previous statement is no longer true when bottom or the top sections of the outboard leg are considered since here the local orientation $\mathbf{s}$ of the channel creates positive and negative θ angles with respect to the z axis respectively. It means that in these regions, if only the w component of the velocity is considered the recirculation can be remarkably over or under-estimated as shown for a simpler 2D case in figure 4.9, where also the orientation φ of the velocity vector $\mathbf{V}$ with respect to $\mathbf{s}$ is taken into account as well.

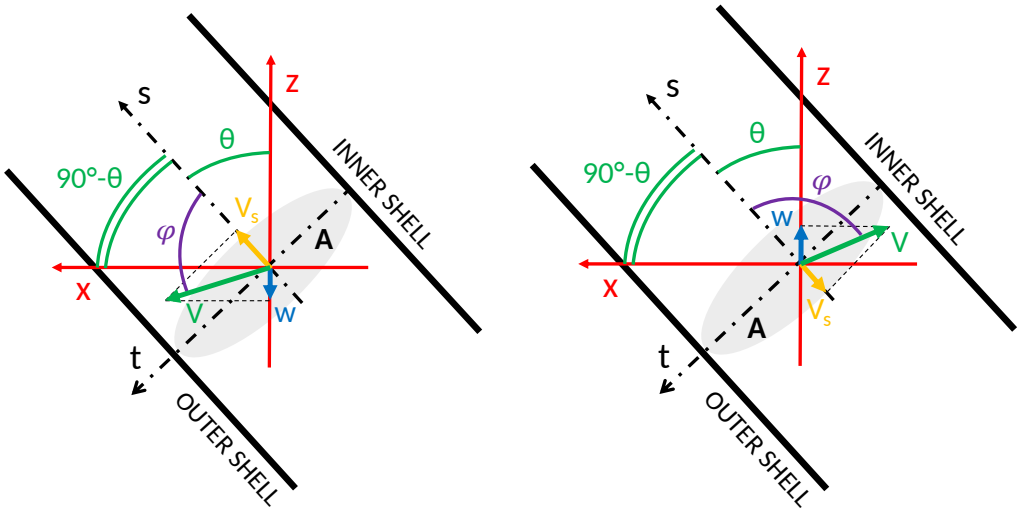

(a) $w < 0$. **(b)** $w > 0$.

Figure 4.9: Simpler 2D schemes where despite $w < 0$ no backflow occurs (a) and where, even if $w > 0$, backflow occurs (b).

For the mass flow rate estimation instead the local orientation of the channel is automatically taken into account in the analytical formulation of the mass flux itself, and therefore, when solution has reached convergence, the orientation of the plane does not have an influence on its computation.
Anyhow, the CV is a three dimensional object corresponding to a 20° slice of the VV torus, and for that reason each outboard channel is also characterized by its own orientation xy_i in the horizontal plane as already shown in figure 4.8.
This orientation, described by complementary angles α_i and β_i, must be taken into account to project the u and v components of the velocity vector along direction $\mathbf{s}$, as follows:

$$V_s = (\pm u \cos(\alpha_i) \pm v \cos(\beta_i)) \sin(\theta) + w \cos(\theta) \tag{4.8}$$

The $\pm$ signs are dependent to which quarter of the horizontal plane contains the projection of $\mathbf{s}$: even if each CV will show different combinations of signs, it can be easily derived that the latter are perfectly inverted when considering bottom and up cross-sections. Bottom and up θ angles are instead invariant for all the CVs.
To speed up the procedure, a Java Macro has been developed to already set field functions, parameters and scenes for the complete reverse flow visualization, minimizing thus manual operations:

- Eight Parameters:
  - Θ_{BM}
  - Θ_{UP}
  - α_i $(x3)$
  - β_i $(x3)$
- Six Field Functions:
  - $V_{s_{bottom,i}} = (\pm u \cos(\alpha_i) \pm v \cos(\beta_i)) \sin(\theta_{BM}) + w \cos(\theta_{BM})$ $(x3)$
  - $V_{s_{up,i}} = (\mp u \cos(\alpha_i) \mp v \cos(\beta_i)) \sin(\theta_{UP}) + w \cos(\theta_{UP})$ $(x3)$
- Six Scalar Scenes:
  - revIBbottom
  - revIBeq
  - revIBup
  - revOBbottom
  - revOBeq
  - revOBup

	Mass Flow Rate Fraction [-]			
Channel	**Bottom**	**Equatorial**	**Up**	**Tot**
OB1	12%	18%	26%	56%
OB2	24%	24%	21%	
OB3	20%	14%	9%	
IB1	21%	21%	21%	44%
IB2	4%	4%	4%	
IB3	19%	19%	19%	
TOT	100%	100%	100%	100%

Table 4.5: Mass flow rate repartition inside CV1 OB and IB channels. Reported mean values are taken from unsteady fine results. Of the total mass flow rate ($\dot{m}_{TOT} = 1.11$ [kg s^{-1}]), ≈ 620 [g s^{-1}] goes to the OB leg while remaining ≈ 490 [g s^{-1}] to the IB leg.

With all of that being said, the mass flow rate distribution in CV1 is summarized in table 4.5, while scenes of the reverse flow are presented in figure 4.10.
The coolant repartition between OB/IB legs results to be sufficiently balanced, without severe decompensations.
On the OB leg, OB2 and OB3 channels show larger mass flow rate at the bottom in view of their proximity to the inlet. By approaching the outlet, borated water starts flowing to the OB1 channel through the toroidal connections as expected.
At the inboard instead, the central paths is characterized by a significant smaller mass flow rate with respect to neighbouring channels which is a consequence of the reduced cross sectional area.
Despite the lower mass flow rate, no criticalities in terms of temperature or pressure are found.
As far as recirculation is concerned, as shown in figure 4.10, it is basically limited to small areas of the domain and it doesn't represent a particular issue. The strongest recirculation is detected at the bottom of IB3 where the elevated fluid velocity, due to inlet proximity, participates in the creation of a region of strong and quite chaotic recirculation. Of course larger backflow (or in general more chaotic fluid motion) is expected at the bottom region of the CV, since here the fluid hasn't had the time to re-organize itself yet; as the upper region of the CV is approached instead the fluid become more and more uniform, as V_s scalar scenes confirm.

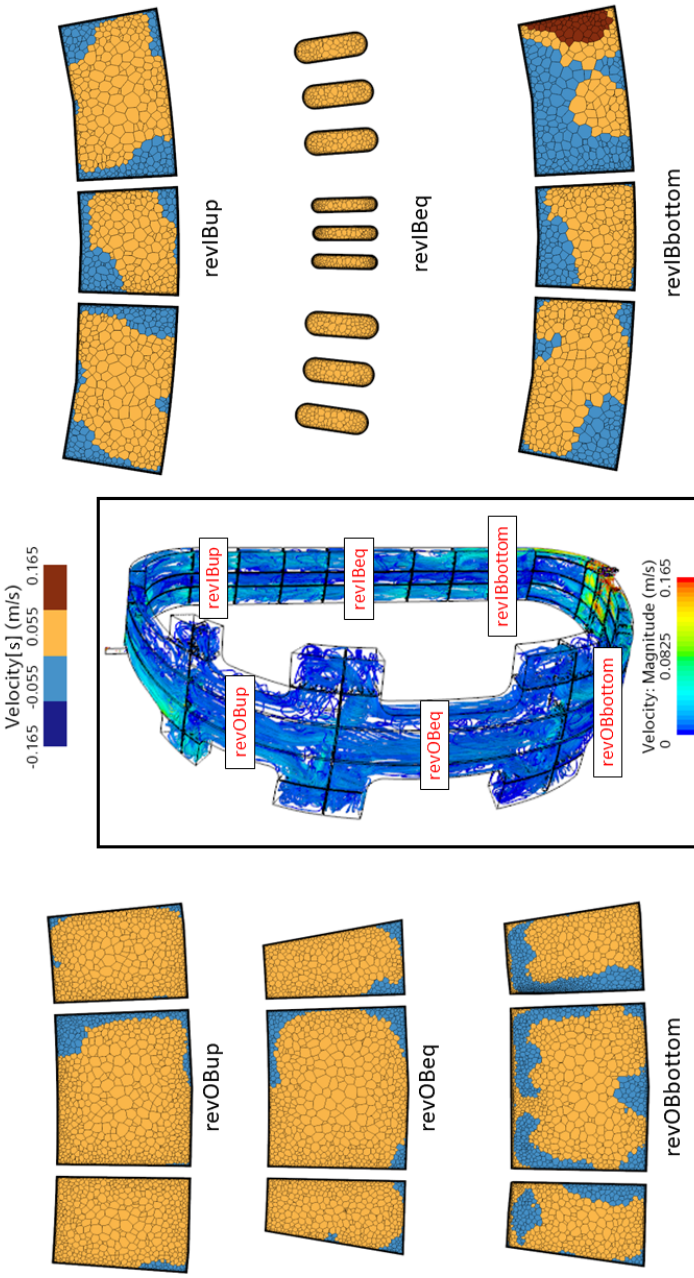

Figure 4.10: Visualization of positive and negative flow regions for the 18 cross-sections (six scalar scenes). The color code is the following: blue-strong backflow, sky blue-moderate backflow, orange-moderate positive flow, red-strong positive flow.

4.1.6 System-Level Hydraulic Characterization

In this section, starting from the results obtained for the regular control volume CV1-type R, the general methodology followed to define the hydraulic characteristic of each geometry is summarized briefly.
Despite the complex multiple paths of borated water inside the control volume, for a pure-hydraulic system-modelling point of view each control volume can be seen as a black box (see figure 4.11) with an inlet and an outlet where, from continuity, $\dot{m}_{INLET} \equiv \dot{m}_{OUTLET}$:

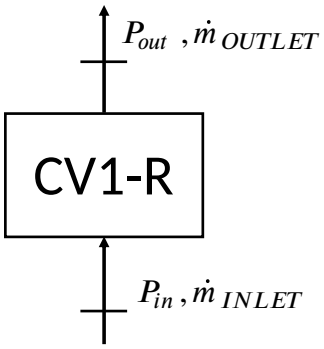

Figure 4.11: Black box schematization of CV1-type R.

With this representation, the CV can be seen as an obstacle in the hydraulic circuit characterized by its own localized pressure drop (also called as "*Minor Losses*"), which could be analytically defined as:

$$\Delta p = k_{\Delta p} \frac{V^2}{2} \rho$$

being $k_{\Delta p}$ the loss coefficient.
More in general however, as dimensional analysis can justify, the relation between pressure drops and velocity (or mass flow rate) is quadratic.
Moreover, since when $\dot{m} = 0$ then also $\Delta p = 0$, the most general quadratic function $a_{CV\#}\dot{m}^2 + b_{CV\#}\dot{m} + c_{CV\#}$ will have its vertex laying on the origin of the $\Delta p - \dot{m}$ plane, meaning that $b_{CV\#} = c_{CV\#} = 0$:

$$\Delta p = a_{CV\#} \cdot \dot{m}^2 \tag{4.9}$$

The couple $(\dot{m}, \Delta p)$ obtained from TH simulation is therefore sufficient to fully characterize the quadratic function:

$$a_{CV1} = \frac{\Delta p_{CV1}}{\dot{m}^2_{INLET}} = \frac{2732.14\ [\mathrm{Pa}]}{1.11^2\ [\mathrm{kg\,s^{-1}}]^2} \approx 2217.5 \quad [\mathrm{Pa\,s^2\,kg^{-2}}] \tag{4.10}$$

At this point, two important considerations have to be done:

1. The quadratic relation above does not account for buoyancy forces where, in section 3.5, the latter have been shown to be not negligible. The quadratic approximation is a priori not correct therefore.

2. As initially highlighted from steady-state analyses and then confirmed by unsteady ones, the pressure drop of the control volume oscillates within a range of ±115 [Pa] around the average value used in eq. 4.10. A single quadratic relation does not account for that.

The point raised from consideration n°1 can be investigated by verifying the goodness of the quadratic approximation when an off-nominal working point is considered for CV1.
As it will be shown in next sections, the pressure drop at nominal mass flow rate is different (as expected because of different geometries) among the different control volumes.
This condition will introduce pressure imbalances which will in turn cause mass flow rate imbalances: when all the CVs are hydraulically connected, positive or negative deviations from nominal simulated conditions are expected.
The magnitude of such imbalances however will be proportional to the pressure imbalances at the nominal working point.
It means that a reasonable off-nominal working point for CV1, needed to verify the goodness of the quadratic approximation, should be selected in order to be representative of what could really happen inside the VV: simulating 20% of the nominal mass flow rate to then get a pressure drop which is not well fit by the quadratic function doesn't tell anything about the effectiveness of such approximation since, if that condition (20% of nominal mass flow rate) is verified, the goodness of the approximation will be the least of the problems, being the mass flow decompensation between VV sectors not acceptable a priori.
To find a coherent off-nominal working condition, the pressure drops of each control volume (average results from medium mesh or fine mesh when available) are compared with the quadratic approximation, which in turns takes into account the physical fluctuations, as shown in figure 4.12.
From the same figure it ca be noticed that control volumes CV11 and CV7 are the ones characterized with the highest and the lowest pressure drops respectively. By intercepting such values with the hydraulic characteristic of CV1, minimum and maximum reasonable (but conservative) mass flow rates are identified:

$$\dot{m}_+ \approx 1.19,\ \dot{m}_- \approx 1.05\ [\mathrm{kg\,s^{-1}}] \tag{4.11}$$

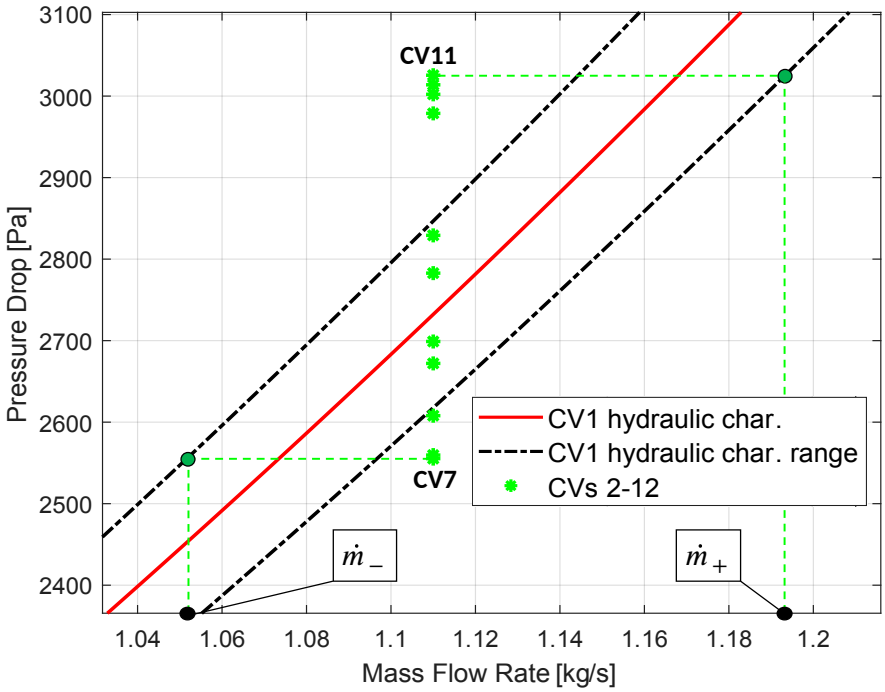

Figure 4.12: Conservative estimation of mass flow rate variation from CV1 hydraulic char. and other CVs computed pressure drops.

It means that a reasonable mass flow rate deviation for CV1 is less than 10% with respect to the nominal value. The effectiveness of the quadratic approximation should be therefore verified in the range $1.11 \pm 10\%$.
The pressure drop for CV1 has been therefore evaluated for an inlet mass flow rate of $\dot{m}_{off-nominal} = 1$ [kg s^{-1}], exploiting the finest mesh and the unsteady approach. A lower mass flow rate has been chosen to avoid possible y^+ constraints violation. The comparison between the simulated pressure drop in off-nominal condition and the hydraulic characteristic of CV1 is presented below in figure 4.13.
The relative deviation between computed and expected pressure drop is equal to:

$$\Delta\% = \frac{2217.5 - 2200}{2200}\% = 0.8\% \tag{4.12}$$

By considering the result found above it can be concluded that, around $\pm 10\%$ of the nominal mass flow rate, the quadratic approximation is a reasonable choice. This methodology will be therefore implemented for all the VV CVs.

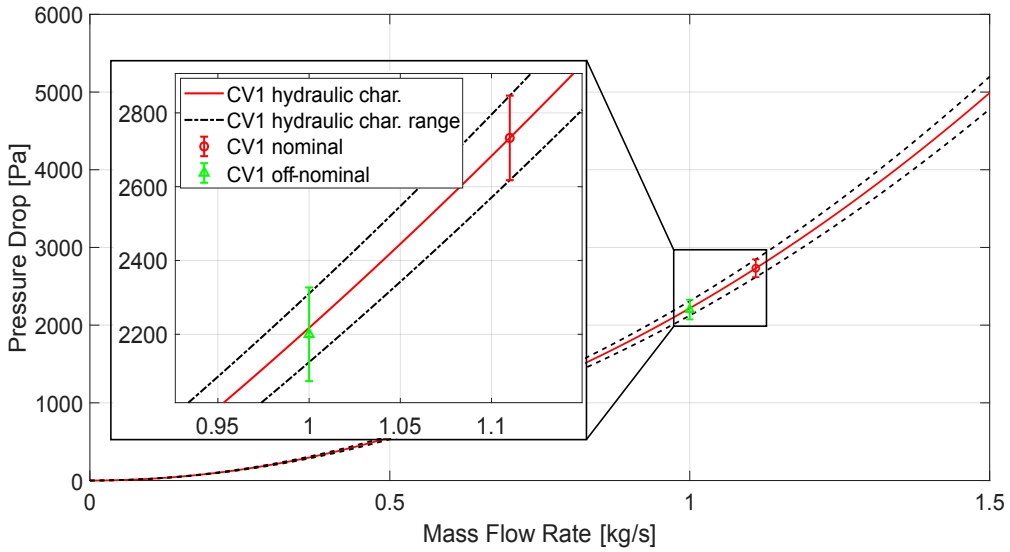

Figure 4.13: Comparison between simulated off-nominal condition and quadratic the approximation. The relative deviation of 0.8% between the two values confirms that the quadratic approximation is appropriate.

4.2 Other Regular Sectors: CV2-CV3

As already explained at the beginning of this chapter, CV1 has been used to investigate the sensitivity of the model to some simulation choices/parameters and to verify the goodness (verification through mesh independence study) of the numerical solution.
The same model therefore, with the mesh medium and an *all* y^+ wall treatment, has been employed to investigate and characterize also the steady-state thermal-hydraulic behaviour of regular control volumes CV2 and CV3.
For sake of brevity, lots of details concerning these two will not be reported here, and only the most relevant results will be presented in this section.

Starting from the geometry, as can be appreciated in figure 4.14, the overall design of CV2 and CV3 is very similar to the one of CV1, with small differences mainly concentrated in the lower part of the domain.
In fact, for being adjacent to the first regular control volume, CV2 shares the same inlet topology while for CV3 the situation is a little bit different. As it can be noticed at the bottom of figure 4.14 (b), the inlet pipe is located behind one of the VV supports (in green), and for that reason its elongation is more than twice the elongation of CV1/CV2 inlet pipe, to simplify future connections with the coolant distribution ring as already discussed in chapter 2.

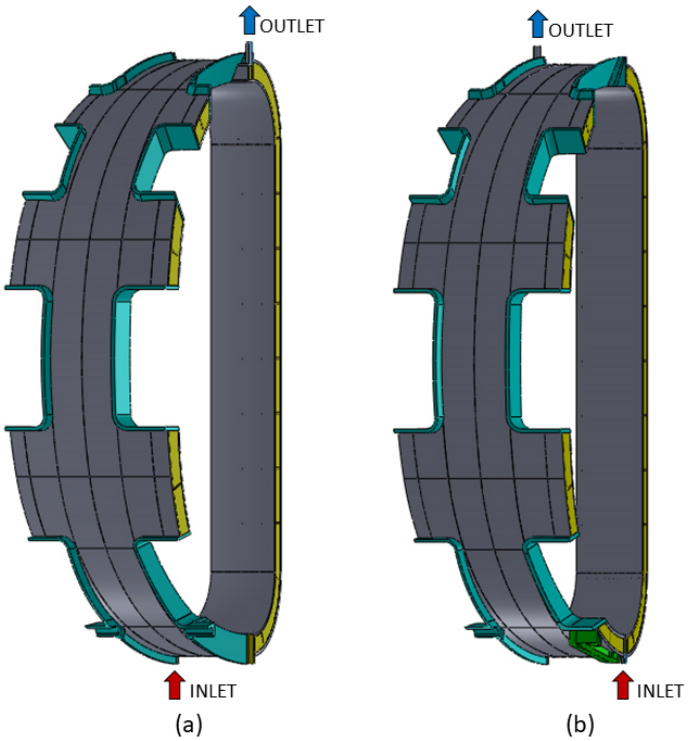

Figure 4.14: (a) CV2-type L geometry. (b) CV3-type R geometry. Relevant differences are found at the inlet section. See figure 4.15 for more details.

Moreover, also the topology of the inlet is different: in CV3 the IB/OB distribution chamber is characterized by three apertures (two OB, one IB) rather than two (one OB, one IB) as shown in figure 4.15. The longer pipe combined with the different distribution chamber topology has indeed an effect on the overall computed pressure drop as it will be discussed below.

In tables 4.6 and 4.7 key features and simulation outcomes of CV2 and CV3 are presented respectively. It can be immediately noticed that CV2 pressure drop is in line with the one characterizing CV1 while for CV3 pressure losses are significantly larger.
The suspicious falls right on the different inlet, which can be considered the main suspect for larger pressure drops. Further investigations done by comparing pressure distribution and streamlines confirm that hypothesis: in figure 4.16 it can be appreciated that for CV3 (b) the pressure is already lower than 3.99 [bar] almost everywhere outside the inlet distribution chamber, differently from CV1 (a) where the pressure is still above that threshold even in the farthest inboard channel from the inlet.

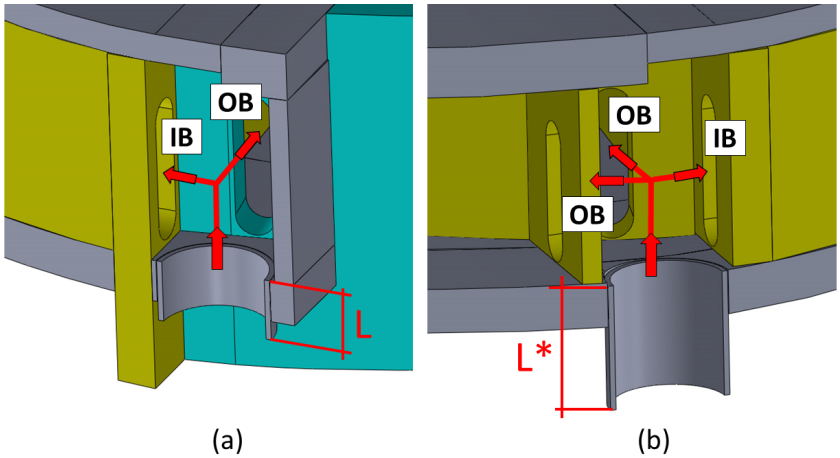

Figure 4.15: (a) CV2 two-way inlet, with inlet pipe length $L = 32$ [mm]. (b) CV3 three-way inlet, $L^* = 65$ [mm]. The additional aperture oriented towards the OB leg is needed because of the missing port #5 on CV3 right-end side, which introduces an additional chamber for the fluid.

Looking at the mass flow rate repartition between IB/OB legs, CV2 appears even more balanced than CV1 while for CV3 the coolant flow is quite biased to the OB leg. This last consideration is again a consequence of the different inlet topology and it was somehow expected due to the extra aperture towards the outboard leg in CV3 inlet distribution chamber. The streamlines comparison between CV1 and CV3 done in figure 4.16 (c) and (d) it's the most effective way to visualize such disproportion.
The reported streamlines are generated by integrating forward the velocity field to get fluid particles trajectories, starting from the inlet surface as source seed: since streamlines generation is randomized over inlet domain cells, the number of resulting streamlines in each IB/OB channels is actually proportional to the amount of fluid following a specific paths and it already provides a qualitative info about borated water mass flow rate repartition. In 4.16 (d) it is clearly evident that the IB leg has less streamlines flowing in it. It must be stressed though that this is a powerful instrument to visualize some information on a *qualitative* way but it does not substitute the exploitation of dedicated mass flow rate reports in each channel.

Regarding the thermal point of view, the slightly larger outlet temperature found for CV2 is coherent with its lower outer wall surface: considering equal mass flow rate at nominal condition, a smaller surface results in a lower thermal load and in turn in a larger outlet temperature from the first law of thermodynamics.
Anyway, detected outlet temperature differences are totally negligible ($\approx 10^{-2}$ [K])

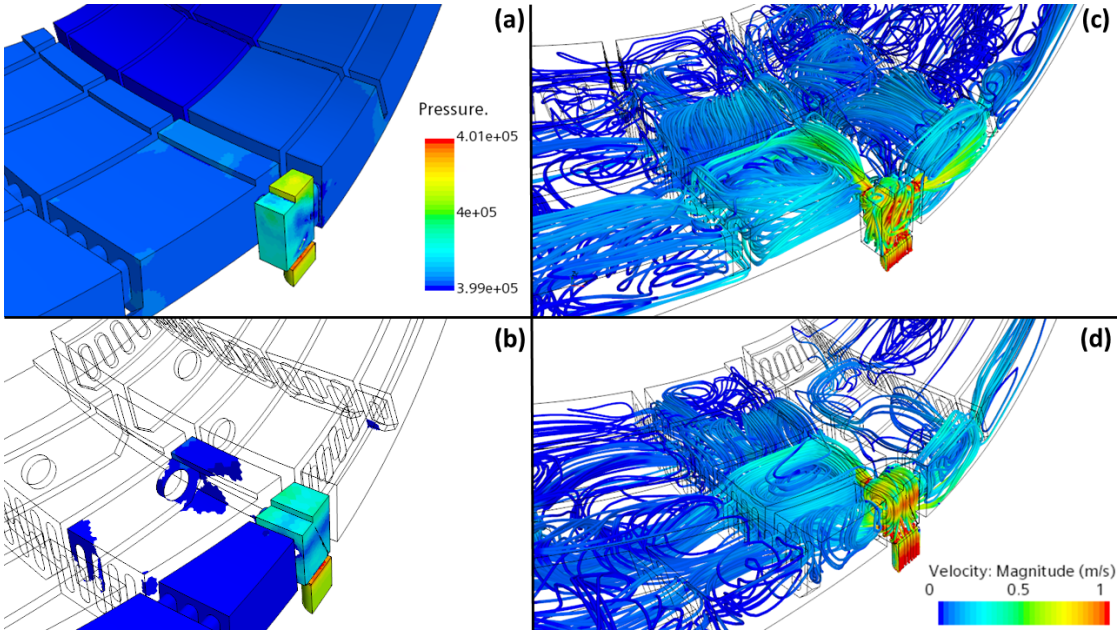

Figure 4.16: On the left, the comparison between CV1 (a) and CV3 (b) pressure fields at the inlet section. The legend is deliberately cropped at 3.99 [bar] to show that the coolant enters the core of CV3 domain with a pressure already below that threshold. On the right, streamlines comparison of CV1 (c) and CV3 (d) respectively, using inlet surface as source seed with 15x15 grid points. Streamlines color is related to the local velocity of the fluid particle following that path.

General Info	
CV	2
CV type	Regular
Sectors	S13,14,16,17
Hydraulic Sectors	i7,9
Inlet	R/L
Fluid Volume [m³]	0.693
Outer Wall Surface [m²]	5.43

Results	
Δp **[Pa]**	2783 ± 115
T_{out} **[K]**	333.07
T_{max} **[K]**	333.15
T_{min} **[K]**	331.90
$\dot{m}_{OB}$ **[g s^{-1}]**	599 ± 20
$\dot{m}_{IB}$ **[g s^{-1}]**	511±20

Table 4.6: Relevant geometric and simulation info for CV2. Results are taken from steady medium simulation, coupled with the uncertainties found for CV1 unsteady fine.

and from a system point of view the three regular sectors behave almost identically (the IB/OB decompensation in CV3 is not an issue for such small heat flux).

General Info	
CV	3
CV type	Regular
Sectors	S2,3,14,15,16
Hydraulic Sectors	I2,8
Inlet	R/L
Fluid Volume [m^3]	0.697
Outer Wall Surface [m^2]	5.55

Results	
Δp [Pa]	3003 ± 115
T_{out} [K]	333.06
T_{max} [K]	333.15
T_{min} [K]	331.99
$\dot{m}_{OB}$ [g s^{-1}]	702 ± 20
$\dot{m}_{IB}$ [g s^{-1}]	408 ±20

Table 4.7: Relevant geometric and simulation info for CV3. Results are taken from steady medium simulation, coupled with the uncertainties found for CV1 unsteady fine.

To conclude, mass flow rate repartition within IB/OB channels is also similar (in terms of mass fractions %) to the one found for CV1: common features such as larger coolant flow at the bottom of the OB channel closer to the inlet and lower mass flow rate in the central path (IB2) of the IB leg are present.
No relevant issues have been found as far as stagnation/recirculation is concerned.
More details on borated water distribution, 3D temperature and 2D V_s scalar scenes for CV2-3 are available in appendix B.

4.3 Special CVs

Having analysed the borated water repartition among the regular sectors, the investigation proceeds with the CtFD analyses of special control volumes. In the following sections, a brief description of the 9 geometries is presented, with a focus on the main differences with respect to regular sectors.
Again, for sake of brevity, only the most relevant thermal-hydraulic results will be presented and discussed.
Differently from the regular CV1 (and of very similar CV2-3), this is the first time that VV special sectors are simulated and therefore no comparisons can be done with previous analyses.

4.3.1 CV4-CV5

The characterization of special sectors starts from control volumes CV4 and CV5. Their geometries are strongly related to the ones of CV2 and CV3 respectively (see figure 4.17), but some details make these two special and not regular.
Starting from CV4 for instance, it acts as a link between multi-sectors A and B.

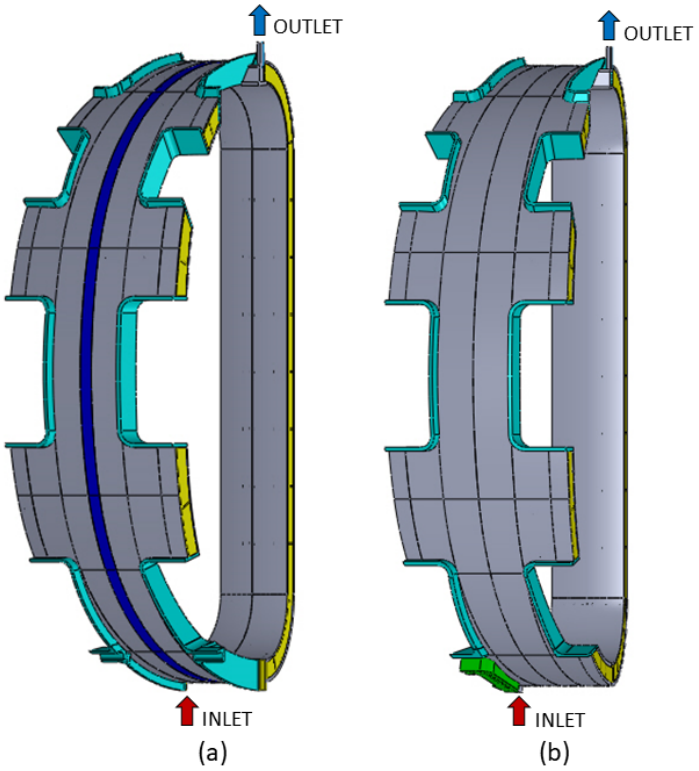

Figure 4.17: (a) CV4-type L geometry. (b) CV5-type L geometry.

For that reason, the latter is provided with 14 screwed plugs located in 7 different regions which are employed to isolate multi-sectors A and B respectively during the pressurization test.
As can be appreciated in figure 4.18, these sector's plugs are only screwed and they will be removed, in case of positive outcome from pressurization tests of course, to guarantee the hydraulic connection between the two VV multi-sectors during normal operation.
Moreover, being CV4 assembled on site, left and right pieces will be connected trough a splice plate, represented in blue in figure 4.17 (a) and 4.18.
The greatest difference between CV2 and CV4 is a consequence of this peculiar assembling decision: the integration of the splice plate will result in a missing buttonhole in the toroidal ribs of the central channel, outboard side.

Regarding special control volume CV5, it is instead strongly related with regular control volume CV3. The only relevant difference can be found again focusing the attention on the lower part of the CAD: differently from CV3, CV5 does not have port #5 on both sides, resulting in a wider bottom region.

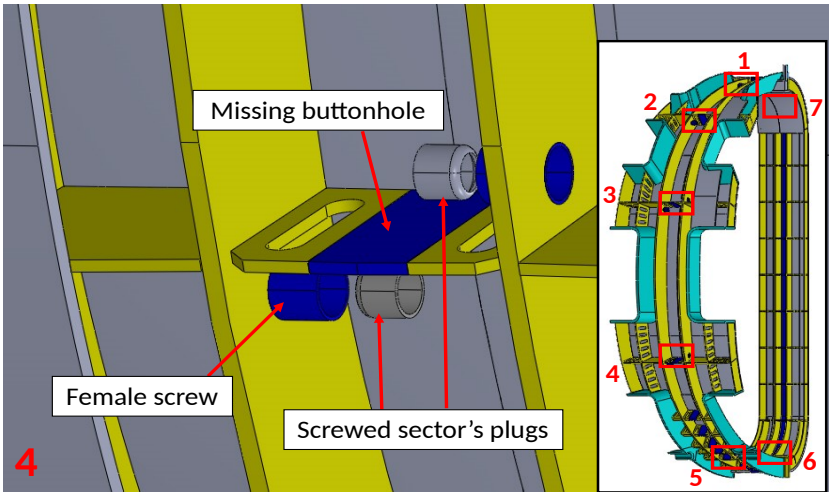

Figure 4.18: Close-up on CV4 sector plugs in region four. The female screw will not be removed after pressurization tests. The missing buttonhole in OB2 is the major difference with respect to regular CV2.

Despite that, inlet topology and mid/upper regions are the same of CV3 and therefore similar thermal-hydraulic performances are expected.

By looking the the CtFD results in table 4.8 for CV4 and in table 4.9 for CV5, it can be noticed that pressure drops are in line with CV2 and CV3 respectively, as the similar geometry suggested from the beginning.
However, looking at the mass flow rate repartition between IB/OB legs it can be noticed that for CV4 the latter is less balanced than CV2 case, with the coolant flowing preferentially in the OB leg.
As far as CV5 is concerned instead, the coolant distribution biased towards the OB leg is in line with what has been concluded for CV3.

Going deeper on the mass flow repartition, it is worth mentioning that, the mass flow rate distribution in CV4 OB leg is quite peculiar: the central channel OB2 is the one characterized by the lower mass flow rate.
Differently from other CVs in fact, where the lowest mass flow rate was always experienced in the furthest path from the inlet (bottom region), the larger hydraulic resistance in OB2 due to the missing buttonhole has indeed a remarkable effect.
Anyway, this peculiar coolant distribution does not represent an issue in terms of pressure/temperature distributions.
To conclude, what can instead represent an issue is the mass flow rate flowing in the inboard channel IB2: here only 1.5% of the total flow is measured.
This result, despite being coherent to what detected in other sectors from a relative

point of view (IB2 is always characterized by the lowest mass flow rate), is not optimal in absolute term: the flow distribution imbalance between inboard channels is even more stressed, passing from average values of mass flow rate in IB2 of $3-4\%$ to only 1.5%.
At nominal mass flow rate, the larger imbalance detected in IB2 still not represents an issue, but it should be highlighted as not optimal and future optimizations are therefore suggested.
For complete mass flow repartition tables, temperature scalar scenes and reverse flow evaluation of CV4 and CV5, see appendix B.

General Info	
CV	4
CV type	Special
Sectors	S1,2
Hydraulic Sectors	i1
Inlet	L
Fluid Volume [m^3]	0.692
Outer Wall Surface [m^2]	5.50

Results	
Δp **[Pa]**	2673 ± 115
T_{out} **[K]**	333.07
T_{max} **[K]**	333.15
T_{min} **[K]**	328.52
$\dot{m}_{OB}$ **[g s^{-1}]**	630 ± 20
$\dot{m}_{IB}$ **[g s^{-1}]**	480 ±20

Table 4.8: Relevant geometric and simulation info for CV4. Results are taken from steady medium simulation, coupled with the uncertainties found for CV1 unsteady fine.

General Info	
CV	5
CV type	Special
Sectors	S3,4
Hydraulic Sectors	i2
Inlet	L
Fluid Volume [m^3]	0.702
Outer Wall Surface [m^2]	5.62

Results	
Δp **[Pa]**	3014 ± 115
T_{out} **[K]**	333.06
T_{max} **[K]**	333.15
T_{min} **[K]**	332.05
$\dot{m}_{OB}$ **[g s^{-1}]**	697 ± 20
$\dot{m}_{IB}$ **[g s^{-1}]**	413 ±20

Table 4.9: Relevant geometric and simulation info for CV5. Results are taken from steady medium simulation, coupled with the uncertainties found for CV1 unsteady fine.

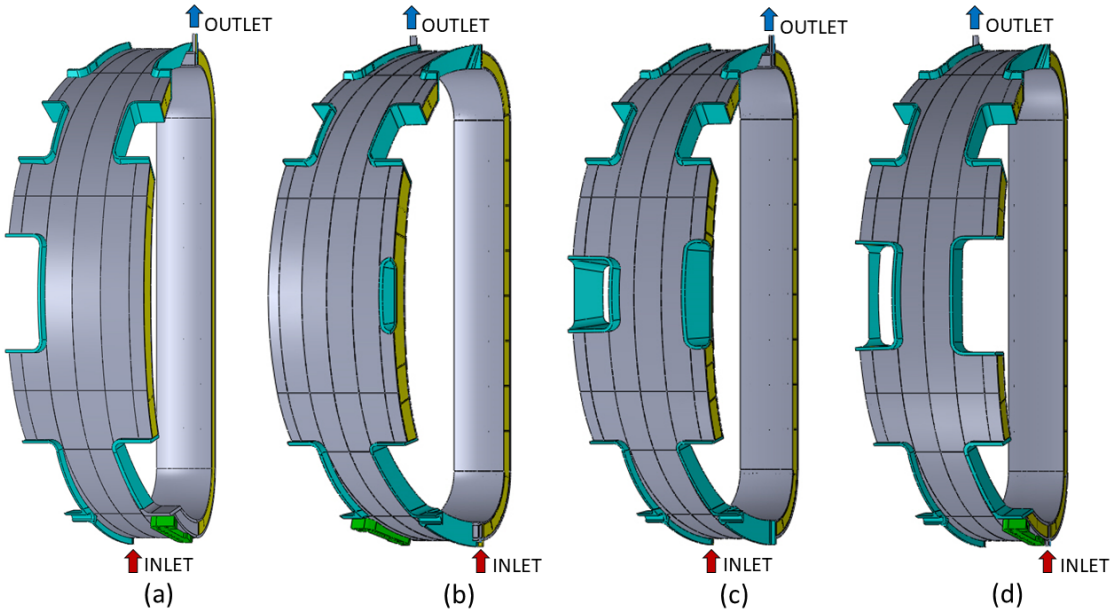

Figure 4.19: (a) CV6-type L, (b) CV7-type R, (c) CV8-type L and (d) CV9-type R geometries.

4.3.2 Negative-Neutral Beam Injector Module: CV6-7-8-9

Continuing the analysis of VV special control volumes, when moving counterclockwise the Negative-Neutral Beam Injector (NNBI) Module (80° toroidal development) is encountered.
As already presented in chapter 2, the NNBI module was initially designed to host two co-tangential injectors located at the equatorial level, in the so-called "double-source" configuration.
It is clear that the VV design was developed having constantly in mind the concept of components' *integration*: a Tokamak reactor is an extremely complex machine that requires several sub-components specifically designed to pursue a distinct goal minimizing the negative effects on other, usually in competition, goals.
Talking about the NNBI specifically, its main function is to provide energy to the plasma by shooting highly energetic neutral particles, in order to keep the plasma temperature sufficiently high for fusion reactions to happen when the intrinsic ohmic heating becomes negligible due to decreasing resistivity of the plasma itself.
Without going in details on the complex mechanisms and interactions that regulate the energy exchange between injected and plasma particles, it is sufficient to know that the injection is not radial, but tangential to not impinge on the wall right in front of the injectors.
This is why the equatorial ports where the two NNBI was foreseen to be installed

are skewed and not radially oriented (sectors 7-8, control volumes 8-9).
In 2020 the NBI module was subjected to a reengineering process which led to the "single-source" configuration, still preserving though two skewed equatorial ports. Moreover, NNBI structure is majestic (it occupies a dedicated building which is as big as the entire Tokamak ones) and for that reason it is almost impossible to locate additional devices for diagnostic/control in the VV sector right before. For that reason, sector S6 (control volumes CV6-7) does not have the equatorial port.

The extracted geometries of these four control volumes are presented in figure 4.19. The already introduced geometric peculiarities have several consequences on the fluid flow: first of all, the missing equatorial port in sector S6 has an effect on the outer wall surface of CV6-7, which is larger than regular CVs resulting therefore in larger thermal loads [W] acting on the fluid.
Secondly, missing equatorial ports introduce more space for the fluid: in order to avoid too low fluid velocities, the cross-sections of the OB paths have been kept of comparable size with respect to other CVs when possible. It means that to cool a larger area the OB channels are no longer straight, but they create serpentines which turn right and left successively to distribute the borated water, as can be seen in figure 4.20 for CV6 and CV7 respectively, but the same reasoning can be extended to control volume 8 as well.
These multiple direction changes increase the vorticity of the flow, introducing secondary flows and regions of recirculation highlighted in red on the same figure.

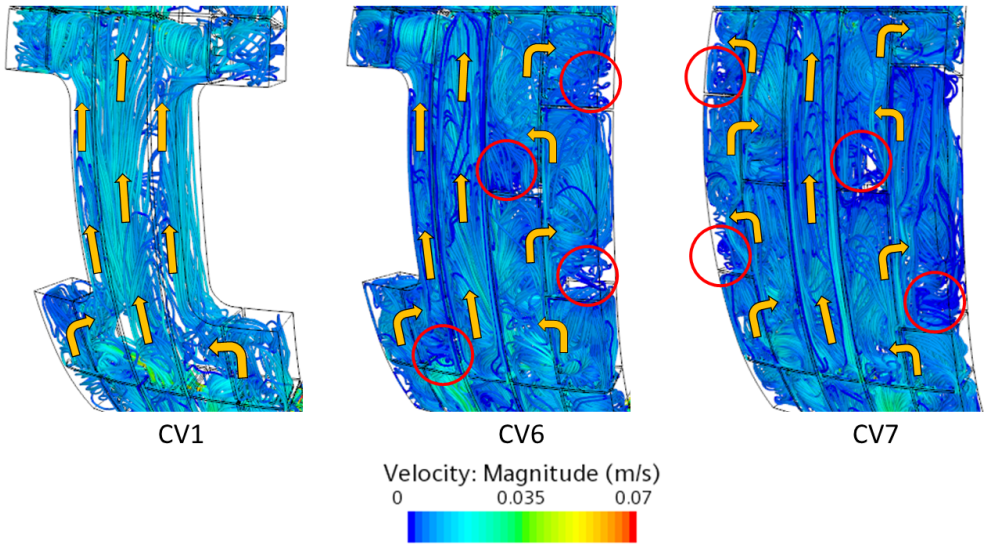

Figure 4.20: Streamlines comparison between CV1, CV6 and CV7 outboard equatorial regions. Macroscopic flow directions in the three OB channels are highlighted with orange arrows, while red circles identifies spots of recirculation/stagnation.

In CV8 and CV9, the presence of skewed ports introduces asymmetries as well in the OB channels. The most relevant aspect though is found on the OB1 path: for CV8 the inclination of port #3 is sufficient to leave a space behind for the connection of upper and lower parts of the control volume. On the contrary, in CV9 the relative inclination between inner wall and port #3 results in a complete disconnection of upper and lower regions, creating two very thin branches, as shown in figure 4.21.
Regarding the little branch at the bottom, this is not a concern because the flow is anyhow able to cool properly this narrow region; in the branch at the top instead, the disconnection introduces a quite severe stagnation region which required deeper investigations. Despite the fact that the CtFD simulation didn't detect any criticalities in terms of minimum temperature at the end, it must be pointed out that the upper branch is for sure a problem for the draining process: in fact, there's no way to remove the borated water in this narrow region from the bottom.

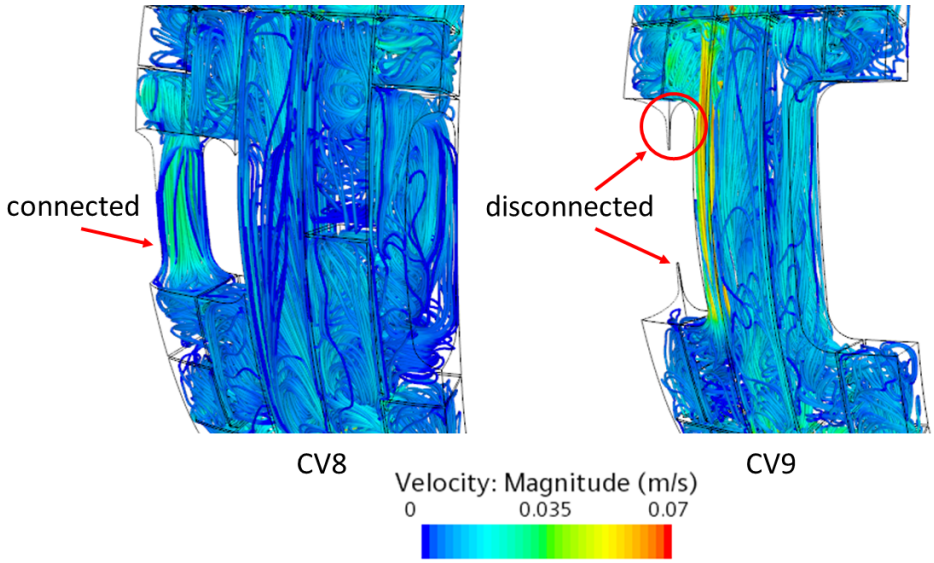

Figure 4.21: Close-up on CV8 and CV9 outboard equatorial regions. In CV9, due to the different relative inclination between port #3 and OB1 channel, the latter is deviated towards OB2, disconnecting upper and lower regions. The red circle highlights the upper fluid volume resulting from the disconnection: borated water will remain trapped here when the CV is drained from the bottom.

Focusing the attention on the thermal-hydraulic results for these four CVs, they are presented in table 4.10, 4.11, 4.12 and 4.13 respectively.
Reported simulation outcomes for CV6, CV7 and CV9 come from unsteady fine simulations, in view of the reports' fluctuations amplitude detected for the steady medium simulations. On the other hand, for CV8 the steady solver coupled with

General Info	
CV	6
CV type	Special
Sectors	S5,6
Hydraulic Sectors	i3
Inlet	L
Fluid Volume [m^3]	0.761
Outer Wall Surface [m^2]	5.89

Results	
Δp [Pa]	2560 ± 95
T_{out} [K]	333.06
T_{max} [K]	333.15
T_{min} [K]	331.76
$\dot{m}_{OB}$ [g s^{-1}]	629 ± 5
$\dot{m}_{IB}$ [g s^{-1}]	481 ± 5

Table 4.10: Relevant geometric and simulation info for CV6. Results are taken from the unsteady fine simulation.

General Info	
CV	7
CV type	Special
Sectors	S6,7
Hydraulic Sectors	i4
Inlet	R
Fluid Volume [m^3]	0.825
Outer Wall Surface [m^2]	6.11

Results	
Δp [Pa]	2561 ± 56
T_{out} [K]	333.05
T_{max} [K]	333.15
T_{min} [K]	332.15
$\dot{m}_{OB}$ [g s^{-1}]	620 ± 3
$\dot{m}_{IB}$ [g s^{-1}]	490 ± 3

Table 4.11: Relevant geometric and simulation info for CV7. Results are taken from the unsteady fine simulation. It is worth mentioning that uncertainties for CV7 are much smaller than CV1 and CV6.

the medium mesh was able to converge to a clean steady-state without considerable numerical fluctuations.
Computed outlet temperatures correctly recover what expected from global energy balances: coherently special CV7 experiences the lowest outlet temperature as a consequence of the larger outer wall surface (6.11 [m^2]).
The swirling paths exploited in CV6 and CV7 to cool larger areas do not have significant influence on the pressure losses.
Different story is found instead for CV9, where the disconnection results in a very narrow OB1 path at the euqatorial level, where fluid velocity increases causing larger pressure drops: for that reason control volume 9 is the one characterized by the largest pressure drop within the NNBI module.
Moreover, in CV9 the disconnection creates an upper region where severe stagnation occurs (fluid velocity of the order of $\approx 10^{-6}$ [$m\,s^{-1}$]) but luckily, in view of its orientation towards the inner side of the control volume, which is not subjected to

General Info	
CV	8
CV type	Special
Sectors	S7,8
Hydraulic Sectors	i4
Inlet	L
Fluid Volume [m³]	0.763
Outer Wall Surface [m²]	5.79

Results	
Δp [Pa]	2608 ± 115
T_{out} [K]	333.06
T_{max} [K]	333.15
T_{min} [K]	330.29
$\dot{m}_{OB}$ [g s^{-1}]	619 ± 20
$\dot{m}_{IB}$ [g s^{-1}]	491 ± 20

Table 4.12: Relevant geometric and simulation info for CV8. Results are taken from the steady medium simulation, coupled with the uncertainties found for CV1 unsteady fine.

General Info	
CV	9
CV type	Special
Sectors	S8,9
Hydraulic Sectors	i5
Inlet	R
Fluid Volume [m³]	0.690
Outer Wall Surface [m²]	5.55

Results	
Δp [Pa]	2928 ± 40
T_{out} [K]	333.06
T_{max} [K]	333.15
T_{min} [K]	331.87
$\dot{m}_{OB}$ [g s^{-1}]	680 ± 4
$\dot{m}_{IB}$ [g s^{-1}]	430 ± 4

Table 4.13: Relevant geometric and simulation info for CV9. Results are taken from the unsteady fine simulation. As can be seen, the severe stagnation in the upper branch doesn't have remarkable effects on final TH results, especially as far as minimum temperature is concerned.

the radiative load from the TS, no issues are found in terms of minimum temperature/formation of cold spots since conduction in the fluid results to be sufficient. This becomes even more true when conduction in the solid will be introduced.
Nevertheless, it must be stressed again that it will for sure represent an issue during the draining process and therefore some design modifications must be discussed in future.
To conclude, always referring to CV9 it is also worth mentioning that the stabilization of the pseudo steady-state during the unsteady fine simulation required a much longer simulated physical time ($\approx$ 10000 [s]) which is not comparable to the time of flight that can be computed knowing the fluid volume and the inlet volumetric flow rate. On top of that, the deviation between average values is also peculiar: as far as the pressure drop is concerned, the steady simulation underestimate the

average value of 2%.
The explanation of these anomalies might be found in the peculiar features of CV9 geometry.

Regarding the coolant distribution, all the four modules share a similar IB/OB balance, in line to what found for regular control volumes.
The repartition between OB and IB channels also follows the trends found for other CVs.
As usual, detailed mass flow rate repartition and temperature/velocity scalar scenes can be found in appendix B for each specific control volume..

4.3.3 CV10-11-12

The VV characterization is concluded by investigating the thermal-hydraulic behaviour of special control volumes CV10, CV11 and CV12. These three control volumes, whose extrapolated geometries are depicted in figure 4.22, are welded together on site via splice plates and act as a glue for the three multi-sectors A-B-C (to be precise, multi-sector C coincides with control volumes CV11 and half of CV10 and CV12).

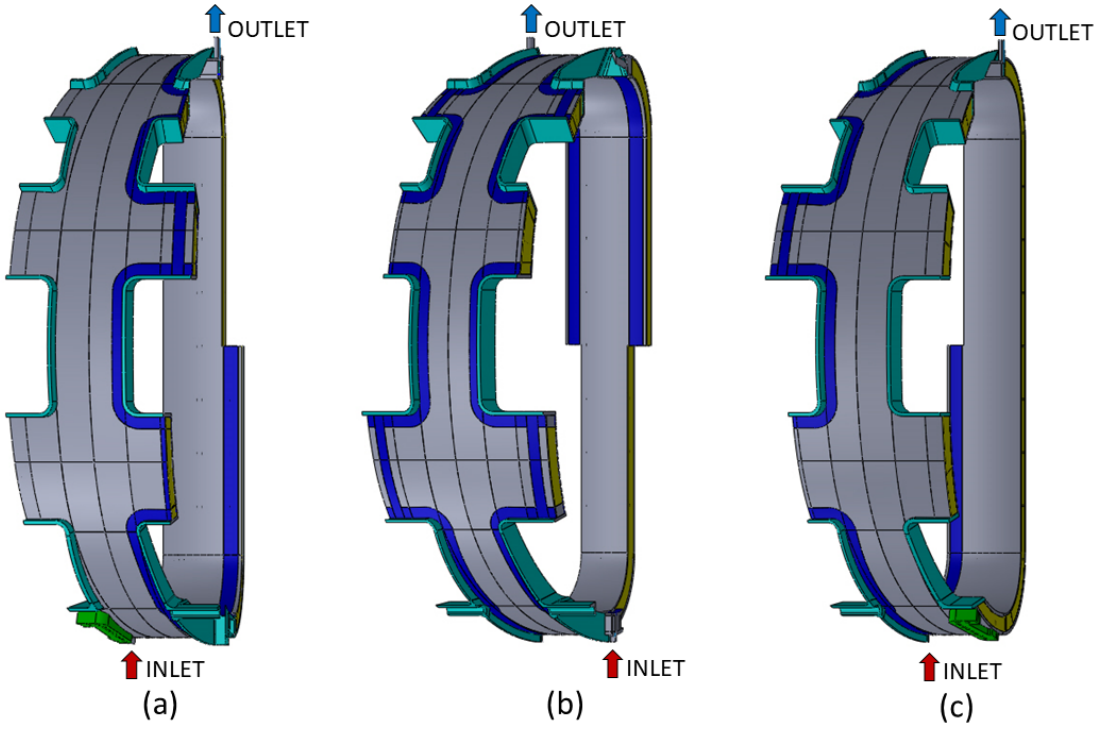

Figure 4.22: (a) CV10-type L, (b) CV11-type R and (c) CV12-type L geometries.

From this picture it can be seen that the topology of these last three control volumes is quite different from previous ones: on the outboard side for instance, the three CVs are no longer hydraulically separated between each other by a straight poloidal cut. Instead, for CV10 and CV12 the branch between ports #2 and #3 has a longer extension towards CV11 than the branches between ports #1/#2 and ports #3/#4. The opposite reasoning can be done for CV11.
Secondly, if the attention is focused on the inboard leg, it can be noticed from figure 4.22 that control volumes CV10 and CV12 present an extension on the lower region while CV11 has two extensions in the upper region. The latter are nothing that additional IB channels which converge into (or -diverge from- if CV11 is considered) the well known three IB paths.
These peculiar geometries will introduce some relevant changes in the coolant distribution that will be discussed in deep in the present section.
In addition to that, as already seen in section 2.2 dedicated to the VV updated design, the different orientation of the poloidal ribs due to the presence of splice frames results in narrower outboard central channels OB2.

As a consequence of their strategic position in the vacuum vessel, CV10 and CV12 will be provided with 8 screwed plugs each (six on OB leg and two on IB leg, see figure 4.23 for details) to carry out the pressurization test of multi-sectors B and A respectively, similarly to what already seen for special CV4.

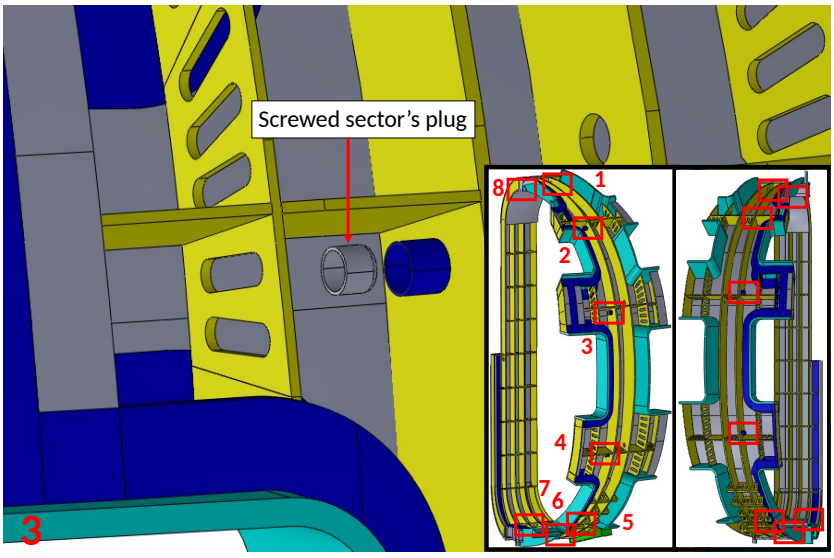

Figure 4.23: CV10 and CV12 screwed plugs. Both control volumes have respectively 8 plugs, six of them located on the outboard leg and the remaining two at the inboard leg. For TH simulations all the plugs have to be removed to let parallel channels to communicate.

Starting from CV10, the outcomes from thermal-hydraulic simulation are presented in table 4.14.

General Info	
CV	10
CV type	Special
Sectors	S9,10-1
Hydraulic Sectors	i5
Inlet	L
Fluid Volume [m^3]	0.688
Outer Wall Surface [m^2]	5.51

Results	
Δp [Pa]	2979 ± 115
T_{out} [K]	333.06
T_{max} [K]	333.15
T_{min} [K]	331.99
$\dot{m}_{OB}$ [g s^{-1}]	700 ± 20
$\dot{m}_{IB}$ [g s^{-1}]	410 ±20

Table 4.14: Relevant geometric and simulation info for CV10. Results are taken from the steady fine simulation coupled with CV1 unsteady fine uncertainties.

As it can be seen in the section dedicated to CV10 in appendix B, the additional inboard channel IB4 is characterized by the lowest mass flow rate (4.5% of the total one), which is coherent because it is located on the opposite side with respect to the inlet.
The pressure drop is more oriented towards the higher values recorded for CV3 or CV5, while no significant issues are found as far as mass flow repartition between IB and OB legs is concerned.
However, CV10 is the only exception because having additional IB channels introduces significant changes in control volumes CV11 and CV12.

Focusing the attention on CV11 for instance, the introduction of additional channels IB0-IB4 at the equatorial level leads to backflow in the upper region of IB1: once the steady-state is reached, approximately 0.5% of the total mass flow rate slowly circulates in IB1 from top to bottom.
This is a quite interesting aspect which has been investigated further as shown in figure 4.24. As can be seen in that figure, the streamlines obtained by integrating backward from the hole H01 (connecting IB0 and IB1 at the outlet region) reveal that little/no fluid passing that hole actually comes from IB1 channel.
In such connection, more than half of the total IB mass flow rate has to be collected and directed towards the outlet pipe: the strong recirculation right before hole H01 creates a "dynamic fluid plug" which hinders the passage of the fluid coming from IB1, which is stopped during its way up to the outlet.
For that reason, once the steady-state is reached, all the fluid circulating in IB1 shifts to IB0 at the equatorial region while a little fraction of the mass flow rate coming from inboard channels IB4, IB3 and IB2 is deflected down to IB1 to then

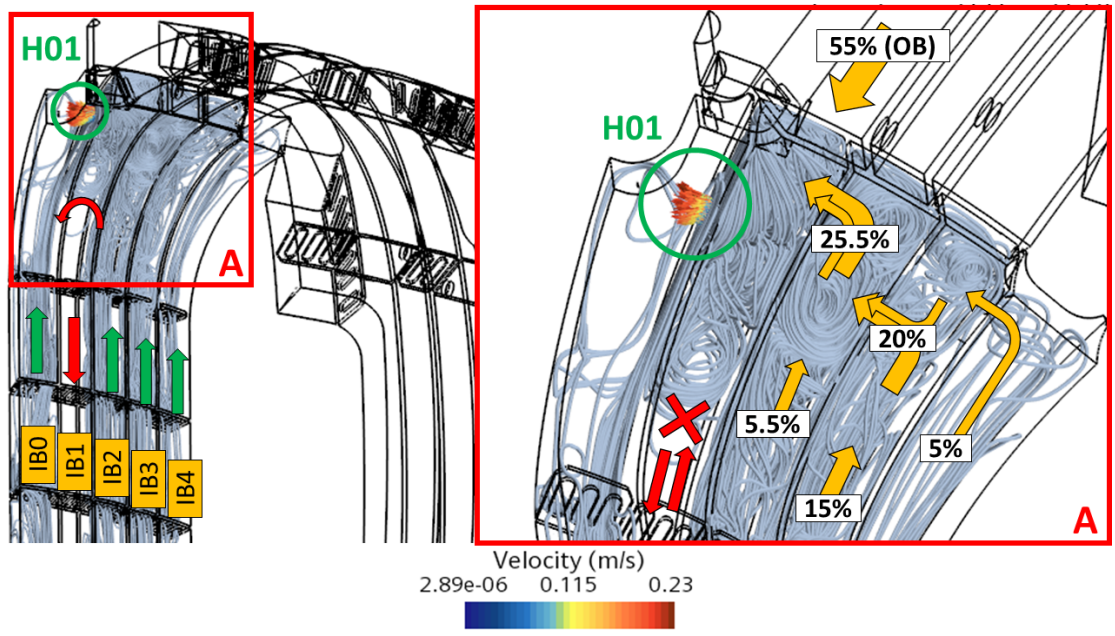

(a)

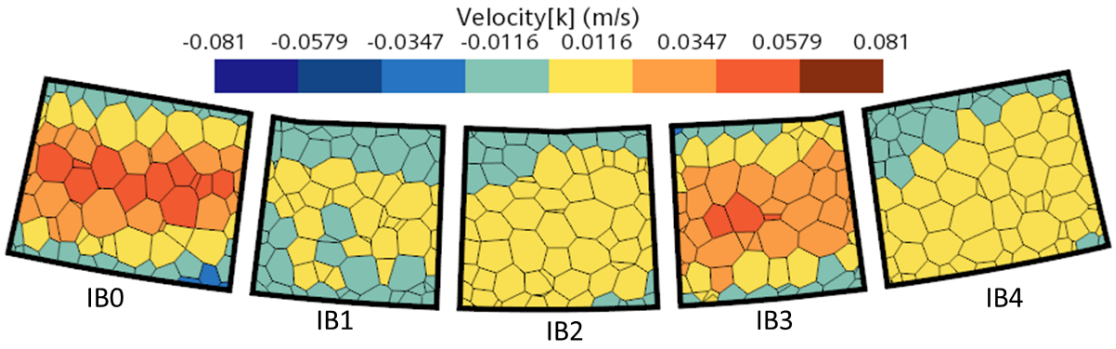

(b)

Figure 4.24: (a) Close-up on CV11 outlet region. The mass flow rate is directed towards the top in all the inboard channels but IB1, where the large fluid recirculation at H01 (the communication hole in the poloidal ribs divinding IB0 and IB1) creates a dynamic fluid plug that hinders the passage of additional mass flow rate. For that reason, 5% of the mass flow rate coming from neighbouring inboard channels is deviated down to IB1 and then exits the domain from IB0. The velocity vectors at H01 provide an idea of the fluid velocity in that region. (b) Scalar scene of the velocity component perpendicular to the four cross-sections of the inboard channels at $z = 1.18$ [m]. In IB1 the fluid is almost stagnant.

reach the outlet from IB0.
That happens because the additional distributed pressure drop related to the passage of the extra mass flow rate $\Delta\dot{m} = 5\%\dot{m}_{tot}$ down to IB1 and then up in IB0 is still lower than the additional localized pressure drop at H01 that would have been occurred if the the same $\Delta\dot{m}$ had passed through the hole. For that reason, the first option is the one preferred by the fluid.
The borated water flowing in IB3 instead prefers to proceed straight at the equatorial intersection: of the 20% of coolant flowing at the bottom of IB3, 15% proceed along IB3 itself while only 5% goes in the additional IB4 channel.
This is coherent because the longer fluid path experienced in IB4 (located further from the outlet) has to be balanced by lower fluid velocity to keep the overall pressure drop inside IB3 and IB4 channels equal (they are parallel connected).
At the end, the fact of having backflow in the upper region of IB1 does not represent an issue in terms of temperature distribution, but it is worth noticing that control volume CV11 is the one characterized by the highest pressure drop among all the CVs that make up the vacuum vessel ($\approx$ 20 [Pa] larger than CV3, so still comparable).
Most relevant TH results are summarized in table 4.15, while in chapter 5 a possible solution that could be investigated to solve the backflow issue is presented.

General Info	
CV	11
CV type	Special
Sectors	S10-2,11-1
Hydraulic Sectors	i6
Inlet	R
Fluid Volume [m^3]	0.670
Outer Wall Surface [m^2]	5.53

Results	
Δp [Pa]	3026 ± 115
T_{out} [K]	333.06
T_{max} [K]	333.15
T_{min} [K]	330.53
$\dot{m}_{OB}$ [g s^{-1}]	615 ± 20
$\dot{m}_{IB}$ [g s^{-1}]	495 ±20

Table 4.15: Relevant geometric and simulation info for CV11. Results are taken from the steady fine simulation coupled with CV1 unsteady fine uncertainties.

To conclude, for CV12 instead the presence of an additional inboard channel at the bottom (IB0) introduces reverse flow in the lower region of IB1.
Differently from CV10, this time the additional inboard channel is located at the same side of the inlet. Since a buttonhole of the inlet chamber directly points toward IB0, the great majority of the coolant flows in it rather than moving to the right and then going up from IB1. At the equatorial level, IB0 mass flow rate (31% of the nominal one) converges into IB1: 22% proceeds going up in IB1, while the remaining 9% flows down to the bottom of IB1 to be then re-distributed between

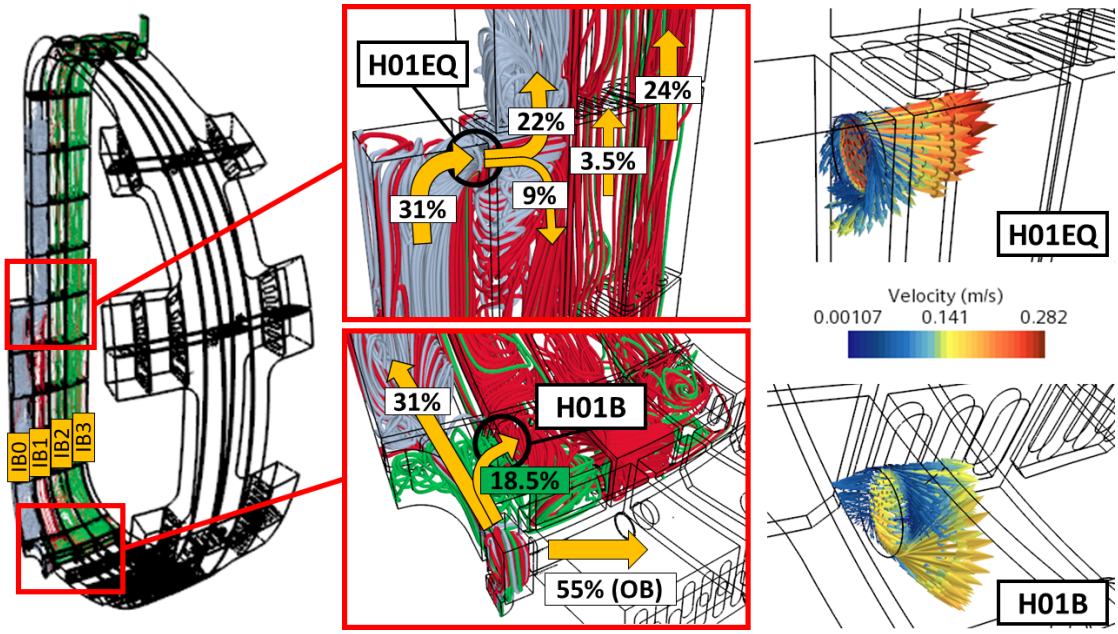

Figure 4.25: Visualization of the peculiar flow distribution in CV12, with a focus on inlet and equatorial regions. Streamlines highlighted in green show the 18.5% of IB mass flow rate flowing in poloidal hole H01B to reach IB2 and IB3 channels, while grey/red streamlines indicate the 31% flowing directly in IB0. After poloidal hole H01EQ, grey streamlines (22%) continue in IB1 towards the outlet while red ones (9%) come back along IB1 to then reach IB2/IB3 channels. Streamlines are evaluated on different grids for sake of visualization and therefore they do not provide quantitative information. Vector velocity fields of poloidal holes H01B and H01EQ are shown as well to give an idea of the velocity magnitude and of the overall flow direction in these two strategic regions. Acting on the diameters of these two can optimze the flow distribution avoinding backflow.

IB2 and IB3 channels.
A visualization of the flow is presented in figure 4.25, while in figure 4.26 the V_s scalar scene of the IB bottom region is available.
Despite the backflow at the bottom of IB1, the TH results, shown in table 4.16, confirms that also for CV12 no relevant issues are found in terms of pressure drop, minimum temperature and overall flow repartition between IB/OB branches.
As for all the other CVs, scalar scenes and detailed flow repartition tables are made available in appendix B.

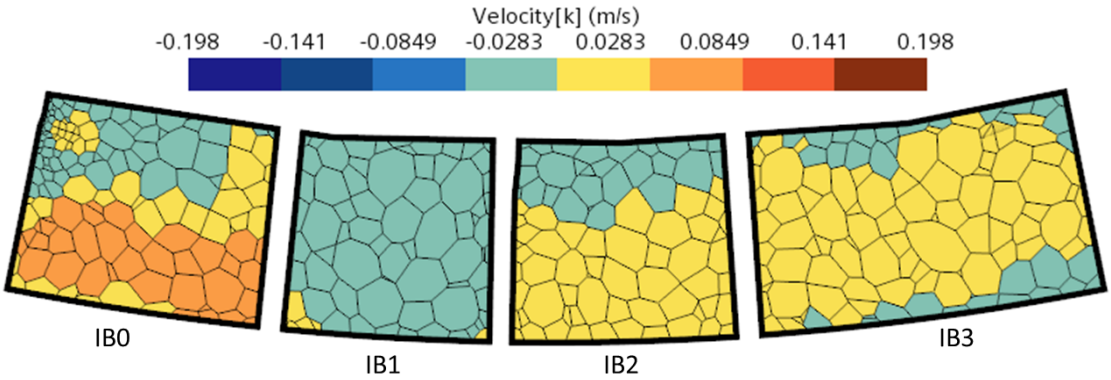

Figure 4.26: V_s scalar scene at the $z = -1.34$ [m] inboard cross-section.

General Info	
CV	12
CV type	Special
Sectors	S11-2,12
Hydraulic Sectors	i6
Inlet	L
Fluid Volume [m^3]	0.687
Outer Wall Surface [m^2]	5.40

Results	
Δp [Pa]	2699 ± 115
T_{out} [K]	333.06
T_{max} [K]	333.15
T_{min} [K]	331.75
$\dot{m}_{OB}$ [g s^{-1}]	560 ± 20
$\dot{m}_{IB}$ [g s^{-1}]	550 ±20

Table 4.16: Relevant geometric and simulation info for CV12. Results are taken from the steady fine simulation coupled with CV1 unsteady fine uncertainties.

4.4 System-level Modelling with OpenModelica

In the previous sections, the TH numerical results for regular and special control volumes have been presented and discussed, with an additional focus on the most relevant flow peculiarities.
These results are recovered from 3D simulations that, as discussed in section 4.1.4, are quite computational expensive.
Since the CtFD simulation of the entire vacuum vessel might be prohibitive, in order to reconstruct its global hydraulic behaviour from what's already available for each CV, the method of the hydraulic characteristic presented in section 4.1.6 has been introduced to approximate firstly the minor losses of CV1 in off-nominal conditions.
Once the quadratic approximation has been demonstrated to be sufficiently precise within $\pm 10\%$ of the nominal mass flow rate, the couples $\Delta p, \dot{m}_{nominal}$ obtained from 3D CtFD analyses have been exploited to extend the same reasoning to the other regular and special control volumes.
In fact, when all the hydraulic behaviours of the components are known, then they can be connected together in parallel (as it actually happen in the VV) recreating the full hydraulic circuit from which the common working pressure drop and the working mass flow rate repartition can be obtained. The overall mixing temperature can be recovered as well starting from the energy balance on each single CV.
In figure 4.27, all the CVs' measured pressure drops are compared taking into account the relative uncertainties, and for the case of CV1 only, of the most important simulation choices discussed in previous sections. As already pointed out, the relative difference between CVs' computed pressure drops is quite limited and, as can be seen in figure 4.28, the resulting quadratic approximations are very similar between each other.

As the title of this section suggests, the full hydraulic model of the DTT Vacuum Vessel has been derived exploiting the open-source software *OpenModelica* based on the Modelica language, an a-causual object-oriented language particularly indicated for the modelling of complex dynamic systems.
Without going to much in details, it is worth mentioning that by exploiting the objects already available in libraries such as the Modelica Standard Library or the ThermoPower Library, complex systems can be built by connecting between each other primitive entities picked up from these libraries.
For instance, in the present work each control volume has been characterized by adopting the 1D fluid flow model[2] (see figure 4.28) coupled with a friction factor

[2]Flow1DFV from ThermoPower open library

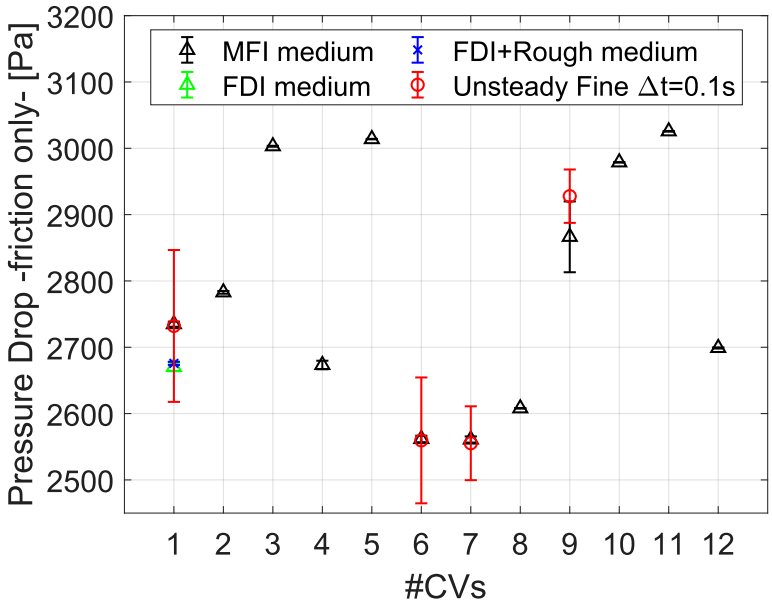

Figure 4.27: Pressure losses at nominal mass flow rate (1.11 [kg s^{-1}]) computed from CtFD simulations for the 12 different CVs. MFI stands for "*Mass Flow Inlet*" while FDI stands for "*Fully Developed Inlet*".

specification of "*OpPoint*" type.
The latter automatically retrieve the hydraulic characteristic (quadratic) of the object once a single operating point ($\Delta p, \dot{m}_{nominal}$ couple) is specified, exactly as explained in section 4.1.6.
As far as the thermal point of view is concerned, the energy balance on each CV can be retrieved by imposing the specific heat flow on the thermal connector of the fluid flow model (highlighted in orange in figure 4.28) and by selecting the "*Ideal Heat Transfer*" function which consider an infinite heat transfer coefficient ($\Delta T = 0$ across the boundary layer). Within each Flow1DFV parameters window then the heat transfer surface is specified according to the computed outer wall surface (fluid side) from TH simulations.
Together with the 18 different objects characterizing the CVs of the vacuum vessel, mass flow source (Mtot) and pressure sink (Pout) objects are introduced to close the system of equations, prescribing thus the total mass flow rate of 20 [kg s^{-1}] and a pressure reference to have the overall problem well-posed.
With Constant Source Blocks and a Heat Source connectors the TS radiative thermal load is prescribed in each object's thermal interface.
The full model of the Vacuum Vessel is presented in figure 4.29.
In the complete model the 9 staggered inlets and outlets have not been introduced: it must be stressed that, since no info on distribution and collector rings are

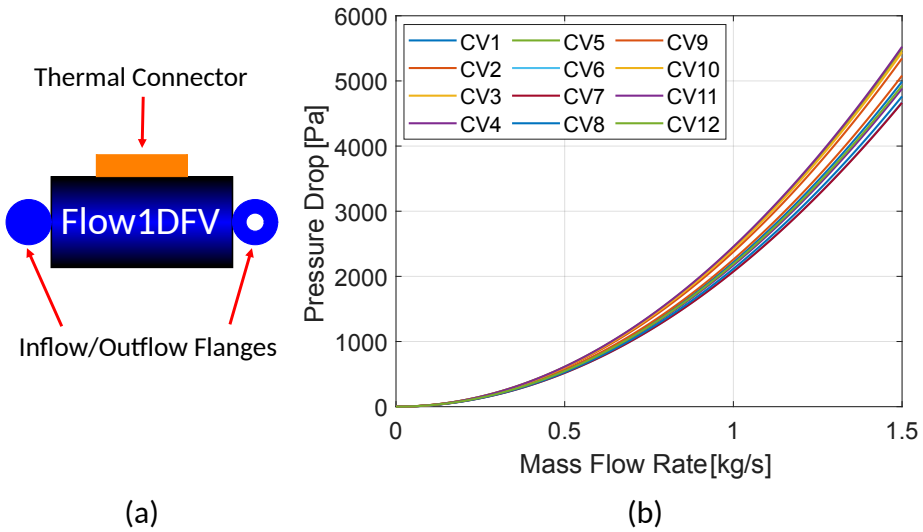

Figure 4.28: (a) Flow1DFV object from ThermoPower library. (b) Interpolated quadratic hydraulic characteristics for all the simulated CVs.

available, the inlet and outlet differentiation is useless from a physical point. All the CVs results to be simply connected in parallel between unique common inlet and outlet.

The results are presented in table 4.17.
Again, it is important to stress that the Modelica full model is more beautiful than useful: the outlet mixing temperature can be simply obtained from the first law of thermodynamics by considering the whole vacuum vessel irradiated external surface of 101 [m^2] and the total mass flow rate of borated water, as:

$$T_{mix} = 333.15\ \text{K} - \frac{70\ \text{W}\,\text{m}^{-2} \cdot 101\ \text{m}^2}{20\ \text{kg}\,\text{s}^{-1} \cdot 4019.68\ \text{J}\,\text{kg}^{-1}\,\text{K}^{-1}} = 333.062\ \text{K}$$

while the mass flow repartition can be also obtained by iteratively solving the resulting non linear system of equations.
However, with the Modelica model each parameter can be modified and/or tuned to assess the effect on the final results without performing every time the computation by hand. For instance, by knowing the desired outlet temperature it can be assessed how the new computed total mass flow rate is split between the different control volumes.

Variable	Value
Δp_{VV} [Pa]	2806.7
$\dot{m}_{CV1}$ [kg s^{-1}]	1.125
$\dot{m}_{CV2}$ [kg s^{-1}]	1.115
$\dot{m}_{CV3}$ [kg s^{-1}]	1.073
$\dot{m}_{CV4}$ [kg s^{-1}]	1.137
$\dot{m}_{CV5}$ [kg s^{-1}]	1.071
$\dot{m}_{CV6}$ [kg s^{-1}]	1.162
$\dot{m}_{CV7}$ [kg s^{-1}]	1.163
$\dot{m}_{CV8}$ [kg s^{-1}]	1.152
$\dot{m}_{CV9}$ [kg s^{-1}]	1.087
$\dot{m}_{CV10}$ [kg s^{-1}]	1.078
$\dot{m}_{CV11}$ [kg s^{-1}]	1.069
$\dot{m}_{CV12}$ [kg s^{-1}]	1.132
T_{mix} [K]	333.062

Regular Special Global

Table 4.17: Outcomes from the VV system-level model.

To conclude, it must be pointed out that the results obtained with the current Modelica model are only *indicative* since they don't take into account the intrinsic transient nature of the solution due to variable pressure drops detected for CV1, CV6, CV7 and CV9. In order to properly account for the unsteadiness as well, a 3D unsteady CtFD simulation of the entire vacuum vessel is the only option.
Moreover, the resulting outlet temperature still differs from the computed one (of ≈ 0.01 [K]) because of uncorrect material properties characterization: in the current model thermo-physical properties of standard water are exploited instead of the one computed for borated water in chapter 3.
To correctly retrieve the real outlet mixing temperature, an ad hoc Modelica media library must be developed in future.

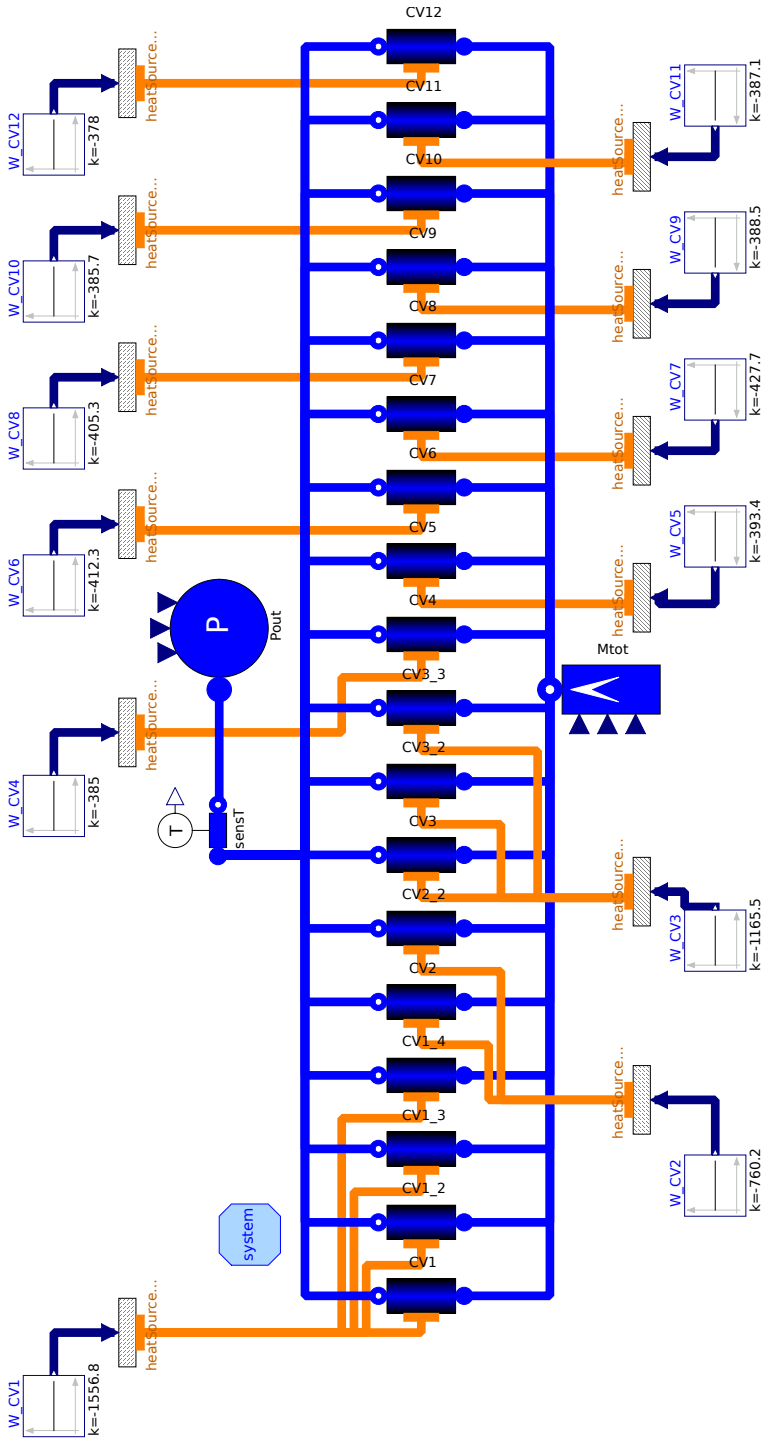

Figure 4.29: Complete system-level model of the DTT Vacumm Vessel.

Chapter 5

Conclusions and Perspective

"Physics is like sex: sure, it may give some practical results, but that's not why we do it"
Richard P. Feynman

In this last concluding chapter, the most relevant results found from numerical simulations are summarized in a compact way, to provide a picture of the DTT vacuum vessel thermal hydraulic behaviour.
To summarize at maximum, all the control volumes satisfy design requirements DS1 and DS2 (maximum and minimum temperature constraints) while for DS3 (full drainability) only CV9 does not fully comply with it.
For control volumes CV4, CV11 and CV12 optimizations are suggested (see high-level priorities below for clarifications).
The 3000+ hours of simulations carried out in this work reveal at the end that common aspects and peculiarities can be found:

- Common aspects:
  - The pressure drop of each control volume, being it "*Special*" or "*Regular*", is within the range $2561 \div 3026$ [Pa].
  - The mass flow rate repartition between inboard and outboard legs is shifted toward the latter ($58\% \div 42\%$ average proportion), which is coherent since OB channels are characterized by larger cross-sections.
  - The mass flow repartition within the outboard leg is characterized by larger coolant flow in the OB channel closer to the inlet at the bottom, which progressively shifts to the opposite side when approaching the outlet at the top, where the maximum mass flow rate is instead detected at the OB channel opposite to the inlet (inlet and outlet are staggered).

  - The mass flow repartition within the inboard leg is characterized by almost equal coolant flow in lateral channels IB1-IB3 ($\approx 20\%$ of total mass flow rate), while only $\approx 3 \div 4\%$ of the borated water flows in the central channel IB2, characterized by a smaller cross-section.
  - Variations in CVs outer surfaces have a negligible impact on the energy balance: the average temperature difference between inlet and outlet is $\Delta T = 0.09$, with deviations between different CVs of the order of [mK].

- Peculiar aspects:
  - In view of the fluid domain complexity, the steady solver is not always able to find a clean steady-state and unsteady simulations on finer meshes are needed to correctly capture all the fluid flow peculiarities. However, the latter have little/no impact on relevant quantities such as pressure drop and mass flow rate distribution.
  - The splice plate foreseen in CV4 introduces toroidal ribs in OB2 and IB2 channels with only two button-holes rather than three. The additional resistance lead to lower coolant mass flow rate, that in IB2 reaches a minimum value of only 1.5% of the total mass flow rate.
  - The relative inclination between skewed equatorial port and inner wall in CV9 creates sharp disconnections between OB1 lower and upper regions. Despite the strong stagnation, they do not represent an issue in terms of temperature distribution. The upper one however will hinder the complete draining of CV9 for baking purposes. Moreover, average values returned from steady and unsteady simulations have 2% relative deviation, which is larger than the 1.2% found for CV1, CV6 and CV7.
  - Peculiar inboard channels topologies in CV11 and CV12 introduces back-flow in portions of the the inboard channels. Even if TH analyses didn't spot any relevant issue related to that, simple modifications of the diameters of the holes for the toroidal flow should reduce/solve it.

Of course, results listed above have to be considered as the starting point for something else, and not a sterile blind spot.
In the following lines, a series of suggested insights and upgrades on the existing model are presented, together with some suggestions on possible future works based on their priority level.

- High-level priorities:
  - Modelling
    1. Extend the fine unsteady simulation to all the remaining CVs to detect if there are other average values relevant deviations (with respect to the medium steady results).
    2. Model the conjugate heat transfer by introducing the solid domain (with its own thermo-physical properties) as well: even if overall effects are expected to be negligible, it will allow to have at disposal a fully representative model of the control volume (knowing the temperature distribution in the solid could help/speed-up future thermo-mechanical analyses for instance).
    3. Introduce and model all the thermal loads acting on the VV, namely the one coming from the divertor and the neutronic volumetric generation. The latter are pulsed and therefore will claim for unsteady simulations.
  - Design:
    1. Optimize CV4, CV9, CV11 and CV12 geometries to reduce/eliminate the spotted criticalities, keeping in mind the integration constraints (e.g structural ones). In CV4 an additional button-hole can be added on IB2/OB2 toroidal ribs to better balance the mass flow rate in these channels; in CV9 the upper disconnection can be filled with solid to satisfy the full drainability constraint; in CV11 and CV12 holes for the toroidal flow can be widened or narrowed in order to tune the hydraulic resistance of each channel to better distribute the borated water avoiding stagnation/backflow.

- Mid-level priorities:
  1. Include in the model the physics related to the neutronic capture by ^{10}B isotopes. Even if detected stagnation/recirculation regions do not represent an issue in terms of temperature distribution, from the neutronic shield point of view these regions can represent a weakness.

2. Perfom a 3D, unsteady CtFD simulation of the entire VV to study separately the effect of outlet and inlet coupling by imposing target mass flow-rate boundary conditions at the outlet. With a fine mesh, the number of cells will be of the order of 400 million.

- Low-level priorities:

1. Implement advanced optimization strategies (e.g topology optimization) to reengineer the inlet/outlet distribution chambers so that to minimize pressure drops while guaranteeing the fairest borated water distribution between OB/IB legs. It must be stressed that the complex resulting geometries could be however impossible to be manufactured/integrated.
2. Develop the borated water Modelica Media library exploiting correlations reported in 3.10 to correctly retrieve outlet mixing temperature.

Appendix A

Accounting for Temperature in the Turbulent Boundary Layer

A.1 Turbulent Prandtl Number Derivation

If the turbulent flow involves also heat transfer, as the case for the present Master Thesis, then an universal law of the wall can be derived also for the temperature. In laminar regimes, the Prandtl number strongly dictates the relative growth of velocity and temperature boundary layers, according to the well known proportion:

$$\frac{\delta}{\delta_t} \approx \mathrm{Pr}^n$$

Being n positive, it is clear that for gases (Pr≈ 1) thermal and velocity boundary layers will have comparable thickness while for liquid metals for instance (Pr$<< 1$) the thermal boundary layer will be much larger then the velocity one because the energy diffusion greatly exceeds momentum diffusion.
However this approximative ratio holds until the smooth and soft transport by diffusion is overshadowed by the brutal and chaotic turbulent mixing.
By conceptually replacing the role of the kinematic viscosity with the thermal diffusivity $\Gamma = \frac{\lambda}{\rho c}$ it can be said that the wall layer of the temperature field is the region where the effect of Γ is more relevant (diffusion predominates). However thermal and flow wall layers are coupled, and the former has universal properties only if it lays within the latter, namely for Prandtl number $\mathrm{Pr} = \frac{\nu}{\Gamma} > 0.5$, condition which is verified when considering the thermophysical properties of borated water:

$$\mathrm{Pr} = \frac{5.8613 \cdot 10^{-4} \cdot 4019.68}{0.6967} \approx 3.4$$

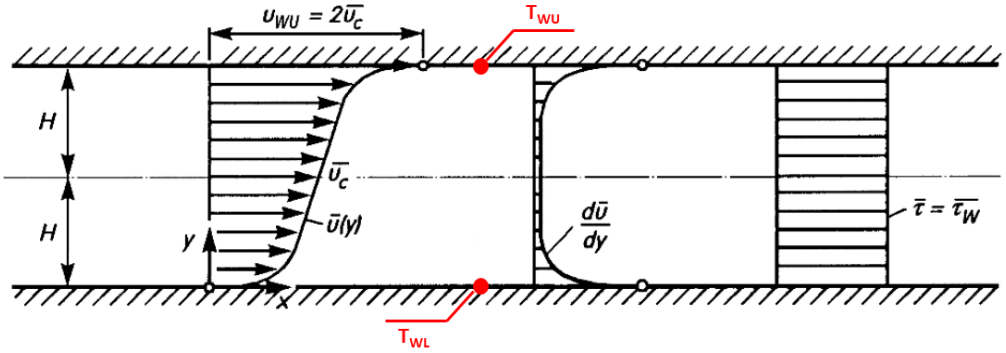

Figure A.1: Schematic representation of the bi-dimensional *Couette* flow between two parallel plates. The original image is taken from [32]

To give a little bit of context, the simple, but representative, bidimensional case of turbulent *Couette* flow between two plates spaced $2H$ and kept at different temperatures shown in figure A.1 is considered to develop the definition of the turbulent Prandtl number, following mainly the treatment done by Hermann Schlichting in its "*Boundary layer theory*" [32].
The Couette flow is a confined pure shear flow where an upper plate is moved horizontally with respect to the lower plate at constant velocity. The velocity of the upper plate u_{WU} is twice the velocity of the flow at the center line $y = H$.
The final goal is to find a relation to describe the temperature $\overline{T}$ and the velocity $\overline{u}$ profiles in proximity of the wall as a function of geometric and fluid properties. To do that, the friction temperature is defined starting from the definition of the wall friction velocity $u_\tau = \sqrt{\frac{\overline{\tau_\nu} + \tau_t}{\rho}}$:

$$T_\tau = -\frac{\overline{q_\lambda} + q_t}{\rho c u_\tau}$$

with:

- $\overline{q_\lambda} = -\lambda \frac{\partial \overline{T}}{\partial y}$ the diffusive heat flux along y-direction
- $q_t = \rho c \overline{T'v'}$ the heat flux related to turbulent mixing along y-direction (viscous dissipation is neglected for simplicity, and for incompressible flow it is also a reasonable assumption)
- $\overline{\tau_\nu} = \rho \nu \frac{d\overline{u}}{dy}$ and $\tau_t = -\rho \overline{u'v'}$ the mean viscous shear stress (molecular momentum transfer due to fluid viscosity) and the turbulent shear stress (momentum transfer due to turbulent fluctuations) respectively.

The balance of forces in the fluid $\overline{\tau_w} = \overline{\tau_\nu} + \tau_t = const$ is nothing but the force per unit area necessary to move the upper plate at constant velocity u_{WU}, while $\overline{q_w} = \overline{q_\lambda} + q_t$ is the total heat flux in the wall layer, assumed constant because the two plates are kept at constant temperature and the flow is fully developed (i.e steady in the mean flow quantities).
For sake of clarity $\overline{q_w}$ is nothing but one of the components of the most general vector $\overline{\mathbf{q}}''$ appearing in the energy equation solved by *Star-CCM+*.
Further manipulations, which involve the introduction of dimensionless quantities such as:

$$\eta = \frac{y}{H},\ u^+ = \frac{\bar{u}}{u_\tau},\ Re_\tau = \frac{u_\tau H}{\nu},\ \tau_t^+ = \frac{\tau_t}{\rho u_\tau^2}$$

allow to find a partial differential equation for the dimensionless velocity u^+ from the balance of forces in the fluid:

$$\frac{1}{Re_\tau}\frac{du^+}{d\eta} + \tau_t^+ = 1$$
$$\eta = 0 :\ u^+ = 0,\ \tau_t^+ = 0$$
$$\eta = 1 :\ \frac{d^2u^+}{d\eta^2} = 0$$

The second boundary condition states that at the center line $y = H$ the velocity profile changes concavity: for $y < H$ the tangential velocity has to nullify to match the no-slip condition at the wall while for $y > H$ fluid velocity has to match the upper plate velocity for the same principle.
However the problem above is not closed since only one equation is available for two unknows (u^+, τ_t^+), and again it is exactly here where a turbulence model is needed.
If the attention is focused on the region close to the wall, the wall layer, it is possible to derive its thickness from two characteristic quantities ν and u_τ:

$$\delta_\nu = \frac{\nu}{u_\tau} = \frac{H}{Re_\tau}$$

from this consideration it is possible to derive the expression of the dimensionless coordinate y^+ already introduced in chapter 3:

$$y^+ = \frac{y}{H}Re_\tau = \eta Re_\tau$$

As far as temperature is concerned instead, in the wall layer it is possible to define a dimensionless temperature and heat flux:

$$\Theta^+ = \frac{\overline{T} - T_{WL}}{T_\tau},\ q_t^+ = \frac{q_t}{\overline{q_w}}$$

From these previous considerations, the force per unit area and heat flux balances in the wall layer, or boundary layer, become:

$$\overline{\tau_w} = \overline{\tau_\nu} + \tau_t \rightarrow \frac{du^+}{dy^+} + \tau_t^+ = 1,\ y^+ = 0:\ \frac{du^+}{dy^+} = 1$$
$$\overline{q_w} = \overline{q_\lambda} + q_t \rightarrow \frac{1}{\mathrm{Pr}}\frac{d\Theta^+}{dy^+} + q_t^+ = 1,\ y^+ = 0:\ q_t^+ = 0$$

In analogy to what done in the Boussinesq assumption, the heat flux related to turbulent transport can be written introducing a turbulent conductivity λ_t and in turn a turbulent thermal diffusivity Γ_t:

$$q_t = \rho c\overline{T'v'} = -\lambda_t\frac{\partial\overline{T}}{\partial y} = -\rho c\Gamma_t\frac{\partial\overline{T}}{\partial y}$$

It is important to stress that this assumption is again a simplification and when buoyancy forces are dominant it is known to be inaccurate.
For sake of completeness, Kenjere et al.[33] derived an algebraic formulation of the turbulent heat flux to provide a remedy for bad performances of the Boussinesq assumption. This formulation can be activated in *Star-CCM+* by selecting the "*Temperature Flux Model*", but it requires low-Reynolds number approach.
Back to the main topic, the definition of the Turbulent Prandtl number Pr_t is derived:

$$\mathrm{Pr}_t = \frac{\mu_t}{\rho\Gamma_t} = -\frac{\tau_t\rho c\left(\frac{\partial\overline{T}}{\partial y}\right)}{q_t\left(\frac{\partial\overline{u}}{\partial y}\right)} \tag{A.1}$$

The velocity profile in the wall layer of the flow should match up the one of the core layer, dominated by turbulent momentum transport, as $y^+ \rightarrow \infty$. In the so-called overlap layer, the velocity profile is neither dependent by H or ν, and a dimensional analysis with the Buckingham theorem leads to:

$$\hat{y}\frac{du^+}{d\hat{y}} = \frac{1}{\kappa}$$

where $\hat{y}$ is an intermediate coordinate for the overlap layer:

$$\begin{cases}\hat{y} = \eta, & \text{core layer}\\ \hat{y} = y^+, & \text{wall layer}\end{cases}$$

Therefore two matching conditions must be verified:

$$\lim_{\eta\rightarrow 0}\frac{du^+}{d\eta} = \frac{1}{\kappa\eta},\ \text{core layer}$$
$$\lim_{y^+\rightarrow\infty}\frac{du^+}{dy^+} = \frac{1}{\kappa y^+},\ \text{wall layer}$$

If the same matching process is made also for the temperature distribution in the core and wall layers, the matching conditions for the wall layer can be integrated approaching the core of the flow ($y^+ \to \infty$) resulting in nothing but two well known logarithmic laws:

$$\lim_{y^+\to\infty} u^+\left(y^+\right) = \frac{1}{\kappa}\ln y^+ + C^+ \tag{A.2}$$

$$\lim_{y^+\to\infty} \Theta^+\left(y^+, \mathrm{Pr}\right) = \frac{1}{\kappa_\theta}\ln y^+ + C_\theta^+(\mathrm{Pr}) \tag{A.3}$$

Relation A.2, known as the logarithmic law of the wall, has already been discussed even if the form is slightly different from the one implemented in *Star-CCM+* (see eq. 3.70). The constant of integration C^+ depends on the characteristics of the surface and for smooth walls experimental evidences show that $C^+ = 5.0$.
Relation A.3 instead indicates the dependence of the dimensionless temperature Θ^+ as a function of the dimensionless coordinate y^+ and of the Prandtl number, which affects the value of the constant of integration C_θ^+. The dependence $C_\theta^+(\mathrm{Pr})$ can be approximated well by the following relation:

$$C_\theta^+\left(\mathrm{Pr}\right) = 13.7 \cdot \mathrm{Pr}^{\frac{2}{3}} - 7.5 \ \left(\mathrm{Pr} > 0.5\right) \tag{A.4}$$

while the value $\kappa_\theta = 0.47$ has been derived in [34], insights of which are far beyond the scope of the present work.
Moreover, it must be stressed that the previous logarithmic relations are valid in the overlap layer only but they have universal character since no turbulence model have been involved, exploiting solely dimensional analysis and the two-layer concept (wall layer-core layer).
If dimensional analysis reminds the reader of science-fictions-like telenovelas, it is of interest to see that M. Oberlack [35] succeed in deriving the logarithmic law of the wall directly from Navier-Stokes' equations. Again, details are left to the reader curiosity.
Exploiting the matching conditions in the definition of eddy diffusivity and turbulent thermal diffusivity when the viscous sub-layer is approached leads to the following results:

$$\lim_{y\to 0} \nu_t = \kappa u_\tau y; \ \lim_{y\to 0} \Gamma_t = \kappa_\theta u_\tau y$$

then from these two it derives that in the wall layer the turbulent Prandtl results to be equal to:

$$\mathrm{Pr}_t = \frac{\kappa}{\kappa_\theta} = \frac{0.42}{0.47} \approx 0.9 \tag{A.5}$$

For value of the Prandtl number greater than 0.5, this value of Pr_t is typically extended for the entire fully turbulent outer layer.

When the assumption $\kappa = \kappa_\theta$ holds, the turbulent Prandtl number is equal to one, condition known as the *Reynolds Analogy*. The latter however has been proven to be invalid for Prandtl number far from unity.
From a practical point of view therefore, for the thermal-fluid dynamics simulations the default *Star-CCM+* value of $\mathrm{Pr}_t = 0.9$ has been kept.

A.2 Temperature Wall Functions

In CFD codes, wall functions for temperatures such as equation A.3 are exploited to provide a correct estimation of the wall heat flux $\overline{q_w}$ avoiding the use of very thin cells near the wall (i.e *high* y^+ treatment).
From DNS/experimental data, standard wall functions are obtained to approximate the temperature profile (in terms of dimensionless temperature T^+) in the viscous sublayer and in the log layer respectively:

- Viscous sub-layer $y^+ < 5$:

$$T^+ = \mathrm{Pr}\, y^+ \tag{A.6}$$

- Log layer $30 < y^+ < 200$:

$$T^+ = \mathrm{Pr}_t \left(\frac{1}{\kappa} \ln\left(E y^+\right) + P \right) \tag{A.7}$$

where the empirical function P by Jayatilleke [36] shifts the logarithmic profile up and down based on the Prandtl number of the fluid:

$$P = 9.24 \left[\left(\frac{\mathrm{Pr}}{\mathrm{Pr}_t} \right)^{\frac{3}{4}} - 1 \right] \left[1 + 0.28 e^{\left(-0.007 \left(\frac{\mathrm{Pr}}{\mathrm{Pr}_t} \right) \right)} \right] \tag{A.8}$$

As for momentum wall functions, a blended approaches have been proposed as well to approximate both regions with an unique function, with the additional desire to better represent the profile in the buffer layer.
In *Star-CCM+*, the approach derived by Kader B.A.[37] is implemented:

$$T^+ = e^{-f_\Gamma} \mathrm{Pr} y^+ + e^{\left(-\frac{1}{f_\Gamma} \right)} \mathrm{Pr}_t \left[\frac{1}{\kappa} \ln\left(E y^+\right) + P \right] \tag{A.9}$$

$$f_\Gamma = \frac{0.01 c \left(\mathrm{Pr} y^+\right)^4}{1 + \frac{5}{c} \mathrm{Pr}^3 y^+} \tag{A.10}$$

$$c = \frac{e^{f_r}}{e} \tag{A.11}$$

In fig.A.2 the standard and blended approaches are shown for two different Prandtl

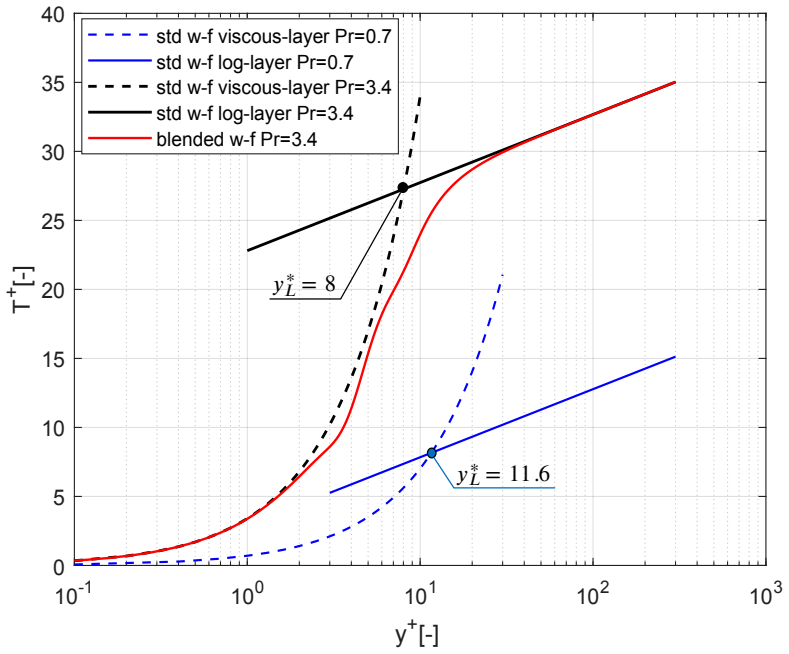

Figure A.2: Comparison between standard wall functions (std w-f) for dimensionless temperature with Pr = 0.7 (air) and Pr = 3.4 (borated water). For borated water, the red curve shows the blended approach. The intercepting points are indicated as well to quantify the effect of the Prandtl number.

numbers, comparing air and borated water at 60°C and 4 [bar]. At first, it can be noticed that, qualitatively, the shape of the T^+ profile is very similar to the one of the velocity, but as already seen before during the Turbulent Prandtl number derivation from the Couette flow, the Prandtl number plays a major role in determining the shape and the thickness of the thermal boundary layer.
More specifically, it modifies the position of the intercepting point y_L^* between viscous and log layer profiles. For air, the viscous layer is more thicker than borated water ones.
A correct estimation of the intercepting point is crucial because again the CFD code doesn't directly exploit wall functions to prescribe the temperature profile; instead it exploits them to correctly approximate the heat flux at the wall by properly tuning the thermal diffusivity $\overline{\Gamma_w}$ from the Fourier's law:

$$\overline{\Gamma_w} = \Gamma_\lambda + \Gamma_t = \begin{cases} \Gamma_\lambda; & \text{if } y^+ \leq y_L^* \\ \frac{u_\tau y_p}{\mathrm{Pr}_t\left(\frac{1}{\kappa}\ln(Ey^+)+P\right)}; & \text{if } y^+ \geq y_L^* \end{cases} \tag{A.12}$$

Being $\Gamma_\lambda = \frac{\lambda}{\rho c}$ the molecular thermal diffusivity.

The workflow of the CFD code is therefore the following:

1. Computes y^+ and Pr of each near wall cell
2. Derives from standard wall functions the intercepting point y_L^*
3. With the if-statement A.12, it corrects the thermal diffusivity at the wall to ensure:
$$\overline{q_w}_{viscous} = \overline{q_w}_{log} = \overline{q_w} = \rho c \overline{\Gamma_w} \left(\frac{T_w - T_p}{y_p} \right) \tag{A.13}$$
being T_p the temperature at the centroid y_p of the cell closest to the wall.

In the case under investigation, all boundaries are adiabatic but the outer wall where the heat flux is prescribed. In this case, eq. A.13 is simply re-arranged to compute correctly the temperature at the wall.
To conclude, it has been derived that for pure water (Pr = 3 at 60°C and 4 [bar]) the interception between viscous and log layers happens at $y_L^* = 8.3$ instead of $y_L^* = 8$. It can be stated therefore that, as far as temperature wall functions application is concerned, the effect of boron could be easily neglected.

Appendix B

Mass Flow Rate Distribution Tables and Temperature/Reverse Flow Scalar Scenes

In this appendix, additional scenes and tables are made available to check, for control volumes from two to 12, the:

- 3D Temperature distribution in the computational domain.
- Mass flow rate repartition in each IB/OB channel.
- V_s distribution in the 18 cross-sections exploited for the backflow evaluation.

B.1 CV2-L

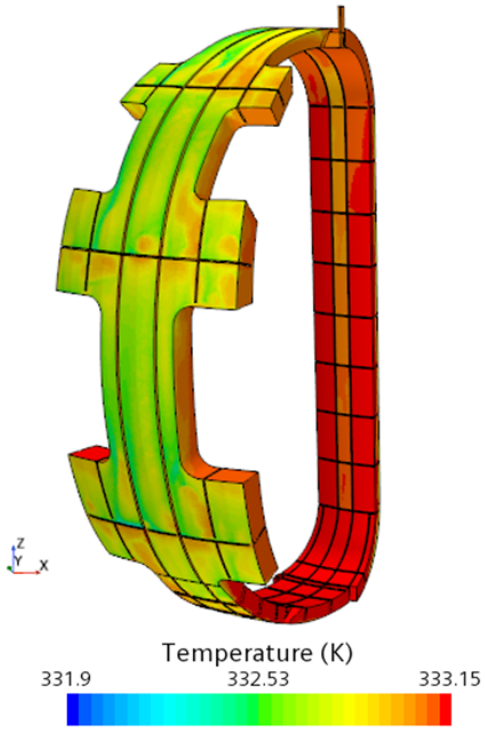

Figure B.1: CV2 Temperature Field.

	Mass Flow Rate Fraction [-]			
Channel	**Bottom**	**Equatorial**	**Up**	**Tot**
OB1	18.5%	14%	9%	54%
OB2	22.5%	22%	20%	
OB3	13%	18%	25%	
IB1	20%	20%	20%	46%
IB2	4%	4%	4%	
IB3	22%	22%	22%	
TOT	100%	100%	100%	100%

Figure B.2: CV2 mass flow rate distribution.

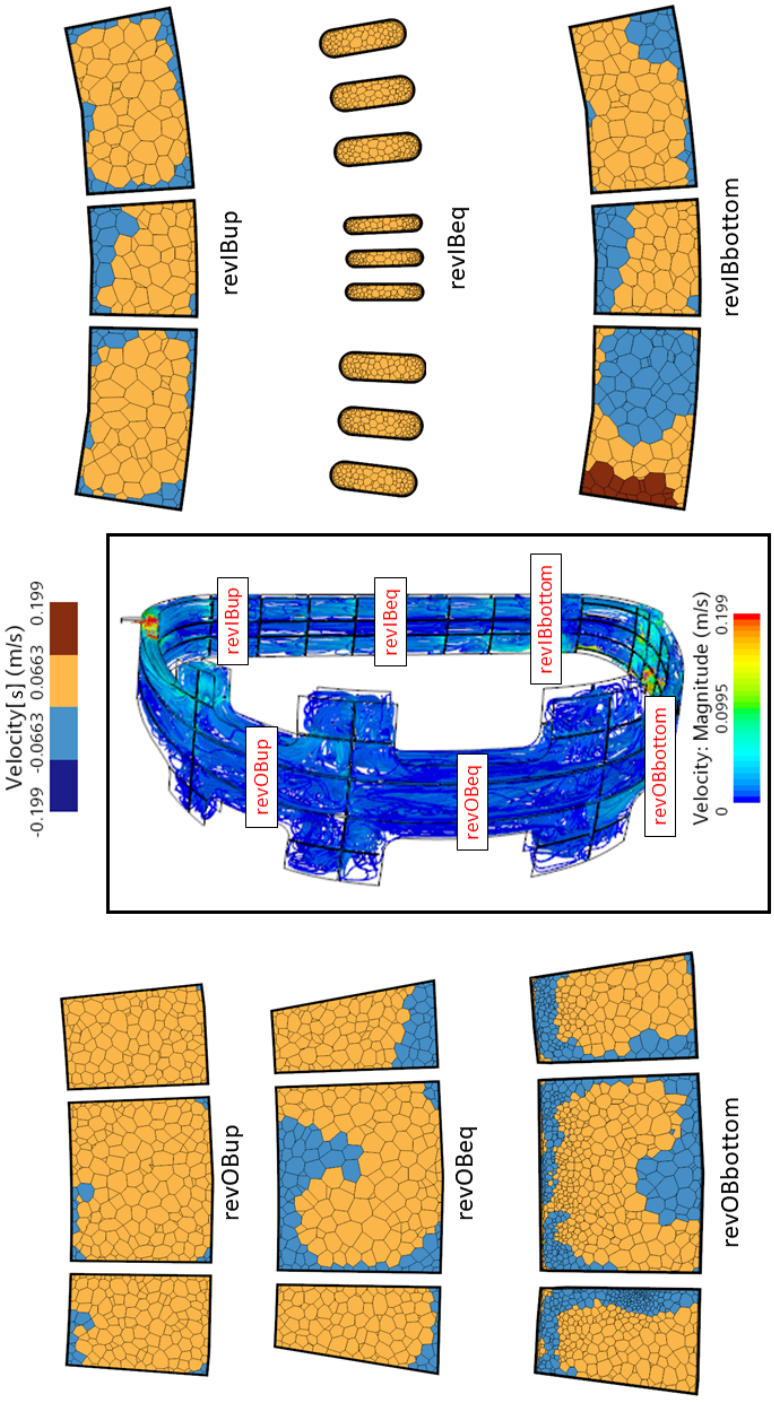

Figure B.3: CV2 V_s scalar scenes.

B.2 CV3-R

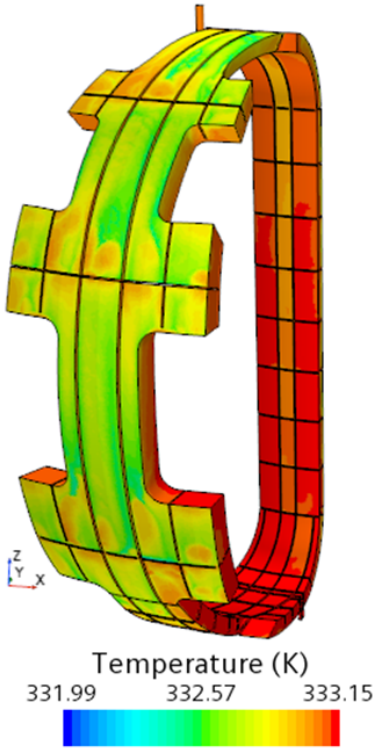

Figure B.4: CV3 Temperature Field.

	Mass Flow Rate Fraction [-]			
Channel	**Bottom**	**Equatorial**	**Up**	**Tot**
OB1	13%	20%	28%	63%
OB2	25%	26%	23%	
OB3	25%	17%	12%	
IB1	18%	18%	18%	37%
IB2	3%	3%	3%	
IB3	16%	16%	16%	
TOT	100%	100%	100%	100%

Figure B.5: CV3 mass flow rate distribution.

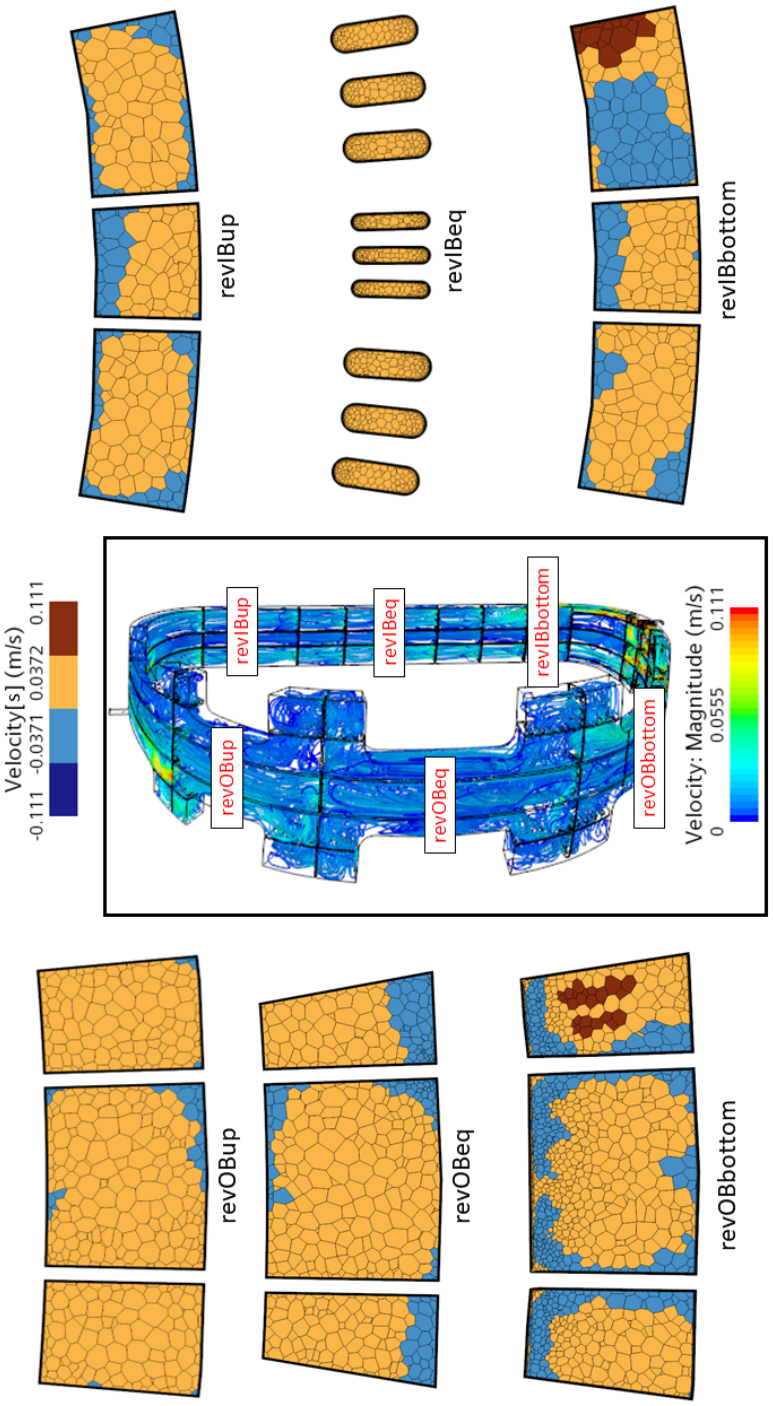

Figure B.6: CV3 V_s scalar scenes.

B.3 CV4-L

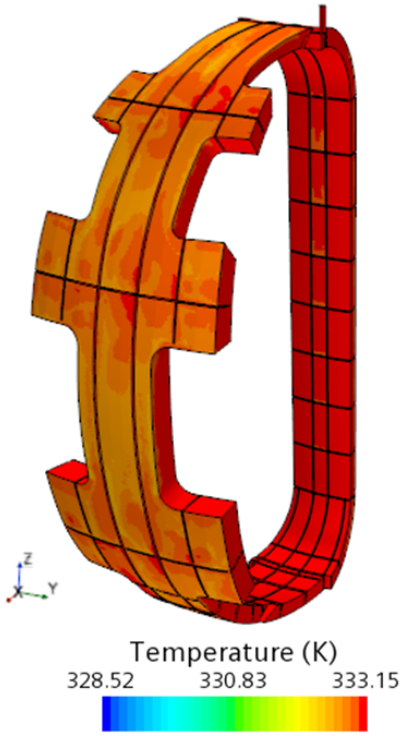

Figure B.7: CV4 Temperature Field.

	Mass Flow Rate Fraction [-]			
Channel	**Bottom**	**Equatorial**	**Up**	**Tot**
OB1	30%	23%	15%	57%
OB2	12%	11%	10%	
OB3	15%	23%	32%	
IB1	21%	21%	21%	43%
IB2	1.5%	1.5%	1.5%	
IB3	20.5%	20.5%	20.5%	
TOT	100%	100%	100%	100%

Table B.1: CV4 mass flow rate distribution.

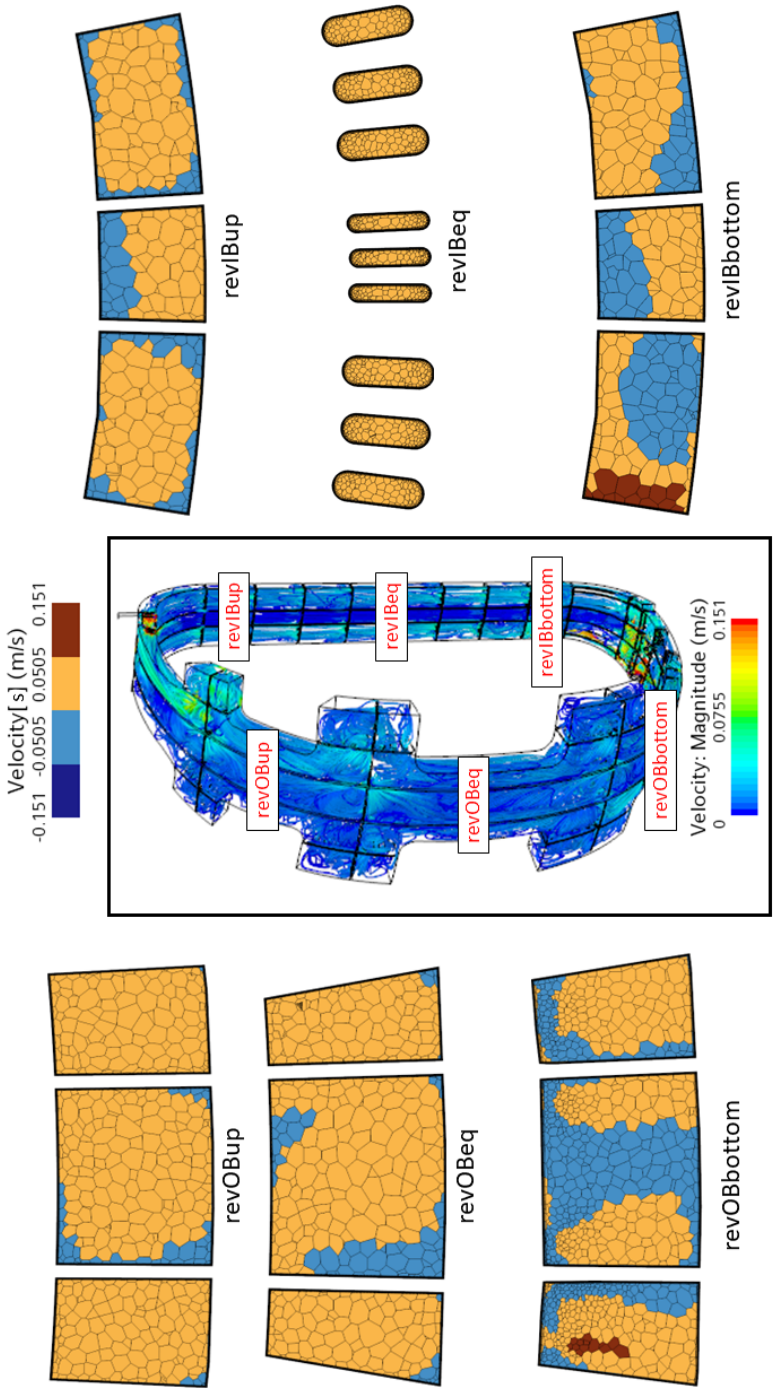

Figure B.8: CV4 V_s scalar scenes.

B.4 CV5-L

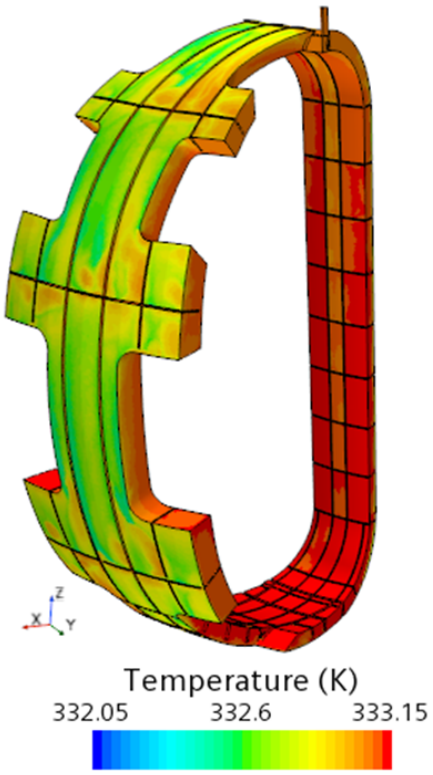

Figure B.9: CV5 Temperature Field.

	Mass Flow Rate Fraction [-]			
Channel	**Bottom**	**Equatorial**	**Up**	**Tot**
OB1	24%	18%	12%	63%
OB2	25%	25%	22%	
OB3	14%	20%	29%	
IB1	16%	16%	16%	37%
IB2	3%	3%	3%	
IB3	18%	18%	18%	
TOT	100%	100%	100%	100%

Table B.2: CV5 mass flow rate distribution.

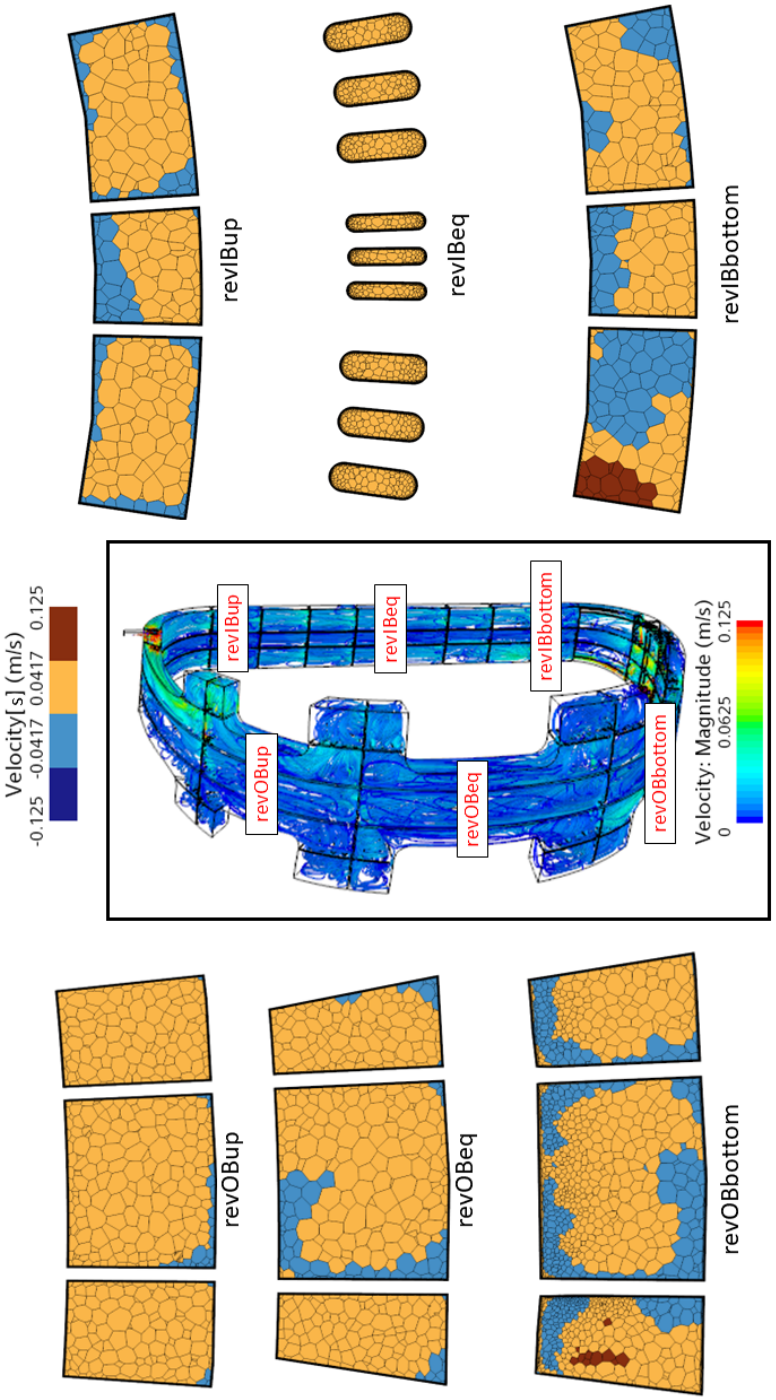

Figure B.10: CV5 V_s scalar scenes.

B.5 CV6-L

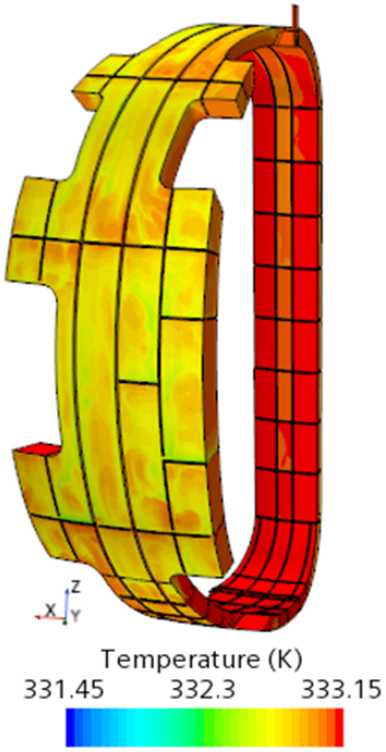

Figure B.11: CV6 Temperature Field.

	Mass Flow Rate Fraction [-]			
Channel	**Bottom**	**Equatorial**	**Up**	**Tot**
OB1	21%	15%	10%	57%
OB2	24%	24%	21%	
OB3	12%	18%	26%	
IB1	18.5%	18.5%	18.5%	43%
IB2	4.5%	4.5%	4.5%	
IB3	20%	20%	20%	
TOT	100%	100%	100%	100%

Table B.3: CV6 mass flow rate distribution.

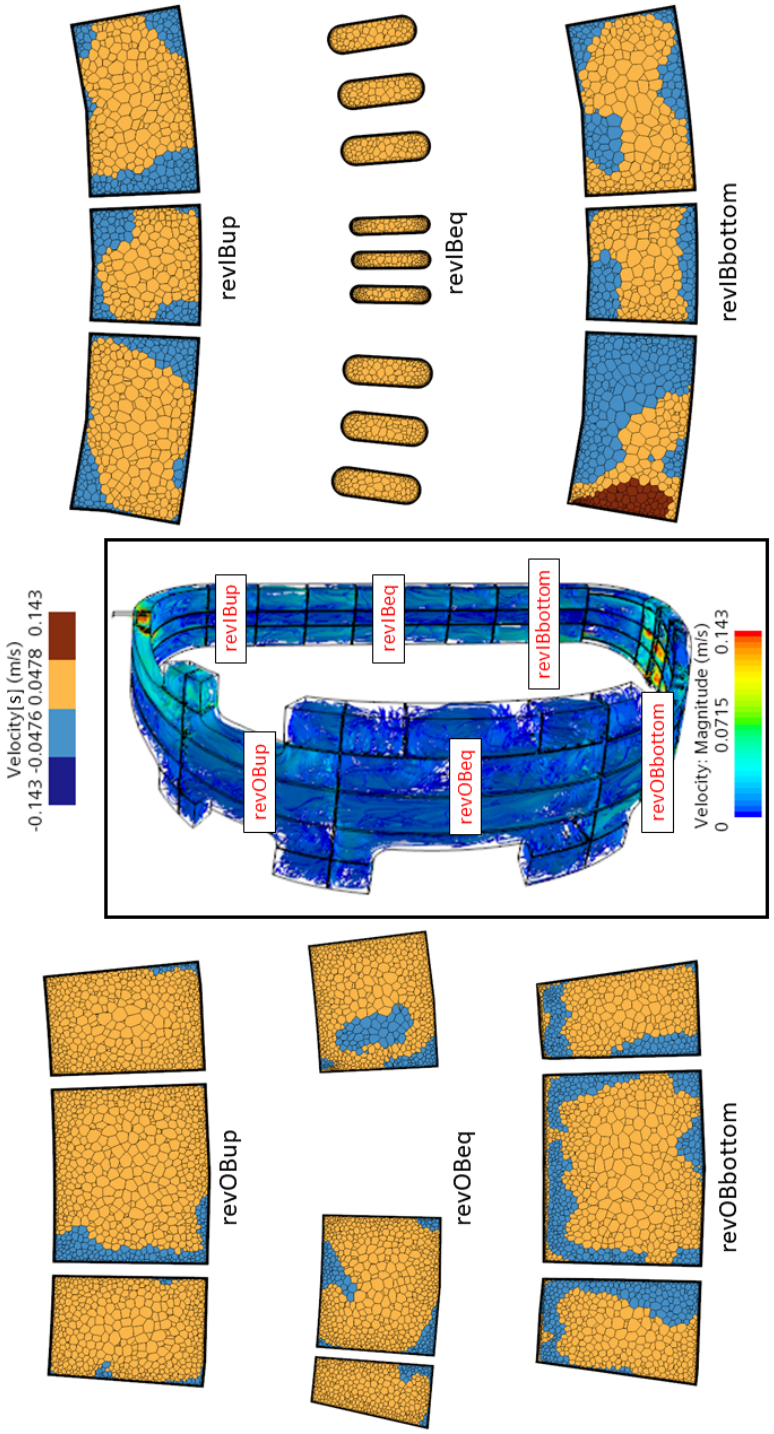

Figure B.12: CV6 V_s scalar scenes.

B.6 CV7-R

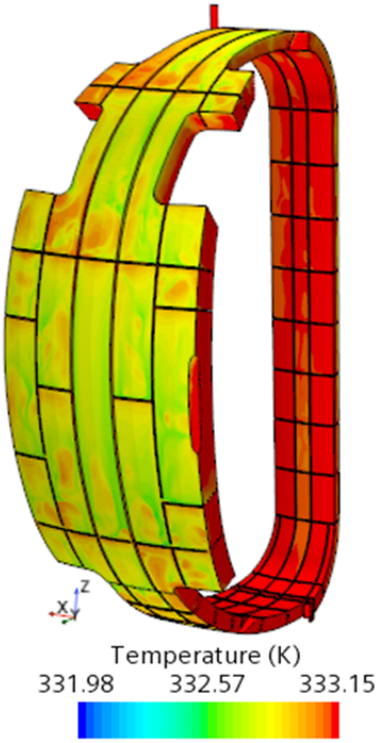

Figure B.13: CV7 Temperature Field.

	Mass Flow Rate Fraction [-]			
Channel	**Bottom**	**Equatorial**	**Up**	**Tot**
OB1	12%	18%	26%	56%
OB2	24%	23%	20%	
OB3	20%	15%	10%	
IB1	21%	21%	21%	44%
IB2	4%	4%	4%	
IB3	19%	19%	19%	
TOT	100%	100%	100%	100%

Table B.4: CV7 mass flow rate distribution.

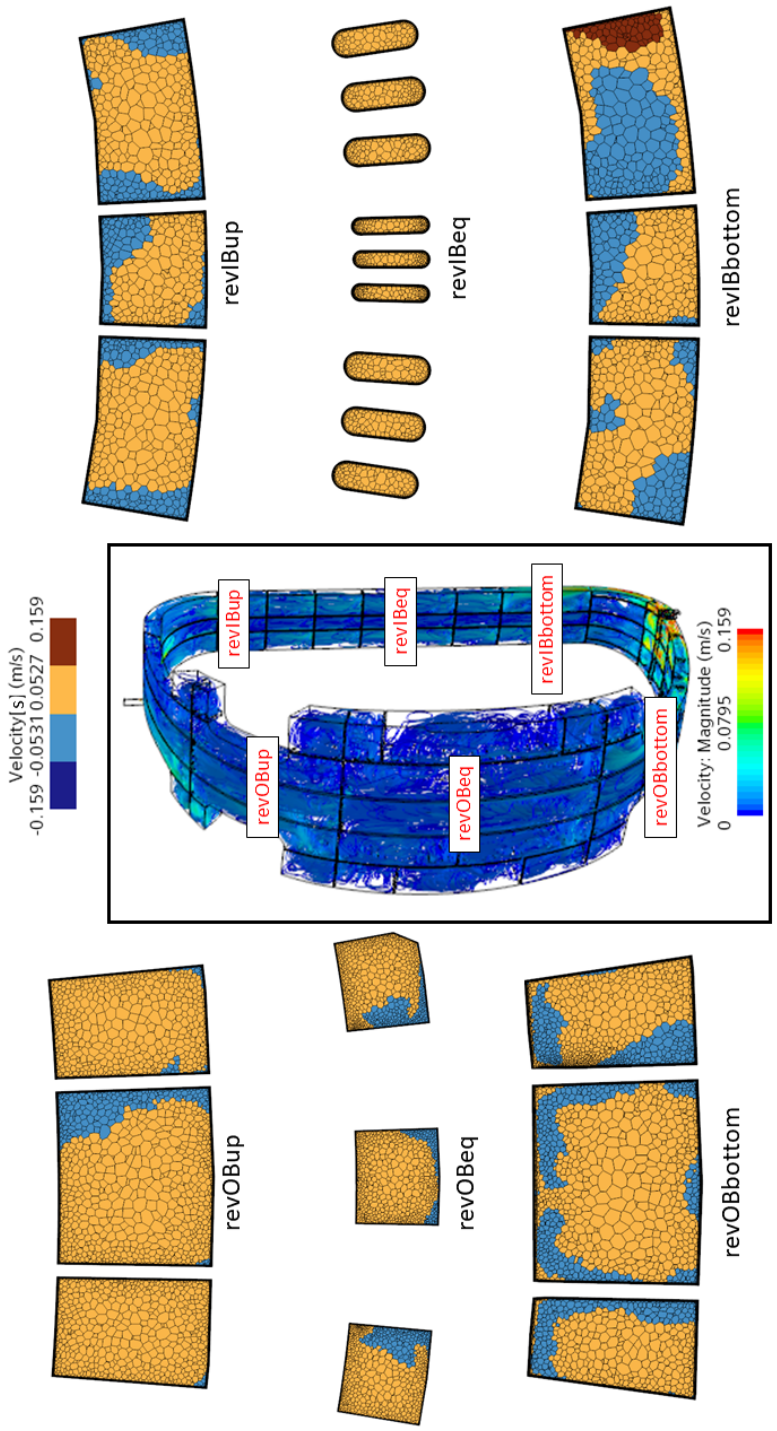

Figure B.14: CV7 V_s scalar scenes.

B.7 CV8-L

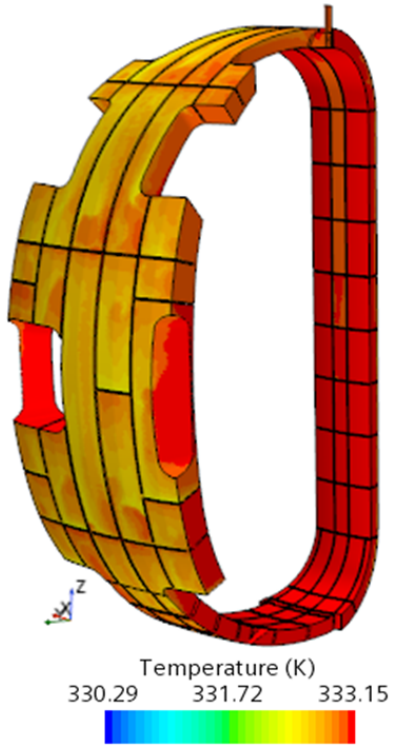

Figure B.15: CV8 Temperature Field.

	Mass Flow Rate Fraction [-]			
Channel	**Bottom**	**Equatorial**	**Up**	**Tot**
OB1	20%	13%	9%	56%
OB2	24%	25%	21%	
OB3	12%	18%	26%	
IB1	19%	19%	19%	44%
IB2	4.5%	4.5%	4.5%	
IB3	20.5%	20.5%	20.5%	
TOT	100%	100%	100%	100%

Table B.5: CV8 mass flow rate distribution.

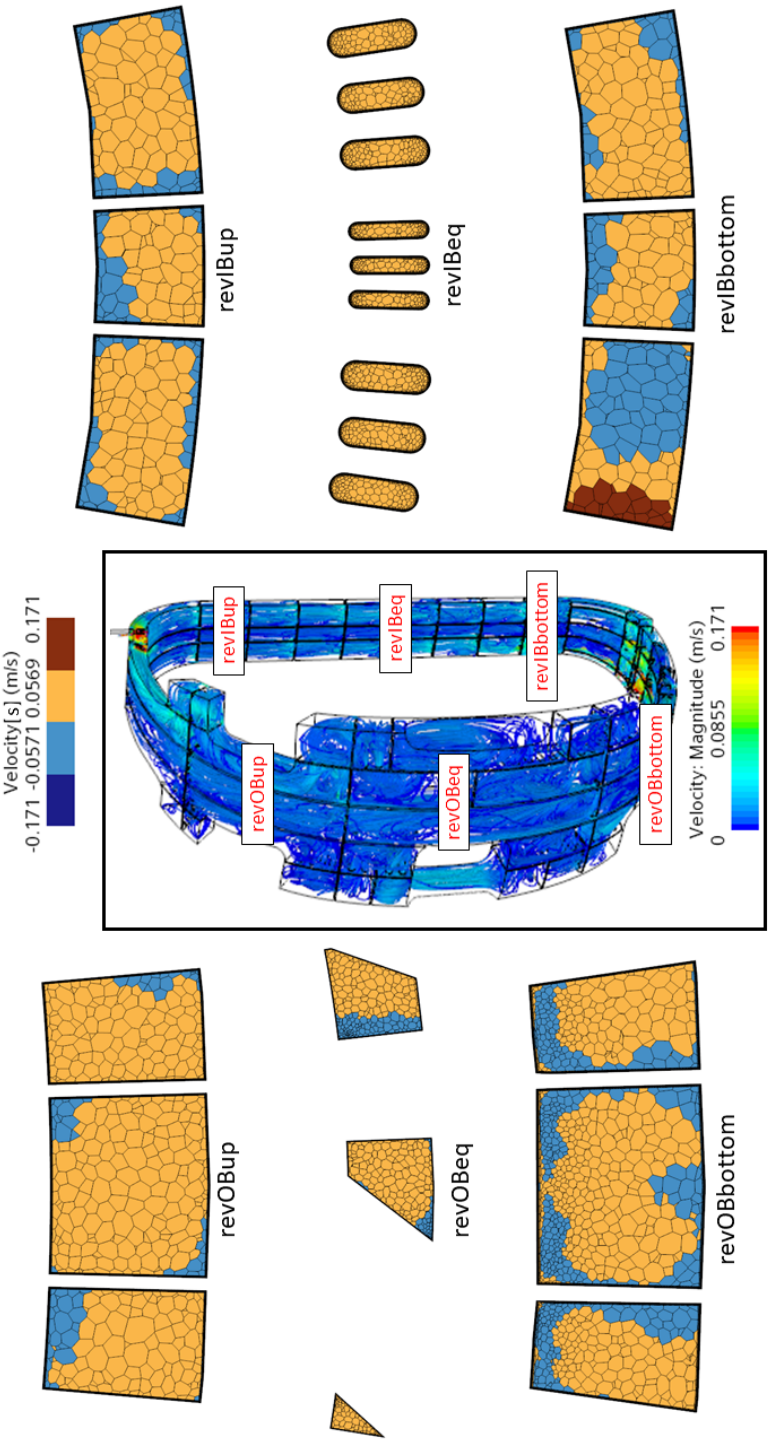

Figure B.16: CV8 V_s scalar scenes.

B.8 CV9-R

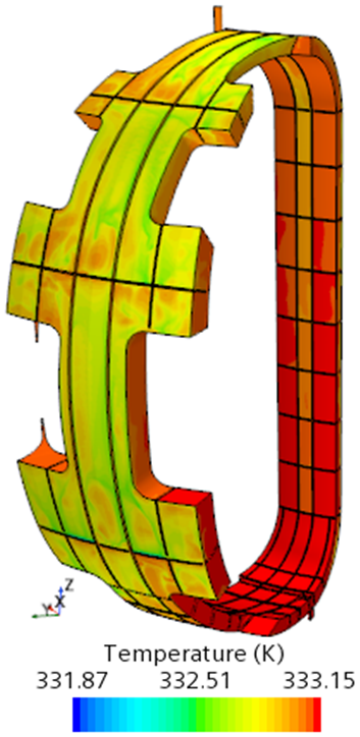

Figure B.17: CV9 Temperature Field.

	Mass Flow Rate Fraction [-]			
Channel	**Bottom**	**Equatorial**	**Up**	**Tot**
OB1	11%	12%	28%	61%
OB2	27%	32%	22%	
OB3	23%	17%	11%	
IB1	19%	19%	19%	39%
IB2	3%	3%	3%	
IB3	17%	17%	17%	
TOT	100%	100%	100%	100%

Table B.6: CV9 mass flow rate distribution.

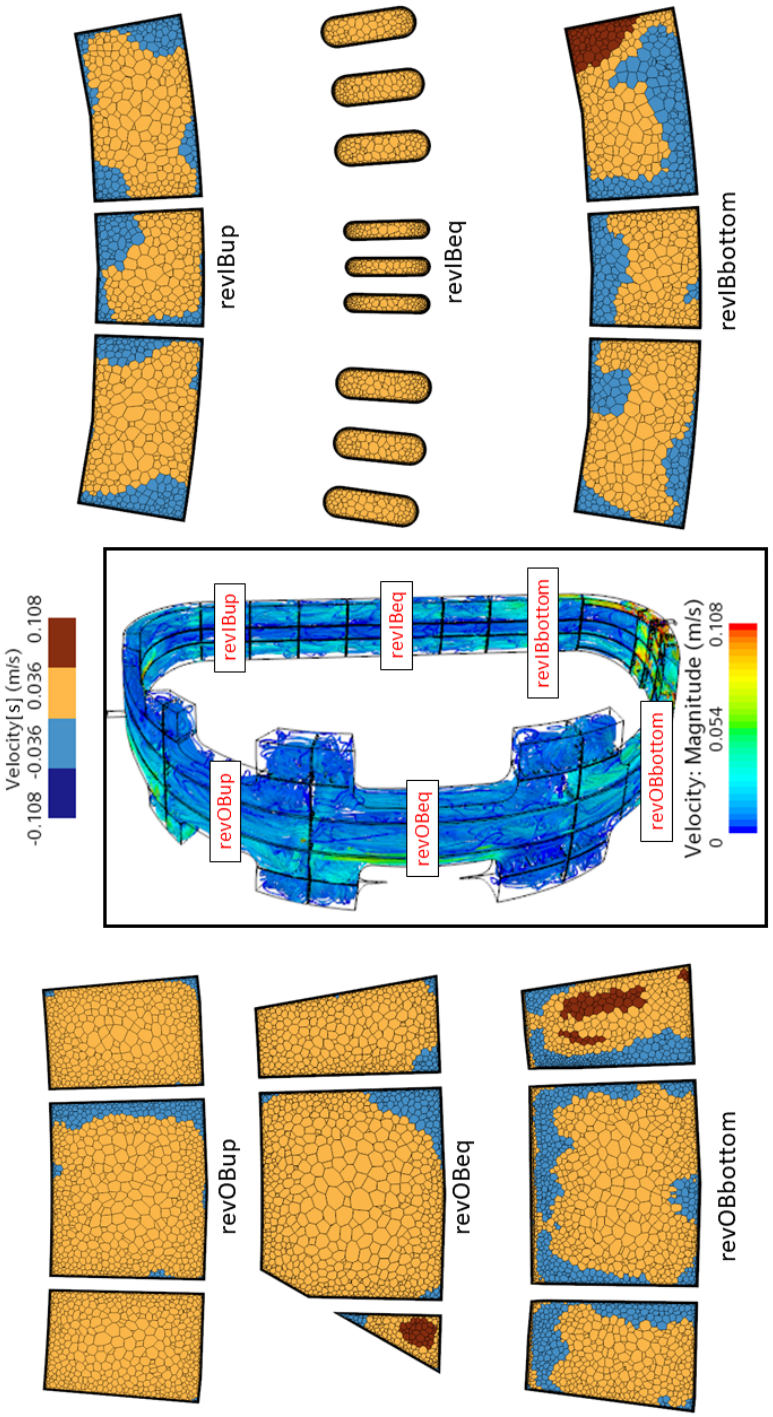

Figure B.18: CV9 V_s scalar scenes.

B.9 CV10-L

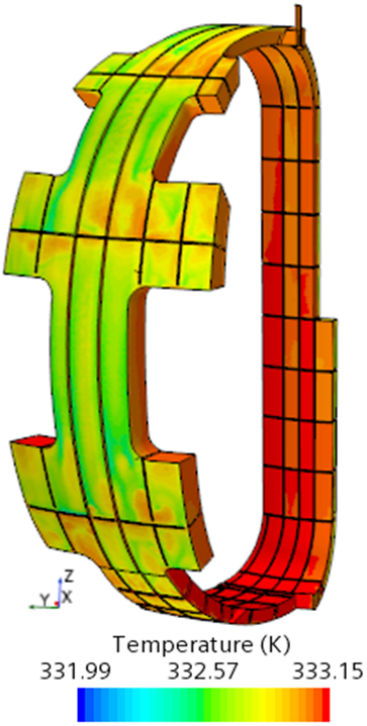

Figure B.19: CV10 Temperature Field.

	Mass Flow Rate Fraction [-]			
Channel	**Bottom**	**Equatorial**	**Up**	**Tot**
OB1	23.5%	18%	12%	63%
OB2	25.5%	26%	22%	
OB3	14%	19%	29%	
IB1	16%	16%	16%	37%
IB2	5%	5%	5%	
IB3	11.5%	16%	16%	
IB4	4.5%	-	-	
TOT	100%	100%	100%	100%

Table B.7: CV10 mass flow rate distribution.

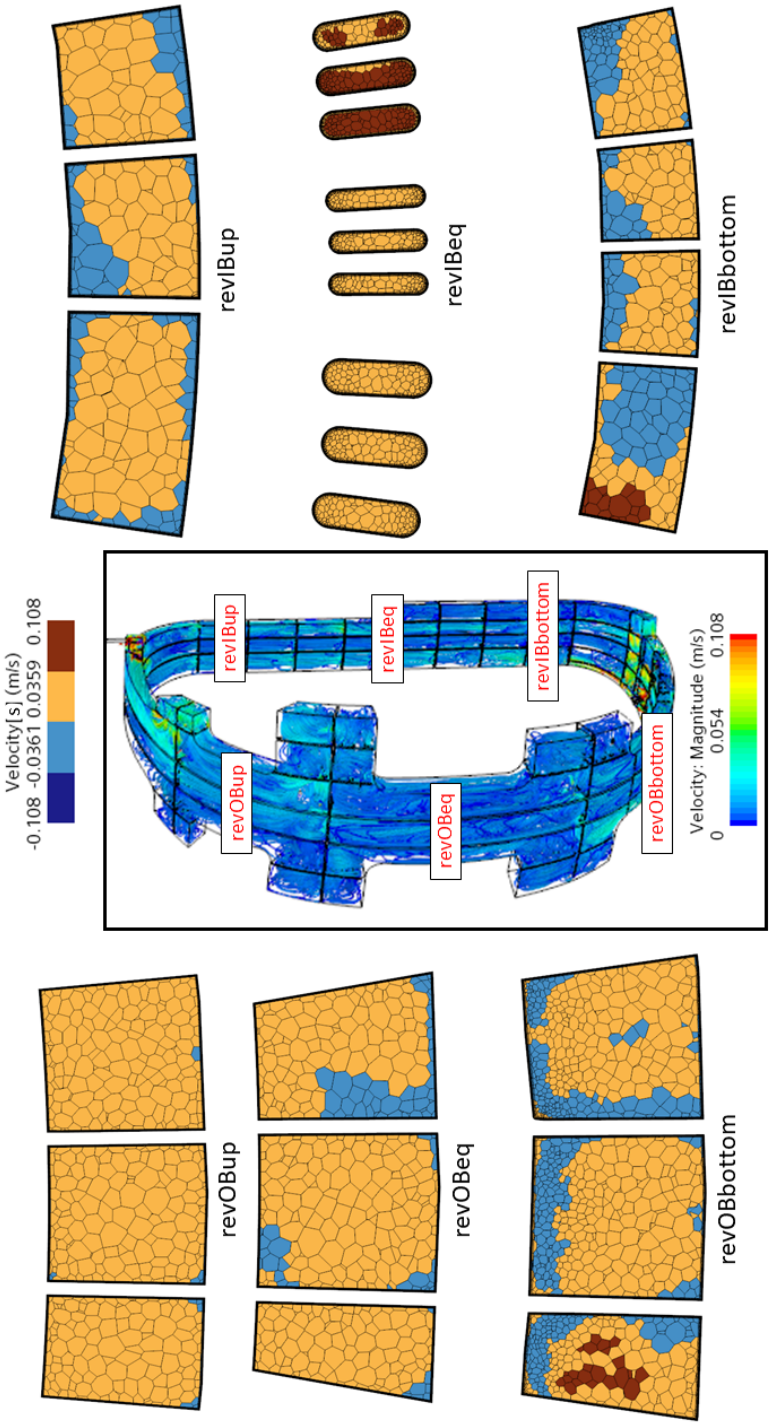

Figure B.20: CV10 V_s scalar scenes.

B.10 CV11-R

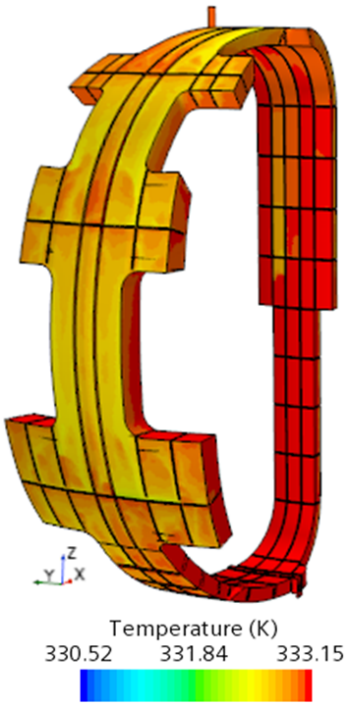

Figure B.21: CV11 Temperature Field.

	Mass Flow Rate Fraction [-]			
Channel	**Bottom**	**Equatorial**	**Up**	**Tot**
OB1	12%	16.5%	22.5%	55%
OB2	20%	22%	21%	
OB3	23%	16.5%	11.5%	
IB0	-	-	20%	45%
IB1	19.5%	19.5%	0.5% (<0)	
IB2	5.5%	5.5%	5.5%	
IB3	20%	20%	15%	
IB4	-	-	5%	
TOT	100%	100%	100%	100%

Table B.8: CV11 mass flow rate distribution.

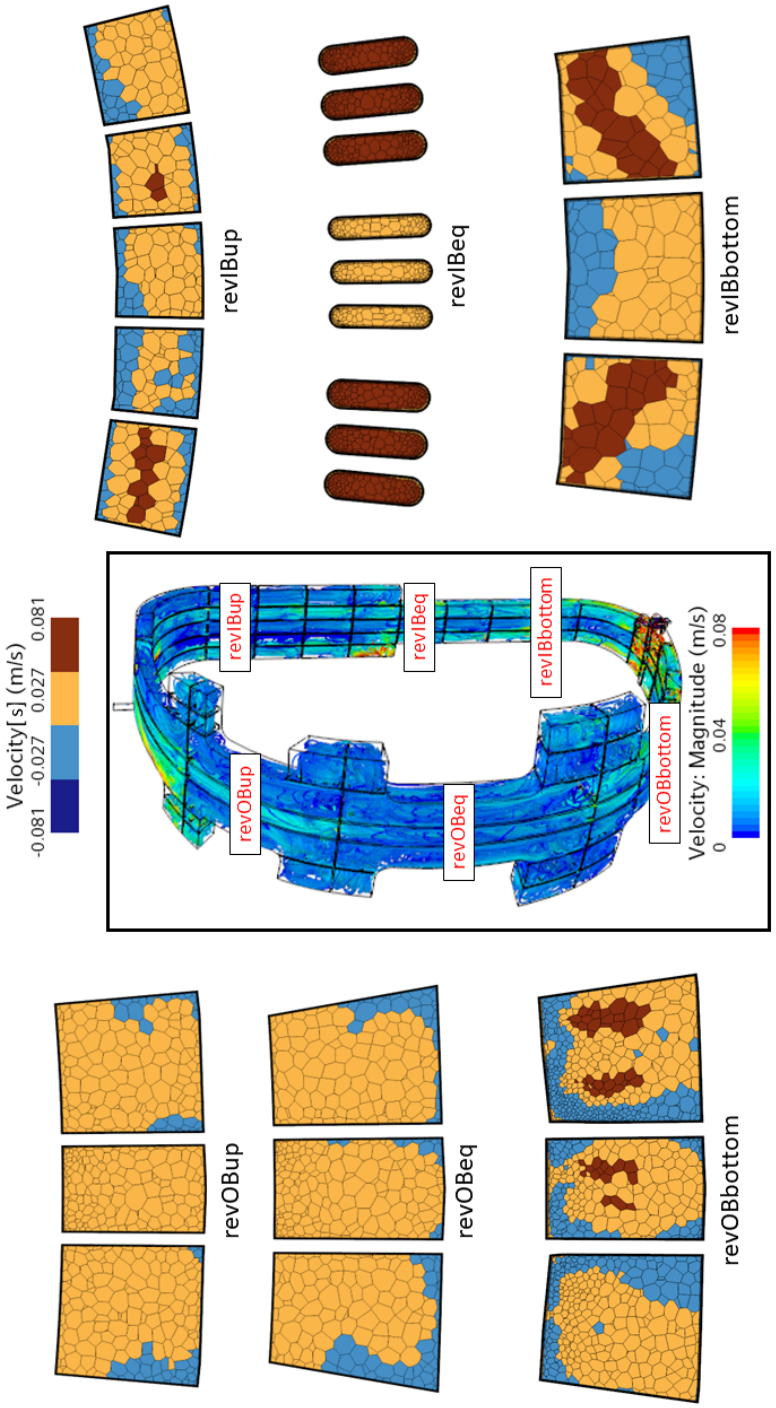

Figure B.22: CV11 V_s scalar scenes.

B.11 CV12-L

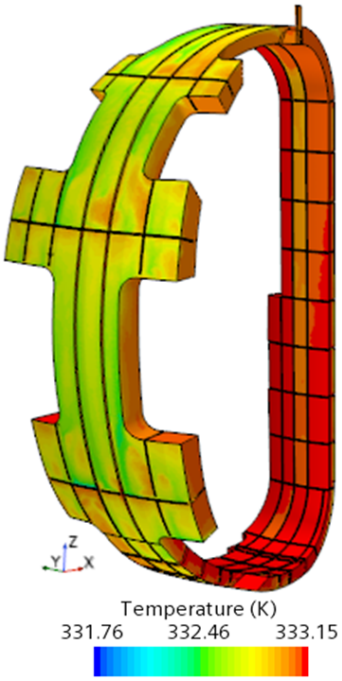

Figure B.23: CV12 Temperature Field.

	Mass Flow Rate Fraction [-]			
Channel	**Bottom**	**Equatorial**	**Up**	**Tot**
OB1	23%	16.5%	11%	50.5%
OB2	17%	18%	16%	
OB3	10.5%	16%	23.5%	
IB0	31%	-	-	49.5%
IB1	9% (<0)	22%	22%	
IB2	3.5%	3.5%	3.5%	
IB3	24%	24%	24%	
TOT	100%	100%	100%	100%

Table B.9: CV12 mass flow rate distribution.

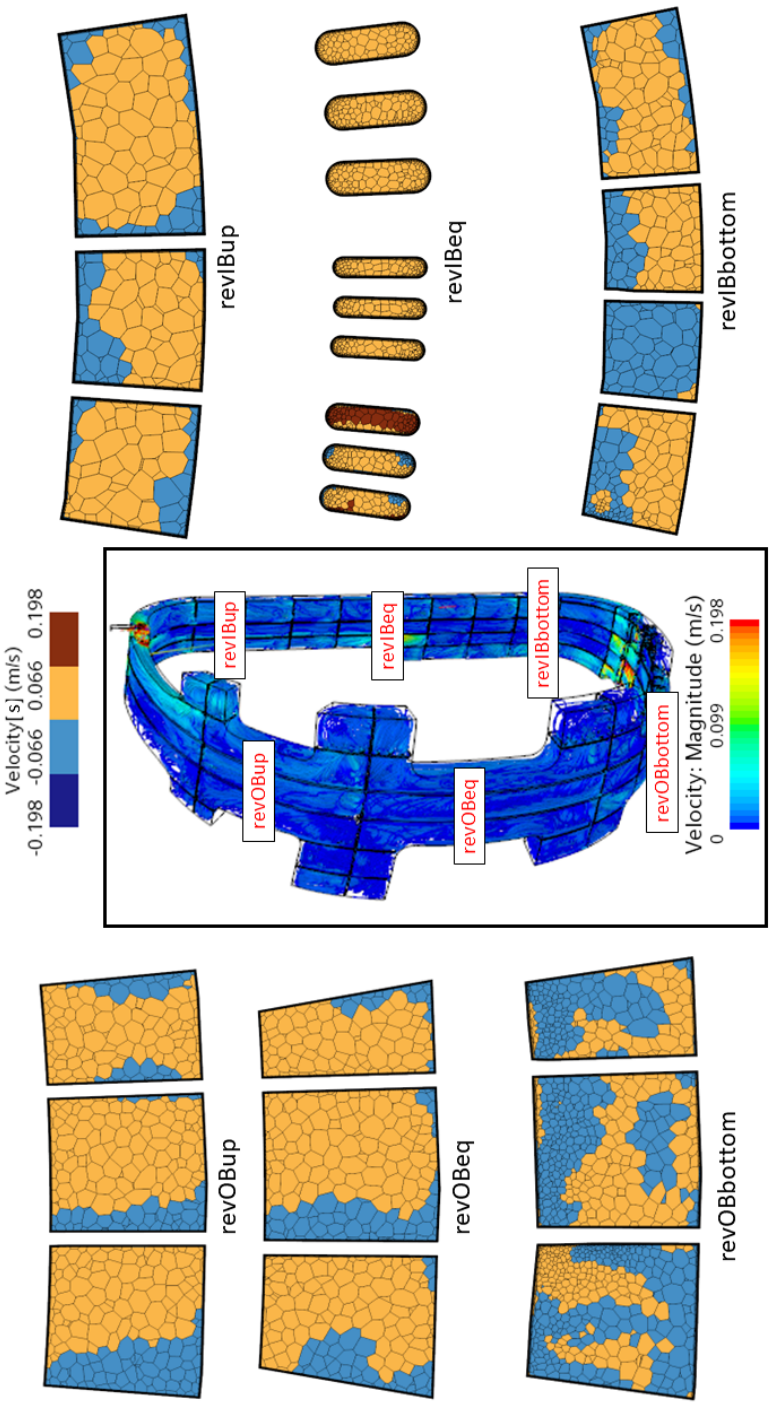

Figure B.24: CV12 V_s scalar scenes.

Bibliography

[1] EUROfusion. *The road to fusion energy*. 2018. URL: https://euro-fusion.org/eurofusion/roadmap/ (visited on 03/06/2023) (cit. on p. 6).

[2] ENEA. *Divertor Tokamak Test Facility Project Proposal*. 2015. URL: https://www.dtt-project.it/index.php/about/who.html?highlight=WyJibHVlIiwiYm9vayIsImJsdWUgYm9vayJd (visited on 03/06/2023) (cit. on p. 7).

[3] ENEA. *DTT, who?* 2022. URL: https://www.dtt-project.it/index.php/about/who.html?highlight=WyJibHVlIiwiYm9vayIsImJsdWUgYm9vayJd (visited on 03/06/2023) (cit. on p. 7).

[4] ENEA. *Divertor Tokamak Test Facility Interim Design Report – A milestone along the roadmap to the realisation of fusion energy*. 2019. URL: https://www.dtt-project.it/index.php/dtt-green-book.html (visited on 02/01/2023) (cit. on pp. 12, 24, 52, 69).

[5] Bonifetto Roberto. *Thermal-hydraulic analysis of the Vacuum Vessel of the Divertor Tokamak Test Facility*. Tech. rep. DTT Project, 2021 (cit. on pp. 13, 33, 42, 52, 72).

[6] P Agostinetti et al. «Improved Conceptual Design of the Beamline for the DTT Neutral Beam Injector». In: *IEEE Transactions on Plasma Science* 50.11 (2022), pp. 4027–4032 (cit. on pp. 20, 24).

[7] ITER Organization. *BAKING IT HOT*. 2010. URL: https://www.iter.org/newsline/130/172 (cit. on p. 26).

[8] Philip M Gerhart, Andrew L Gerhart, and John I Hochstein. *Munson, Young and Okiishi's Fundamentals of Fluid Mechanics*. John Wiley & Sons, 2016 (cit. on pp. 28, 57).

[9] David C Wilcox et al. *Turbulence modeling for CFD*. Vol. 2. DCW industries La Canada, CA, 1998 (cit. on pp. 29, 34).

[10] AN Kolmogorov. «Equations of turbulent motion of an incompressible fluid, Izv. Acad. Sci., USSR». In: *Physics* 6.1 (1942), p. 2 (cit. on p. 34).

[11] Philippe R Spalart and Christopher L Rumsey. «Effective inflow conditions for turbulence models in aerodynamic calculations». In: *AIAA journal* 45.10 (2007), pp. 2544–2553 (cit. on p. 34).

[12] David C Wilcox. «Formulation of the kw turbulence model revisited». In: *AIAA journal* 46.11 (2008), pp. 2823–2838 (cit. on pp. 35, 37).

[13] Langley Research Center. *Turbulence Modeling Resource*. 2022. URL: `https://turbmodels.larc.nasa.gov/` (visited on 12/13/2022) (cit. on p. 36).

[14] PG Huang. «Physics and computations of flows with adverse pressure gradients». In: *Modeling Complex Turbulent Flows*. Springer, 1999, pp. 245–258 (cit. on p. 36).

[15] Florian R Menter. «Two-equation eddy-viscosity turbulence models for engineering applications». In: *AIAA journal* 32.8 (1994), pp. 1598–1605 (cit. on p. 37).

[16] Paul A Durbin. «On the k-ε stagnation point anomaly». In: *Int. J. Heat and Fluid Flow* 17 (1996), pp. 9–90 (cit. on p. 39).

[17] Chang Hwan Park and Seung O Park. «On the limiters of two-equation turbulence models». In: *International Journal of Computational Fluid Dynamics* 19.1 (2005), pp. 79–86 (cit. on p. 39).

[18] The Engineering ToolBox. *Water – Speed of Sound vs. Temperature*. 2022. URL: `https://www.engineeringtoolbox.com/sound-speed-water-d_598.html` (visited on 02/01/2023) (cit. on p. 54).

[19] Hans Reichardt. «Vollständige Darstellung der turbulenten Geschwindigkeitsverteilung in glatten Leitungen-Complete representation of the turbulent velocity distribution in smooth pipes». In: *ZAMM-Journal of Applied Mathematics and Mechanics/Zeitschrift für Angewandte Mathematik und Mechanik* 31.7 (1951), pp. 208–219 (cit. on p. 61).

[20] Johann Nikuradse et al. «Laws of flow in rough pipes». In: (1950) (cit. on p. 66).

[21] Lewis F Moody. «Friction factors for pipe flow». In: *Trans. Asme* 66 (1944), pp. 671–684 (cit. on p. 67).

[22] Cyril Frank Colebrook, T Blench, H Chatley, EH Essex, JR Finniecome, G Lacey, J Williamson, and GG Macdonald. «Turbulent flow in pipes, with particular reference to the transition region between the smooth and rough pipe laws.» In: *Journal of the Institution of Civil engineers* 12.8 (1939), pp. 393–422 (cit. on p. 67).

[23] Rosaria Villari et al. «Nuclear design of divertor tokamak test (DTT) facility». In: *Fusion Engineering and Design* 155 (2020), p. 111551 (cit. on p. 69).

[24] C Gasparrini et al. «Water Chemistry in Fusion Cooling Systems: Borated Water for DTT Vacuum Vessel». In: *IEEE Transactions on Plasma Science* (2022) (cit. on pp. 70, 72).

[25] K Crapse and E Kyser. «Literature review of boric acid solubility data». In: (2011) (cit. on pp. 71, 72).

[26] ND Azizov and TS Akhundov. «Thermal properties of the aqueous solutions of boric acid at 298-573 K». In: *Teplofizika vysokikh temperatur* 34.5 (1996), pp. 798–802 (cit. on p. 72).

[27] WA Byers, WL Brown, BE Kellerman, KS Shearer, and DJ Fink. «Summary of tests to determine the physical properties of buffered and un-buffered boric acid solutions». In: *Westinghouse Non-Proprietary Class* 3 (2010) (cit. on p. 72).

[28] AS Avanesyan and TS Akhundov. «Experimental Study of the Coefficient of Dynamic Viscosity of Aqueous Solutions of Boric Acid». In: *Preprint AN ArmSSR* (1980) (cit. on p. 72).

[29] AV Morozov, AV Pityk, AR Sahipgareev, and AS Shlepkin. «Experimental study of the thermophysical properties of boric acid solutions at the parameters typical of the WWER emergency mode». In: *Journal of Physics: Conference Series*. Vol. 1128. 1. IOP Publishing. 2018, p. 012103 (cit. on p. 72).

[30] Maogang He, Chao Su, Xiangyang Liu, and Xuetao Qi. «Isobaric heat capacity of boric acid solution». In: *Journal of Chemical & Engineering Data* 59.12 (2014), pp. 4200–4204 (cit. on p. 74).

[31] Nese Keklikcioğlu Çakmak. «EXPERIMENTAL STUDY OF THERMAL CONDUCTIVITY OF BORIC ACID- WATER SOLUTIONS». In: *Heat Transfer Research* 50.17 (2019) (cit. on pp. 75, 77).

[32] Hermann Schlichting and Joseph Kestin. *Boundary layer theory*. Vol. 121. Springer, 1961 (cit. on p. 132).

[33] Sasa Kenjereš, SB Gunarjo, and K Hanjalić. «Contribution to elliptic relaxation modelling of turbulent natural and mixed convection». In: *International Journal of Heat and Fluid Flow* 26.4 (2005), pp. 569–586 (cit. on p. 134).

[34] Manfred Wier and L Römer. «Experimentelle Untersuchung von stabil und instabil geschichteten turbulenten Plattengrenzschichten mit Bodenrauhigkeit». In: *Zeitschrift für Flugwissenschaften und Weltraumforschung* 11.2 (1987), pp. 78–86 (cit. on p. 135).

[35] Martin Oberlack. «A unified approach for symmetries in plane parallel turbulent shear flows». In: *Journal of Fluid Mechanics* 427 (2001), pp. 299–328 (cit. on p. 135).

[36] Chandra Laksham Vaidyaratna Jayatilleke. «The influence of Prandtl number and surface roughness on the resistance of the laminar sub-layer to momentum and heat transfer». In: (1966) (cit. on p. 136).

[37] BA Kader. «Temperature and concentration profiles in fully turbulent boundary layers». In: *International journal of heat and mass transfer* 24.9 (1981), pp. 1541–1544 (cit. on p. 136).